# NiAl AND STEEL AS MATRICES AND TiC AND OXYNITRIDES AS REINFORCEMENTS IN METAL-MATRIX COMPOSITE FABRICATION

**SIGQIBO TEMPLETON CAMAGU**

**A thesis submitted in fulfilment of the requirement for the degree of Doctor Philosophiae in the Department of Physics and Astronomy, University of the Western Cape.**

UNIVERSITY of the
WESTERN CAPE

**Supervisor: Dr A. S. Bolokang, Council for Scientific and Industrial Research (Advanced Materials Engineering); University of the Western Cape**

**Co-Supervisor: Prof. C. J. Arendse, University of the Western Cape**

**27 OCTOBER 2021**

http://etd.uwc.ac.za/

## ACKNOWLEDGEMENTS

I would like to acknowledge the following people for the role they played during this research

- My supervisors, Dr Sylvester A. Bolokang and Prof. Christopher J. Arendse who relentlessly offered encouragement, support and constant availability throughout.
- CSIR AME staff, Dr Robert T Tshikhudo who encouraged me to pursue the PhD study and supported my application to the CSIR for funding of this study. Dr Sagren Govender, Dr Maria N. Mathabathe, Mr Ndumiso Mnguni, Mrs Zizo Gxowa-Penxa, Ms Pfarelo Daswa, Ms Mary Mojalefa and many more AME staffers offered a lot of support.
- Dr Sagren Govender, thank you for your open-door policy – always available for a chat and support.
- Ms Mary Mojalefa, thank you for conferring the "PhD" upon me before a university could.
- Mrs Christa Marais, Information Scientist at CSIR BEI, thank you for ensuring that I have uninterrupted access to scientific literature search engines during the lockdown period and your alerts that are always on point.
- UWC Physics Department staff, Dr Franscious R. Cummings, Dr Theophillus F.G. Muller, Mrs Angela Adams, and Natasha Peterson thank you for your assistance and hospitality.
- To my family, Nomonde Camagu (my wife), Onesimo Matshini (my daughter), Bonani Camagu and Lakhiwe Camagu (my sons) as well as my mother, Nothemba Camagu, thank you for being my inspiration.
- Finally, I would like to thank the Department of Science and Innovation – CSIR Titanium Centre of Competence (TiCoC) for their financial support.

UNIVERSITY of the WESTERN CAPE

## DECLARATION

I declare that

# "NiAl AND STEEL AS MATRICES AND TiC AND OXYNITRIDES AS REINFORCEMENTS IN METAL-MATRIX COMPOSITE FABRICATION"

is my own work except where otherwise stated and acknowledged by means of complete references. I state that this work has not been previously accepted in substance for any degree and is not being submitted in candidature for any degree.

Sigqibo Templeton Camagu

UNIVERSITY of the
WESTERN CAPE

Signature: _____ 27 OCTOBER 2021

## KEYWORDS

# NiAl AND STEEL AS MATRICES AND TiC AND OXYNITRIDES AS REINFORCEMENTS IN METAL-MATRIX COMPOSITE FABRICATION

**SIGQIBO TEMPLETON CAMAGU**

Nickel Aluminium

Titanium Carbide

Steel Alloy

Oxynitrides

Metal Matrix Composites

Metal Powder Compaction

Sintering

Oxidation

Thermal Behaviour

Electron Back Scatter Diffraction

High Resolution Scanning Electron Microscopy

Deferential Scanning Calorimetry

Lattice Parameter

X ray Diffraction

Microhardness

UNIVERSITY of the
WESTERN CAPE

## LIST OF ARTICLES INCLUDED IN THIS DISSERTATION

1. S.T. Camagu, N.M. Mathabathe, D.E. Motaung, T.F.G. Muller, C.J. Arendse, A.S. Bolokang, “Investigation into the thermal behaviour of the B2–NiAl intermetallic alloy produced by compaction and sintering of the elemental Ni and Al powders”, Vacuum 169 (2019) 108919.
2. S. T. Camagu, D. E. Motaung, A. S. Bolokang, C. J. Arendse, “Microstructure and hardness of Steel/Ni–TiC composite produced by compaction and sintering”, Materials Today: Proceedings 38 (2021) 553–557.
3. S.T. Camagu, A.S. Bolokang, T.F.G. Muller, D.E. Motaung, C.J. Arendse, “Surface characterization and formation mechanism of the ceramic $TiO_{2-x}N_x$ spherical powder induced by annealing in air”, Powder Technology 351 (2019) 229–237.

## OTHER RESEARCH AND DEVELOPMENT OUTPUTS

### Journal Publications

UNIVERSITY of the
WESTERN CAPE

4. A.S. Bolokang, D.E. Motaung, C.J. Arendse, S.T. Camagu, T.F.G. Muller, “Structure–property analysis of the Mg–$TiO_2$ and Mg–Sn–$TiO_2$ composites intended for biomedical application”, Materials Letters 161 (2015) 328–331.
5. S. L. Pityana, S. T. Camagu, J. Dutta Majumdar, “Laser surface alloying of Al with Cu and Mo powders”, The Journal of The Southern African Institute of Mining and Metallurgy, 115 (2015) 193-198.
6. C. J. Oliphant, C. J. Arendse, S. T. Camagu, H. Swart, “EBSD analysis of tungsten-filament carburization during the hot-wire CVD of multi-walled carbon nanotubes” Microscopy and Microanalysis, Microscopy Society of America 2013, 1-10.

http://etd.uwc.ac.za/

7. A.S. Bolokang, M.J. Phasha, S.T. Camagu, D.E. Motaung and S. Bhero, “Effect of thermal treatment on mechanically deformed cobalt powder” Int. Journal of Refractory Metals and Hard Materials 31 (2012) 258–262.

## Conference Publications

8. S.T. Camagu, G. Govender, H. Moller, “Wear behaviour of A356 aluminium alloy reinforced with micron and nano size SiC particles”, Materials Science Forum, Trans Tech Publication, 765 (2013), 554-557
9. L. Ivanchev, S.T. Camagu, and G. Govender, “Semi-solid high pressure die casting of metal matrix composites produced by liquid state processing” Semi State Phenomena, Trans Tech Publication, 192-193(2012), 61-65

UNIVERSITY of the
WESTERN CAPE

# GRAPHICAL ABSTRACT

## NiAl AND STEEL AS MATRICES AND TiC AND OXYNITRIDES AS REINFORCEMENTS IN MMC FABRICATION

### Fabrication of B2-NiAl

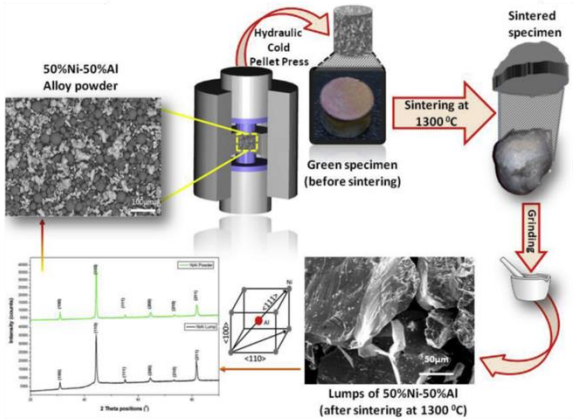


A cubic B2–NiAl alloy was synthesized by mixing of elemental Ni and Al powders followed by cold compacting and sintering of some samples at 750 °C and other samples at 1300 °C.

### Fabrication of Ni62.5Al37.5TiC1.28 composite

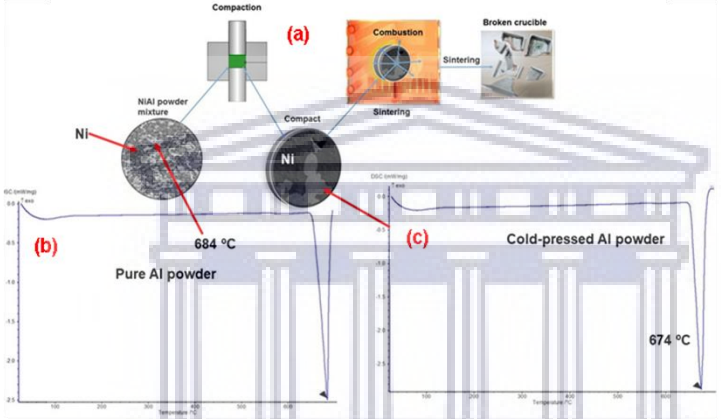


Ni62.5Al37.5TiC1.28 composite was developed by powder mixing, compaction and sintering at 650 °C.

### Fabrication of Steel/Ni–TiC composite

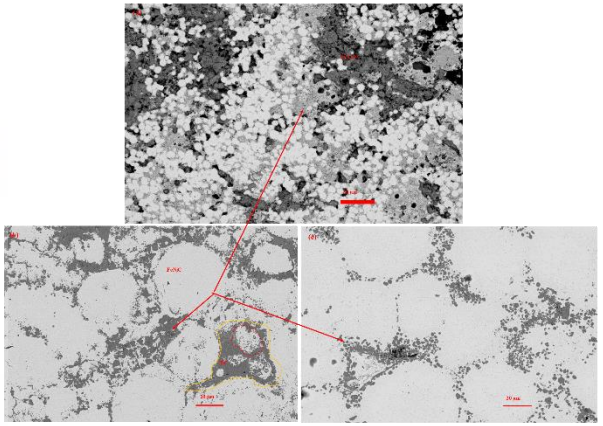

A Steel/Ni reinforced with 1.0–1.5 wt% TiC composite material was developed by compaction and sintering processes.

UNIVERSITY of the
WESTERN

### Fabrication of titanium oxynitride (TiO2-xNx)

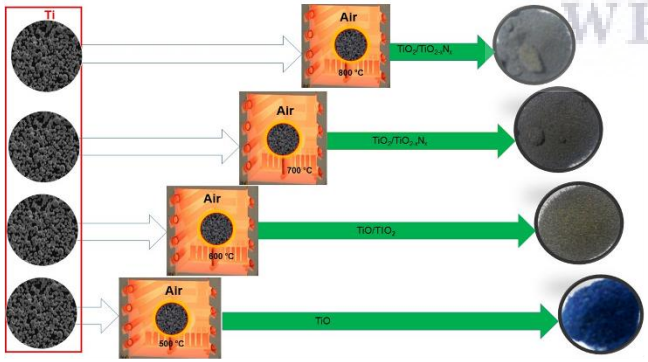


Titanium oxynitride (TiO2-xNx) was formed on the surfaces of spherical Ti powder particles upon heat treatment in air at 500, 600, 700 and 800 °C.

### Fabrication of A356-1Sn-5Ni-(TiO2-x-Nx) Composite

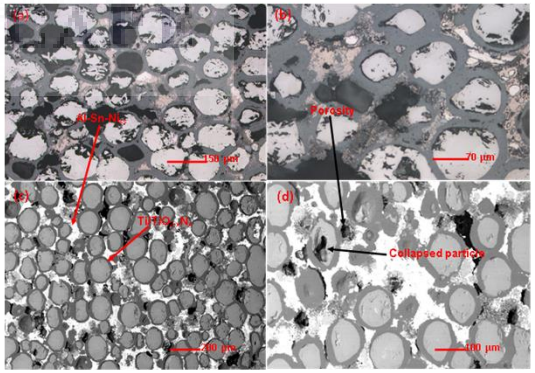


A ceramic composite material of A356-1Sn-5Ni-(TiO2-x-Nx) composition was developed with TiO2-x-Nx ceramic particles bonded without forming any intermetallic particles such as Al3Ti with Ti.

http://etd.uwc.ac.za/

# ABSTRACT

Metal matrix composites harness the superior attributes of their individual constituents to form high performance materials that would rather be impossible from monolithic substances. Owing to many possible combinations, a myriad of metal matrix composite systems can be fabricated with a metal (or a metal alloy) as a matrix (continuous) phase and a ceramic as a reinforcement (discontinuous) phase. The current study focuses on two matrices, namely Nickel Aluminide and Austenitic Steel as well as two reinforcements namely, Titanium Carbide and Oxynitrides. NiAl alloys are candidates for high temperature structural materials due to their high melting temperature, low density, good thermal conductivity, and excellent oxidation resistance. This class of materials has however found limited applications due to low room temperature ductility and poor machinability. Stainless steel is still the lifeblood for several industrial applications due to their multipurpose attributes, long life cycle and recyclability. TiC is the third most used reinforcement behind SiC and $Al_2O_3$. Metal oxynitrides have been developed as materials for photocatalytic, gas sensing and various other applications. For the current study, of the eight aspects (two matrices, two reinforcements and four composite systems) are studied and some are captured by means of peer reviewed publications in scientific journals. The article-based research study covered the following:

A B2–NiAl intermetallic synthesized by mixing of elemental Ni and Al powders followed by cold compacting and sintering exhibited excessive brittle behaviour for samples sintered at higher (1300 °C) than those sintered at lower (750 °C) temperatures. The B2–NiAl intermetallic developed a thin scale of stable $Al_2O_3$ alloy upon oxidation in air at 750 °C for 120 h. The B2–NiAl intermetallic developed a thin scale of stable $Al_2O_3$ upon oxidation in air at 750 °C for 120 h. The $Al_2O_3$ formed a barrier on the sample's surface which prevented further oxidation except for traces of $Al_2O_3$ formed via intergranular

UNIVERSITY of the
WESTERN CAPE

http://etd.uwc.ac.za/

oxidation which transformed into a metastable monoclinic oxynitride phase due to nitrogen (N) contamination.

A $Ni_{62.5}Al_{37.5}TiC_{1.28}$ composite was developed via elemental powder mixing (of Ni, Ai, and TiC), compaction and sintering at 650 ºC**.** The chemical reaction during sintering showed that thermal explosion (TE) occurs when a small amount of nanosized TiC powder was added forming martensite NiAl laths, $Ni_3Al$ and TiC phases.

Steel/Ni reinforced with 1.0–1.5 wt% TiC composite synthesized by compaction and sintering comprised of the the FCC Steel/Ni matrix for 1.0 wt % TiC- Steel/Ni composite the 1.5 wt% TiC- Steel/Ni composite is comprised of the BCC Steel/Ni phase. The FCC Steel/Ni (1.0 wt% TiC) composite exhibited lower average hardness compared to the B2 Steel/Ni (1.5 wt% TiC) phase.

Titanium oxynitride ($TiO_{2-x}N_x$) formed on the surfaces of spherical Ti powder particles upon heat treatment in air at 500, 600, 700 and 800 °C. At 500 °C a hexagonal closed packed (HCP) $TiO_x$ film was formed while a $TiO_2$ film was observed after annealing at 600 °C and eventually a $TiO_{2-x}N_x$ layer coated the spherical Ti particles at 700 and 800 °C due to N diffusion within the $TiO_2$ crystal lattice.

A ceramic composite material of A356-1Sn-5Ni-($TiO_{2-x}$-$N_x$) composition was developed. The $TiO_{2-x}$-$N_x$ ceramic particles were bonded without forming any intermetallic particles such as $Al_3Ti$ with Ti. The structural analysis showed that a tetragonal $TiO_{2-x}N_x$ with lattice parameters a=4.585 Å; c=2.960 Å, HCP $TiO_x$ phase with lattice parameters a=5.140 Å c=9.480 Å and FCC phase with lattice parameter a=5.572 Å were formed.

UNIVERSITY of the WESTERN CAPE

# TABLE OF CONTENTS



UNIVERSITY of the WESTERN CAPE

http://etd.uwc.ac.za/

http://etd.uwc.ac.za/

# CHAPTER ONE

# 1. INTRODUCTION

## 1.1 GENERAL BACKGROUND AND NEED FOR THE RESEARCH

Although Metal Matrix Composites (MMCs) were initially developed for advanced military systems, they have since found widespread applications in the ground transportation, thermal management, aerospace, industrial, recreational and infrastructure industries **[1]**. The demand for lightweight materials and high mechanical performance has seen MMCs being transformed from a topic of scientific and intellectual interest to a material of broad technological and commercial significance **[1,2]**. MMCs combine the superior attributes offered by their constituents resulting in a material that exhibits a unique balance of physical and mechanical properties. High thermal and electrical conductivity, good resistance to aggressive environments, good impact and erosion resistance, good fatigue and fracture properties coupled with high strength and stiffness as well excellent wear resistance and lower coefficient of thermal expansion is achievable by this class of materials **[2]**.

UNIVERSITY of the
WESTERN CAPE

There is many possible MMC combinations that can be fabricated owing to the number of matrices and reinforcements that are available **[1]**. Aluminium alloy matrix has been the most popular due to its excellent strength/weight ratio, good corrosion resistance and high thermal and electrical conductivity making its use ideal for automotive and aircraft applications **[2,3]**. Aluminium-silicon alloys are the most widely used owing to their commercial availability, possibility to be heat treated, excellent fluidity of which are properties fundamental in all metal-casting processes **[2]**. Continuous and discontinuous reinforcements have been incorporated into aluminium alloys to produce Aluminium Matrix Composites (AMCs). Ceramic particulate reinforcements have received the most

http://etd.uwc.ac.za/

attention due to the high strength, stiffness as well as high temperature stability of ceramics. SiC is the reinforcement of largest commercial use (by volume) by a significant margin, followed by $Al_2O_3$ and TiC **[1]**.

Micro-ceramic particles are used to improve the yield and ultimate tensile strength of the matrix metal but the ductility of MMCs drops with increasing content of reinforcing particles **[4]**. This is due to the tendency of the "larger" particles to occupying the grain boundaries **[5]**. This leads to low fracture toughness, low strength and hardness at high temperatures and poor machinability **[6]**. This has led to the development of nano-ceramic particle reinforcements in Metal Matrix Nano Composites (MMNCs). These particles have the potential to influence the microstructure at the atomic level which could lead to ultra-high-performance materials. There are several fabrication routes for MMNCs which fall into two general categories namely, in-situ and ex-situ. During the ex-situ fabrication, nano particle reinforcement is externally added to the matrix while in-situ synthesis involves the production of reinforcements within the matrix during the processing stage **[6]**. Ex-situ fabrication can be further divided into two categories, solid state and liquid state **[6]**. Fabrication routes of MMNCs include mechanical alloying with high energy milling, ball milling, nano-sintering, vortex process, spray deposition, electrical plating, sol-gel synthesis, laser deposition etc. **[4]**.

UNIVERSITY of the
WESTERN CAPE

Liquid phase casting process of MMNCs can produce components with complex shapes. The route is therefore attractive in production of near net shape lightweight bulk components with uniform reinforcement distribution and structural integrity **[4]**. The major drawback in fabrication of MMNCs has been the difficulty to obtain uniform dispersion of nano-sized ceramic particles in liquid metals due to high viscosity, poor wetability in the metal matrix and a large surface-to-volume ratio which induces agglomeration and clustering **[4–6]**. This is the major reason why liquid state synthesis of MMNCs has proved

http://etd.uwc.ac.za/

less successful despite Duralcan's success in commercialising AlMMCs that are fabricated via liquid state processing. The Advanced Casting Technologies (ACT) research group of the Council for Scientific and Industrial Research (CSIR) has made extensive research in this field. The research group has successfully demonstrated up to 40kg batches of SiC reinforced AlMMCs synthesized via liquid casting with comparable microstructures to the most widely commercially available MMC material, Duralcan **[7]**.

## 1.2 PROBLEM STATEMENT

- **NiAl** alloys are candidates for high temperature structural materials due to high melting point (than Ni based superalloys), low density, high thermal conductivity, and excellent oxidation resistance.

  Despite these attractive attributes, this class of materials exhibits poor room temperature ductility and machinability which has been a major drawback for its use in specialised applications such as aerospace and automobile. Additional second-phase modification for specialised applications such as in gas turbines is thus required for NiAl.

  The current study seeks to fabricate a beta NiAl alloy and further reinforce the alloy with nano TiC or Ti (metal) oxynitride particles and study the resulting microstructure.

- **TiC** is an extremely hard binary compound of Titanium and Carbon used in refractories due to its high melting point (3140 ℃) and good thermal conductivity. The grey-coloured cemented carbide material is extremely wear resistant and its hardness coupled with wear resistance and lubricating properties has made it an attractive material for cutting tools, coating drills punches etc.

UNIVERSITY of the WESTERN CAPE

The large surface area presented by powders and nanoparticles of TiC has led to more effective application of this material as a reinforcement in nano metal matrix composites.

- **Metal Oxynitrides** is an important class of materials that derives unique properties of both the metal oxides and nitrides. Metal oxynitrides have found use as coatings to enhance wear and corrosion resistance, pigments, magnets and their most researched application being in photocatalysis for energy production, degradation of pollutants etc.

Steel was also considered additionally to NiAl as a matrix for the current study.

- **Steel** was not necessarily considered as means to compare with NiAl as a matrix but to increase the scope of use of this versatile and mostly widely used structural material. Steel is by far the most recycled material as it undergoes recycling without compromise in its performance. Further widening the scope of this versatile and hugely recyclable material through enhancing its already impressive mechanical properties will thus have very positive effect on the environmental conservation.

UNIVERSITY of the
WESTERN CAPE

## 1.3 OBJECTIVES OF THE RESEARCH

The specific objectives for this research are:

- To synthesize NiAl alloy via powder consolidation of elemental Ni and Al powders and study the resulting alloy structure
- To synthesize a TiC reinforced NiAl based alloy and study the resulting composite structure
- To synthesize a suitable metal oxynitride and study the resulting structure
- To synthesize a NiAl based alloy reinforced with the suitable metal oxynitride and study the resulting composite structure
- To synthesize a steel-based alloy matrix reinforced with,
    - TiC and study the resulting composite structure
    - the suitable metal oxynitride and study the resulting composite structure

## 1.4 RESEARCH LAYOUT

This research is partitioned into four chapters.

UNIVERSITY of the WESTERN CAPE

- Chapter one: General background and need of the research which gives a bird's eye view on metal matrix composites as a subject of research, a problem statement which contextualizes the need to conduct this research, the objectives of the research which gives a concise scope of what the research seeks to achieve as well as the research layout on how the work is presented in this thesis.
- Chapter two presents literature review about NiAl as a matrix alloy for the current study. Techniques used to improve properties of NiAl are also presented. Steel as matrix for metal matrix composites is considered and finally, a special class of materials namely, metal oxynitrides is reviewed.

http://etd.uwc.ac.za/

- Chapter three presents the synthesis of NiAl, Titanium Oxynitrides and Metal Matrix Composites of interest.
- Chapters four to eight shows results and discussion broken up in into five studies as per the objectives of the overall study, namely:
    - Investigation into the thermal behaviour of the B2–NiAl intermetallic alloy produced by compaction and sintering of the elemental Ni and Al powders
    - Characterization of the $Ni_{62.5}Al_{37.5}TiC_{1.28}$ composite produced via cold pressing and sintering process
    - Microstructure and hardness of Steel/Ni–TiC composite produced by compaction and sintering
    - Surface characterization and formation mechanism of the ceramic $TiO_{2-x}N_x$ spherical powder induced by annealing in air
    - Low temperature synthesis and characterization of (A356Al, Sn, Ni, Ti) ON ceramic composite
- Chapter nine presents the Concluding Remarks and Future Work.

UNIVERSITY of the
WESTERN CAPE

# CHAPTER TWO

# 2. LITERATURE REVIEW

## 2.1 NICKEL ALUMINIDES

NiAl alloys have been a subject of great research for a number of studies due to their high melting point, low density, good thermal conductivity and excellent oxidation resistance **[8]** which makes them excellent candidates for structural materials **[9–19]**. According to Bochenek et al.,**[14]** due to the growing need for advanced materials solutions in the aerospace industry, NiAl alloys have regained more attention after decline of the scientific reports on NiAl bulk material development in the beginning of the 21st century **[11,14–18,20]**.

### 2.1.1 Synthesis of NiAl Alloys

Recent literature studies reveal that powder metallurgy (PM) consolidation techniques have been the most widely used to fabricate NiAl intermetallic alloys. Of the PM processing routes, mechanical alloying (MA) has received lots of attention as a technique for producing homogeneous and possible ductile of otherwise brittle intermetallics via grain refinement. According to Hadef **[21]**, Joadar et al., conducted MA of equiatomic elemental Ni and Al powder blend and reported that the formation of NiAl required ~200 kJ $kg^{-1}$ as well as ~550 kJ $kg^{-1}$ for completion in a stainless steel grinding media as mapped in figure 2.1.

UNIVERSITY of the WESTERN CAPE

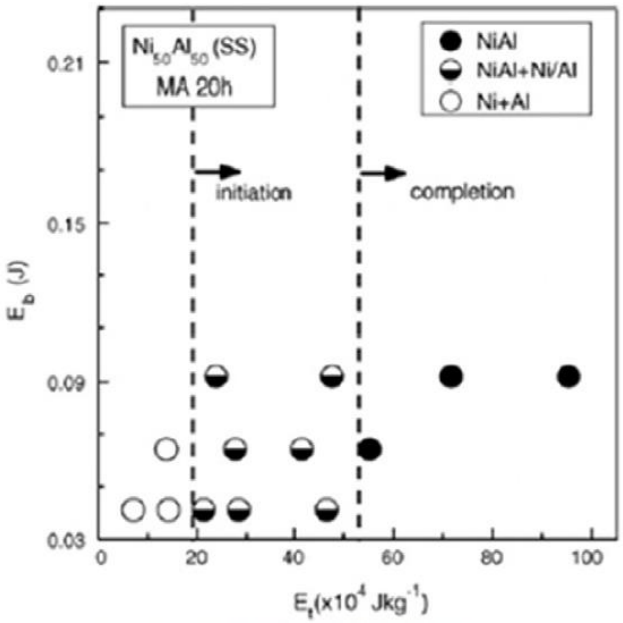


**Figure 2.1**: Milling map for NiAl formation on MA of Ni50Al50 with stainless steel media **[21]**.

In their efforts to synthesize NiAl intermetallics with improved mechanical properties via reduction of crystallite size, Chen et al., **[22]**, Krasnowski et al., **[9,10]** Liu et al., **[23]** used mechanical alloying of elemental Ni and Al powders followed by hot pressing. Recently, Ayodele at al. **[24]** reported on the successful synthesis of NiAl with varying degrees of density (via MA of elemental Ni and Al powders) owing to the subsequent spark plasma sintering of the MA product at different heating rates up to 1000 °C under 50 MPa of pressure. Recently, Biranvand et al., **[25]** concluded that the long-range order parameter decreases (table 2.1) to 0.65 with increasing the milling time to 50 h which is contrary to what Liu et al., **[23]** concluded in 2014 during MA of elemental Ni and Al powders where it was reported that the long range order parameter gradually increases (Figure 2.2 a) from 0.45 at 20 h to 0.6 at 70 h. Chen et al., **[22]** had earlier concluded that during MA of elemental Ni and Al powders, long-range order parameters of powders mechanically

UNIVERSITY of the WESTERN CAPE

alloyed for different times were decreased (Figure 2.2 b) from 0.82 after 5 h to 0.63 after 48 h which is in agreement with Biranvand **[25]**.

**Table 2.1**: Long range order parameter and rα of the B2-NiAl at various mechanical alloying times **[25]**.

| $r_\alpha$ | LRO | Mechanical alloying time (hours) |
|---|---|---|
| 1 | 1 | 30 |
| 0.830 | 0.660 | 40 |
| 0.825 | 0.650 | 50 |

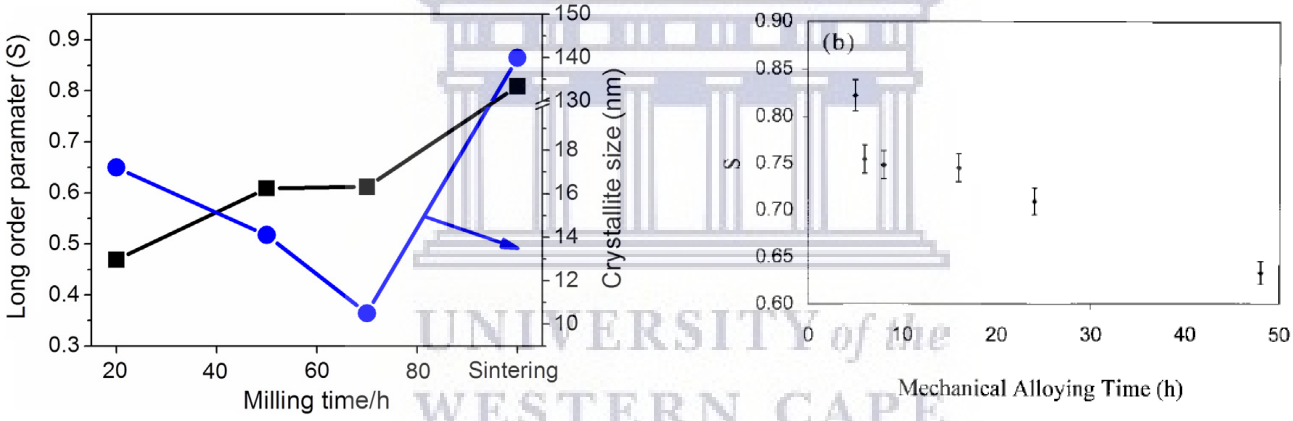


UNIVERSITY of the WESTERN CAPE

**Figure 2.2**: The variation of long-range order parameter of NiAl powders with the milling time according to a) Liu et al., **[23]** and b) Chen et al., **[22]**.

A number of research studies have taken advantage of the properties of the reaction that ensues when Ni and Al are ignited and spontaneously form NiAl intermetallic product in what is referred to as self-propagating high-temperature synthesis (SHS) due to the free energy for the formation of the intermetallic **[25]**. In 1992 Subrahmanyam et al., **[26]** conducted a review on SHS as a process being developed worldwide for fabrication of powders and near-net shape components. The study highlights adiabatic temperature,

$T_{ad}$ as a critical parameter for SHS reaction and Merzhanov made a physico-chemical classification (Table 2.2) of SHS mechanisms for a binary system based on the adiabatic, melting, and boiling temperatures of reactants. In 2019, Yunmao et al., **[27]** used combustion in SHS synthesis and space holder method of elementary Ni, Al and NaCl to fabricate a highly porous (>80%) single phase NiAl with a hierarchical open-cell structure via controlled sintering conditions and volume fraction of the space holder NaCl. Zhao et al., **[28]** used combustion and hot pressing in SHS to fabricate NiAl intermetallic alloy with true ultimate compression strength of $1002^{+72}_{-94}$ MPa, fracture strain of 21.6±1.8%, work-hardening capacity (Hc) of $1.40^{+0.09}_{-0.074}$ and the Vickers micro-hardness is $360^{+15}_{-19}$ HV. Ozdemir et al., **[29]** determined that the combustion reaction between aluminium and carbonyl-nickel occurs at 655 °C to form NiAl intermetallic in open air under 150 MPa uniaxial pressure.

UNIVERSITY of the
WESTERN CAPE

**Table 2.2**: Physicochemical classification of SHS reaction mechanisms for a two component system **[26]**.

| Relation between $T_{ad}$, $T_m$ and $T_b$ | Characteristics of the system | Examples |
|---|---|---|
| 1. $T_{ad} < T_b^i$ $i = 1, 2$ | Ideal gas free combustion occurs if $[P(T_{ad})/P_o] \rightarrow 0$ | 1. $Ti + 2B = TiB_2$<br>$T_{ad} = 3200$ K ($T_o = 293$ K)<br>$P_{Ti}(3200\ K) = 8$ kPa<br>$P_B(3200\ K) = 0.4$ kPa<br>Gasless reaction only at high pressures<br>2. $Mo + B = MoB$<br>$T_{ad} = 1750$ K ($T_o = 293$ K)<br>$P_{Mo}(1750\ K) = 10^{-7}$ Pa<br>$P_B(1750\ K) = 10^{-6}$ Pa<br>Gasless reaction even in high vacuum |
| 2. $T_m^i < T_{ad} < T_b^i$ $i = 1, 2$ | Both components in liquid state | $Ni + Al = NiAl$<br>$T_{ad} = 1910$ K<br>Ni: $T_m$(K) 1726, $T_b$(K) 3373<br>Al: $T_m$(K) 933, $T_b$(K) 2773 |
| 3. $T_m^1 < T_{ad} < T_m^2$ | Solid + liquid reaction. Highest propagation velocity | $Ti + C = TiC$<br>$T_{ad} = 3210$ K<br>$T_m^{Ti} = 1933$ K<br>$T_m^C = 3973$ K |
| 4. $T_{ad} < T_m^i (i = 1, 2)$ | Both components in solid state. Lowest combustion velocity. Difficult combustion | $2Ta + C = Ta_2C$<br>$T_{ad} = 2600$ K $T_m^{Ta} = 3269$ K<br>$Ta + C = TaC$<br>$T_{ad} = 2700$ K |
| 5. $T_b^1 < T_{ad} < T_b^2$ | One component in the gaseous phase and the other in condensed state. Widely used process | Formation of nitrides, hydrides, sulphides, selenides, phosphides etc. |
| 6. $T_{ad} > T_b^i$ $i = 1, 2$ | Both reactants in gas phase and solid product | Very few systems studied. Mg + S |

In 2017, Fan et al., **[30]** used SHS to fabricate NiAl alloy which they plasma sprayed onto the magnesium (MB26) alloy substrate to enhance its thermal barrier capacity with excellent bond stability. Depending on the energy generated (as determined by the milling medium) during by the mechanical alloying of elemental Al and Ni powders, synthesis of NiAl intermetallic my occur via mechanically induced self-propagating reaction (MSR) **[31]** or via gradual formation through continuous diffusive reaction at Ni/Al layers interfaces **[32]**. Mechanical alloying may not only result in enough energy to cause (MSR) but may also result in partial martensitic transformation of B2-NiAl to tetragonal L10-NiAl during prolonged milling of elemental Ni and Al powders in planetary mill **[33]**. Kubaski et al., **[34]** published a study on how the synthesis of NiAl intermetallic compound fabricated via mechanically induced self-propagating reaction during high energy milling of elemental Ni and Al powders is effected by the milling variables.

UNIVERSITY of the WESTERN CAPE

Recently, Sun et al., **[35,36]** used forming and reaction synthesis to fabricate thin walled curved shell NiAl alloy components via forming of laminated alternating Ni and Al foils in a mould (figure 2.3) followed by reaction synthesis at specified temperature and pressure.

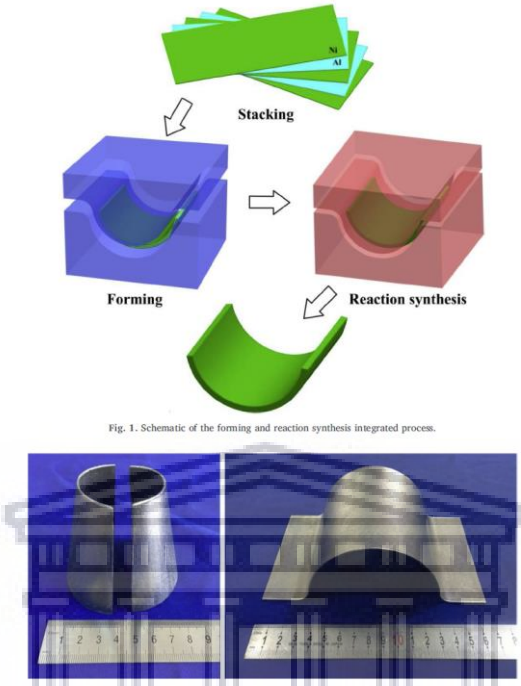


Fig. 1. Schematic of the forming and reaction synthesis integrated process.

**Figure 2.3**: NiAl alloy thin-walled component manufactured by the integrated process **[36]**.

UNIVERSITY of the
WESTERN CAPE

For the current study, B2–NiAl intermetallic alloy was synthesized by compaction and sintering of elemental Ni and Al powders and the thermal behaviour of the alloy was studied. The study (presented in chapter four) was then published in a peer-reviewed journal.

Despite these excellent inherent properties, Ni-Al suffers from poor room temperature ductility and machinability which limits their use in specialised applications such as aerospace and automobile **[9,12,14]**. There has been an increased research attention to improve the formability of this class of materials, and grain refinement of NiAl microstructures has been investigated. Bochenek et al., **[14]** presented an overview of

research on NiAl processing and indicated methods that are promising in solving the low fracture toughness of this intermetallic alloy at room temperature. In the same overview, other material properties relevant for high temperature applications are also addressed.

### 2.1.2 Grain Refinement of NiAl

Various studies have been aimed at fabricating NiAl structures with nano crystalline **[9-12,22,23,31–34,37]** grain size to improve their ductility or formability. Grain refinement in NiAl has been achieved via a carefully controlled fabrication route, addition of refiners as well as precipitate strengthening.

Powder consolidation fabrication routes whereby elemental powders are premixed, milled below a nanocrystalline size range followed by controlled high pressure sintering with limited grain growth have been explored. Using this fabrication route, Krasnowski et al., produced a NiAl intermetallic alloy with a mean crystallite size of 13 nm upon milling of Ni-50% Al powder mixture **[9]**. The pre-milled intermetallic alloy powder was sintered at 800°C under 900 GPa of pressure. The high-pressure sintering preserved the nanometric crystallite size with limited grain growth to 24 nm resulting in a nanocrystalline NiAl intermetallic alloy with improved hardness of 9.53 GPa. The milling time to achieve optimal starting crystallite size is a critical determining factor in achieving a nanocrystalline material and Krasnowski et al., estimated the mean crystallite size at various fabrication stages of the NiAl polycrystalline alloy, figure 2.4.

UNIVERSITY of the WESTERN CAPE

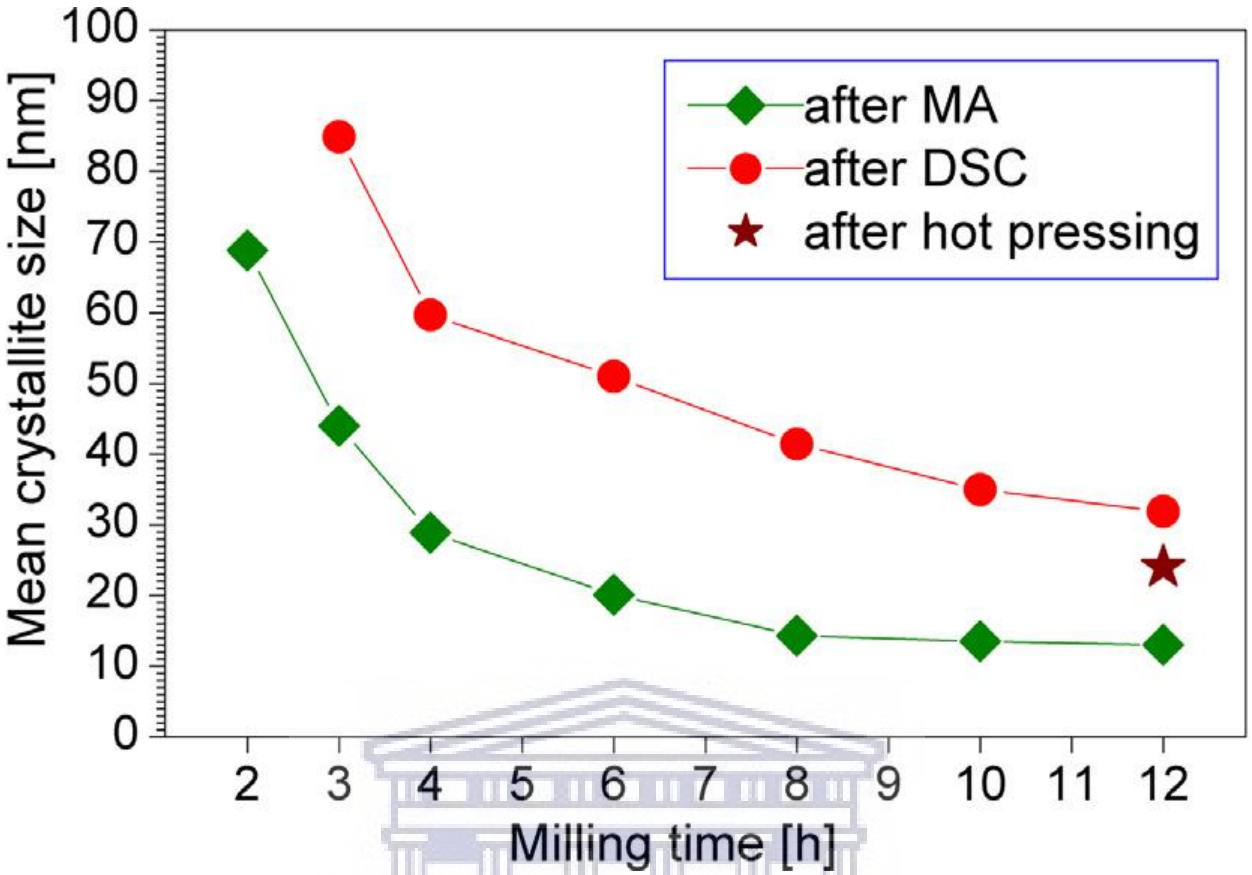


**Figure 2.4**: Estimated mean crystallite size of NiAl after various milling times, after DSC examinations and after consolidation **[9]**.

UNIVERSITY of the
WESTERN CAPE

Addition of Boron and transition elements has been found to result in grain refinement of NiAl microstructures. In another study, Krasnowski et al., makes the claim that they have fabricated bulk NiAl-B composites with nanocrystalline intermetallic matrix for the first time via milling of equiatomic NiAl powders with the addition of 5, 10, 20 and 30 vol% of boron **[10]**. The study concludes that a decrease in grain size, an increase in hardness as well as decrease in the NiAl-B composites was achieved with an increase in Boron content.

In their study, Albiter et al., used the additions of transition metals such as Fe, Ga, and Mo on elemental Ni and Al powder mixture followed by mechanical alloying to achieve a refined B2 NiAl structure followed by a hot pressing technique **[12]**. The refined structures

achieved up to 22% deformations for the NiAl intermetallic alloy hot pressed at 1200°C (Table 2.3).

**Table 2.3**: Mechanical properties measurements (strain rates, stress and yield strength) from all the alloys prepared under two different hot pressing conditions **[12]**.

| Composition (at.%) | Temperature/time (°C/min) | Strain (%) | Maximum stress (MPa) | Yield strength (MPa) |
|---|---|---|---|---|
| Al–44Ni | 1200/30 | 11.8 | 2030 | 1532 |
| Al–43Ni+2Fe | 1200/30 | 15 | 2536 | 1645 |
| Al–42Ni+6Fe | 1200/30 | 22.1 | 2861 | 1678 |
| Al–43Ni+2Ga | 1200/30 | 9.1 | 1967 | 1715 |
| Al–41Ni+6Ga | 1200/30 | 9.0 | 2759 | 1980 |
| Al–42Ni+2Mo | 1200/30 | 9.9 | 2322 | 1693 |
| Al–41Ni+6Mo | 1200/30 | 7.1 | 2294 | 2055 |
| Al–42Ni+2Fe+2Ga | 1200/30 | 14.5 | 2090 | 1591 |
| Al–40Ni+2Fe+6Ga | 1200/30 | 11 | 2122 | 1745 |
| Al–40Ni+6Fe+2Ga | 1200/30 | 17.5 | 2621 | 1546 |
| Al–39Ni+6Fe+6Ga | 1200/30 | 15 | 2377 | 1621 |
| Al–42Ni+2Fe+2Mo | 1200/30 | 8.9 | 2222 | 1884 |
| Al–40Ni+2Fe+6Mo | 1200/30 | 12.2 | 2522 | 1932 |
| Al–40Ni+6Fe+2Mo | 1200/30 | 19.2 | 2520 | 1496 |
| Al–39Ni+6Fe+6Mo | 1200/30 | 15 | 2476 | 1862 |
| Al–42Ni+2Mo+2Ga | 1200/30 | 8.9 | 1933 | 1597 |
| Al–40Ni+6Mo+2Ga | 1200/30 | | | |
| Al–40Ni+2Mo+6Ga | 1200/30 | | | |
| Al–39Ni+6Mo+6Ga | 1200/30 | 12.8 | 2456 | 1710 |
| Al–44Ni | 1500/15 | 9.7 | 1604 | 1230 |
| Al–43Ni+2Fe | 1500/15 | 13.6 | 1737 | 1472 |
| Al–42Ni+6Fe | 1500/15 | 19.9 | 2322 | 1165 |
| Al–43Ni+2Ga | 1500/15 | | | |
| Al–41Ni+6Ga | 1500/15 | 9.2 | 1560 | 1300 |
| Al–42Ni+2Mo | 1500/15 | 8.6 | 1869 | 1560 |
| Al–41Ni+6Mo | 1500/15 | 8.8 | 1930 | 1400 |
| Al–42Ni+2Fe+2Ga | 1500/15 | 12.6 | 2140 | 1348 |
| Al–40Ni+2Fe+6Ga | 1500/15 | | | |
| Al–40Ni+6Fe+2Ga | 1500/15 | 21 | 2103 | 1233 |
| Al–39Ni+6Fe+6Ga | 1500/15 | 11.2 | 1565 | 1146 |
| Al–42Ni+2Fe+2Mo | 1500/15 | 20 | 2240 | 1281 |
| Al–40Ni+2Fe+6Mo | 1500/15 | 12 | 1932 | 1520 |
| Al–40Ni+6Fe+2Mo | 1500/15 | | | |
| Al–39Ni+6Fe+6Mo | 1500/15 | 22 | 2639 | 1357 |
| Al–42Ni+2Mo+2Ga | 1500/15 | 15.5 | 1875 | 1208 |
| Al–40Ni+6Mo+2Ga | 1500/15 | 11.4 | 1872 | 1287 |
| Al–40Ni+2Mo+6Ga | 1500/15 | | | |
| Al–39Ni+6Mo+6Ga | 1500/15 | 11 | 1770 | 1380 |

UNIVERSITY of the WESTERN CAPE

It would thus be important to determine how the mechanical properties of NiAl vary as a function of grain size, whether they follow the classical Hall-Petch relation indefinitely or there is a critical grain size where the properties saturate. In 1999, Chen et al., **[22]** concluded that the increase in microhardness of the B2 NiAl intermetallic (synthesized via mechanical alloying of elemental Ni and Al powders followed by shock consolidation)

followed Hall-Petch behaviour. Volpp et al., synthesized nanocrystalline NiAl via mechanical alloying of a stoichiometric mixture of gas-atomized $Ni_3Al$ and Ni-76 at.% Al powders in a high energy ball mill and measured hardness on the as milled and heat treated samples to investigate the applicability of a Hall-Petch type relationship in nanocrystalline B2 NiAl **[37]**. The study concluded that the hardness follows a Hall-Petch behaviour down to a grain size of about 20 nm below which deviations from the "classical" behaviour is observed. Depending on the thermo-mechanical history of the samples;

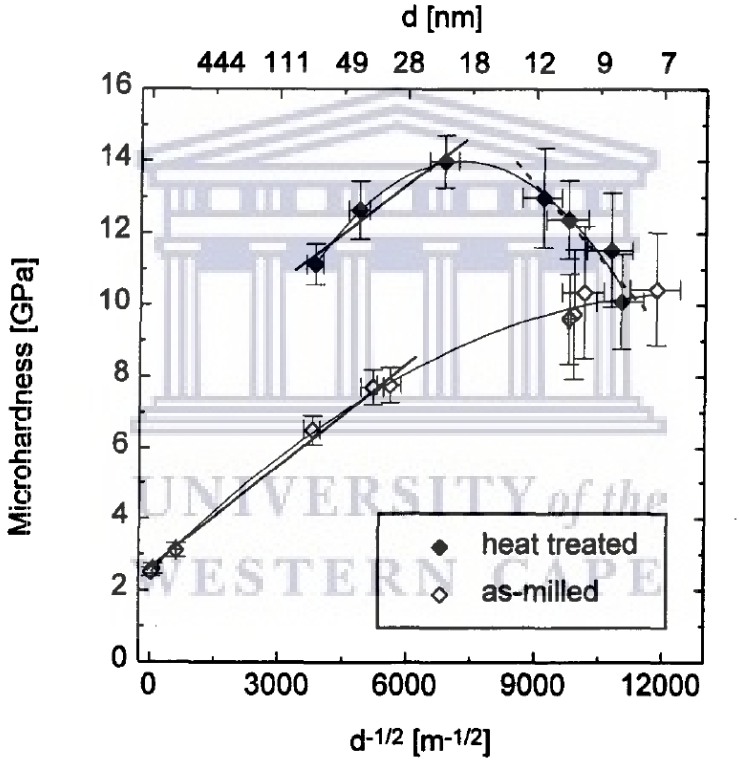


heat-treated powders exhibit "inverse" Hall-Petch behaviour, whereas the hardness of as-milled powders only saturates at a grain size of about 10 nm, figure 2.5.

**Figure 2.5**: Microhardness values for as milled and for heat-treated powders as a function of l/Jd. Full lines indicate Hall-Petch behaviour; dashed line corresponds to "inverse" Hall-Petch behaviour, observed for heat-treated powders only **[37]**.

http://etd.uwc.ac.za/

Despite efforts to improve ductility of NiAl via grain refinement, the near zero plasticity at room temperature coupled with low temperature strength above 800 °C has limited the use of polycrystalline NiAl **[38]**.

### 2.1.3 Alloying of NiAl

Addition of other metals coupled with fabrication techniques to further improve the mechanical properties of NiAl intermetallics have been reported. According to literature compiled by Zaitsev et al., **[38]**, alloying elements for NiAl can be sub-grouped into three categories (Table 2.4).

**Table 2.4**: Elements used for alloying NiAl-based alloys **[38]**.

| *Elements* | *Solubility in NiAl* | *Interaction with NiAl* |
|---|---|---|
| ***Gr VIII, Mn and Cu*** | Highly soluble | Prone to forming isostructural compounds. |
| ***Gr VIB, V and Re*** | Low solubility | Form pseudobinary eutectic systems with stoichiometric NiAl, while the increased alloy plasticity is ensured by formation of the lamellar eutectic structure. |
| ***Gr IIB, IVB and VB*** | Very limited solubility | Form ordered ternary intermetallic compounds, such as Heusler phases $Ni_2AlX$ and Laves phases NiAlX, which have a positive effect on high-temperature characteristics of the alloy. |

UNIVERSITY of the WESTERN CAPE

García-Galán et al., **[39]** reported that maximum modulus of elasticity (figure 2.6a), displacement at break (figure 2.6b) and bending strength (figure 2.6c) peaked at 7.5 at.% Cu for nanocrystalline NiCuAl powders prepared via MA of elemental Ni, Al and Cu powers consolidated by double action pressing at 1.20 GPa and sintered at 1000 °C.

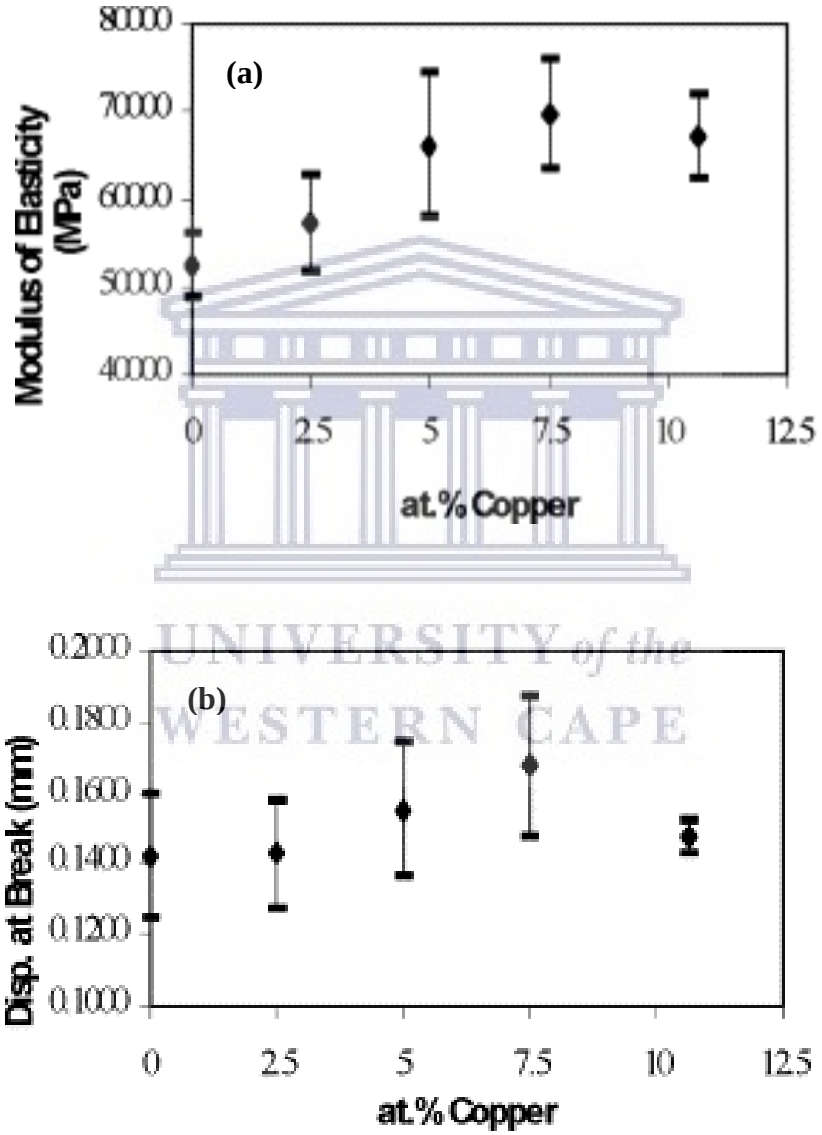


UNIVERSITY of the WESTERN CAPE

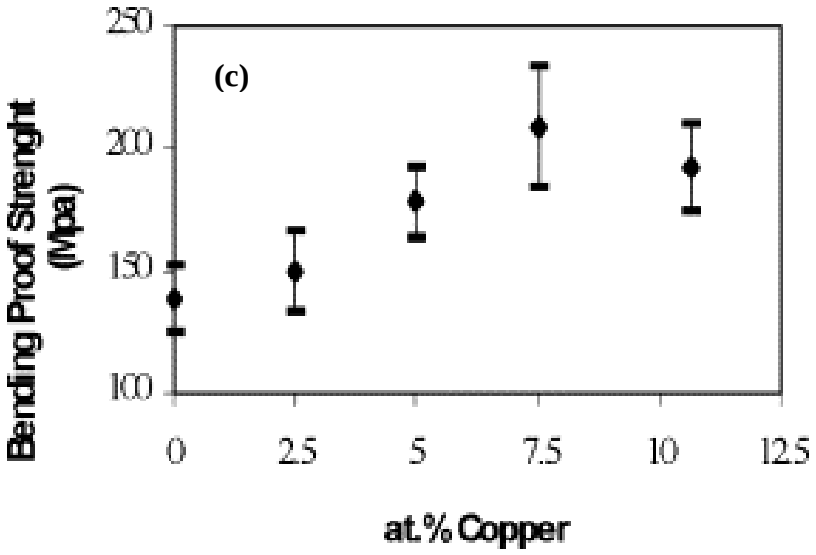


**Figure 2.6**: a) Modulus of elasticity, b) Displacement at break and c) Bending proof strength as a function Cu additions into NiAl **[39]**.

Bochenek et al., **[40]** used hot pressing and spark plasma sintering to fabricate NiAl/Re with almost full (99.9%) density, 60% improvement in fracture toughness and almost double the flexural strength of NiAl and no significant changes during oxidation at 900, 1100 and 1300 °C.

UNIVERSITY of the
WESTERN CAPE

As reported previously, Krasnowski et al., **[10]** successfully produced NiAl phase with boron particles (5, 10, 20 and 30 vol%) evenly embedded within the nanocrystalline NiAl matrix. Increase in boron content resulted in decrease of the NiAl grain size during milling as well decrease in density (rule of mixtures) of the alloy. Improved hardness (10.58 - 12.60 GPa) was derived from the addition of boron. According to the researchers, “bulk NiAl-B composites with nanocrystalline intermetallic matrix were produced for the first time”.

Albitera et al., **[12]** synthesized NiAl intermetallic with grains refined into the nanometric range (20 nm) via the additions of transition elements such as Fe, Ga, and Mo during

http://etd.uwc.ac.za/

mechanical alloying and densification via hot pressing techniques. According to the investigators, these minor additions of the transition elements form a solid solution (B2) with the intermetallic structure of NiAl resulting in up to 22% deformations.

UNIVERSITY of the
WESTERN CAPE

http://etd.uwc.ac.za/

## 2.2 NICKEL ALUMINIDES METAL MATRIX COMPOSITES

Powder metallurgy (PM) techniques used to fabricate NiAl intermetallic alloy discussed above have been extended to synthesize in-situ as well as ex-situ ceramic particle reinforced NiAl. This endeavour seeks to achieve ceramic particles (reinforcement) evenly dispersed in the microstructure of a continuous NiAl matrix to improve ductility of NiAl intermetallic alloy. TiC **[16,41]**, $Al_2O_3$ **[8,42,43]**, $TiB_2$ **[44]**, TiC/$TiB_2$ **[15,20,45,46]**, TiC/$Al_2O_3$ **[17]**, $TiB_2$/$Al_2O_3$ **[47]**, $TiB_2$/TiN **[48]** and carbon nanotubes **[18,49,50]** are some of the reinforcements used to reinforce NiAl to fabricate NiAl intermetallic alloy matrix composites.

### 2.2.1 Ex-situ fabrication

During ex-situ synthesis of metal matrix composites, a reinforcing ceramic phase is externally added into the metal matrix during liquid state casting or solid-state fabrication. Recently Talas et al., **[20]** fabricated NiAl reinforced with either TiC of $TiB_2$ in the range 0.5, 1, 2, 4 and 8 wt % via ex-situ compacting of premixed Ni, Al and either TiC or $TiB_2$ powders followed by melting in vacuum. Talas reported an improved hardness of the composite with increasing content of TiC or $TiB_2$ which dropped significantly upon heat treatment of the composite attributable to a possible particle sizes and interparticle distance increased by coarsening. The investigation does not report on the ductility/deformability of the as cast and heat-treated composite samples. Li et al., **[51]** synthesized NiAl-BaO/$TiO_2$ composite via ball milling of NiAl intermetallic, BaO and $TiO_2$ powders followed by sintering at 1300°C for 1 h under a pressure of 20 MPa. The 20% BaO /$TiO_2$ composite exhibited microhardness and yield strength of 474.5 and 2786 MPa respectively with a decrease in the friction coefficient and wear rate at 800°C. In 2018, in an unconventional reinforcement/matrix setup Sonber et al., **[19]** used NiAl as a

UNIVERSITY of the WESTERN CAPE

reinforcement for $ZrB_2$ and concluded that an increase in the content of NiAl resulted in decrease in hardness and an increase in fracture toughness. It is thus judicious to conclude that by classical definition of the matrix-reinforcement, NiAl is the matrix while the $ZrB_2$ is the reinforcement in the setup.

### 2.2.2 In-situ fabrication

During in-situ synthesis of metal matrix composites, a chemical reaction leads to the formation of very fine and thermodynamically stable reinforcing ceramic phase within a continuous metal matrix. Feedstocks have been used during self-propagating high-temperature synthesis (SHS) to achieve microstructures with in-situ reinforcement particles homogeneously distributed within NiAl intermetallic matrix. Fan et al., **[15]** and Shen et al., **[45]** used SHS of Ni–Al–Ti–$B_4C$ feedstock to in-situ fabricate NiAl-TiC-$TiB_2$ intermetallic matrix composite. Zhang et al., **[11]** in-situ synthesized $TiB_2$ reinforced NiAl with 35.2% increase in room temperature compressive strength via arc melting of Ti-B-Ni-Al system. The reaction process was found to proceed in two steps: firstly, Ni, Al reacted with Ti to form transient phase $AlNi_2Ti$, and then $AlNi_2Ti$ reacted with B to form $TiB_2$ particles, which serve as reinforcements with a uniform distribution within the NiAl matrix. On another study, Zhao et al., **[52,53]** used Ni–Al–Nb–$B_4C$ system to fabricate $NbB_2$–$Nb_xC$/NiAl composite via the combustion synthesis and hot pressing technique. In 2011, Zhao et al., **[52]** reported on the microstructures, interfaces, compression properties and work-hardening effect of the resulting NiAl-matrix composites reinforced with 5-20 wt.% ceramic particulates ($Nb_2C$, NbC and $NbB_2$) noting that an increase in the ceramic particulate content resulted in increase in the ultimate and yield compression strengths while the fracture strain and hardening (Hc) decreased. The researcher concluded that the composite with the least (5%) amount of particulate exhibited the best combination of mechanical properties: compression fracture strain of 18.3%, an ultimate

UNIVERSITY of the WESTERN CAPE

compression strength of 1479 MPa, and a value of Hc =1.29. Zhao et al., **[53]** conducted a similar investigating on NiAl matrix composite reinforced with 1.7 wt.% $NbB_2$ and $Nb_xC$ (x =1 or 2) fabricated using the same technique. The NiAl-matrix composite showed a strong strain rate sensitivity whereby yield strength of the $NbB_2$–$Nb_xC$/NiAl composite decreases while the fracture strain and the work-hardening capacity (Hc) increase with decreasing strain rate. Compression fracture strain of 20.1%, an ultimate compression strength of 1472 MPa, and a value of Hc =1.41 was achieved with reduced volume fraction of the reinforcement at a strain rate of 2.0 x $10^{-5}s^{-1}$. Zhao et al., **[54]** also studied the microstructure, compression property and work-hardening effect of the NiAl-matrix composite reinforced by 5 vol.% TaB and $TaB_2$ fabricated via combustion synthesis of Ni-Al-Ta-B system. The researchers arrived at similar conclusions that NiAl-matrix composite exhibits remarkable strain-rate-dependent compression properties and work-hardening effect.

Song et al., **[47]** used SHS of Ni, Al, $B_2O_3$ and $TiO_2$ premixed and green compacted powders to synthesize ($TiB_2$+$Al_2O_3$)/NiAl composites of 2−5 μm $TiB_2$ grains embedded in $Al_2O_3$ clusters, while a small number of $TiB_2$ particles disperse in the NiAl matrix according to the schematic microstructural evolution depicted in figure 2.7. The investigators go on to postulate - “the higher the $TiB_2$+$Al_2O_3$ content is, the more the regular shapes and homogeneous distributions of $TiB_2$ and $Al_2O_3$ will be present in the NiAl matrix”.

UNIVERSITY of the WESTERN CAPE

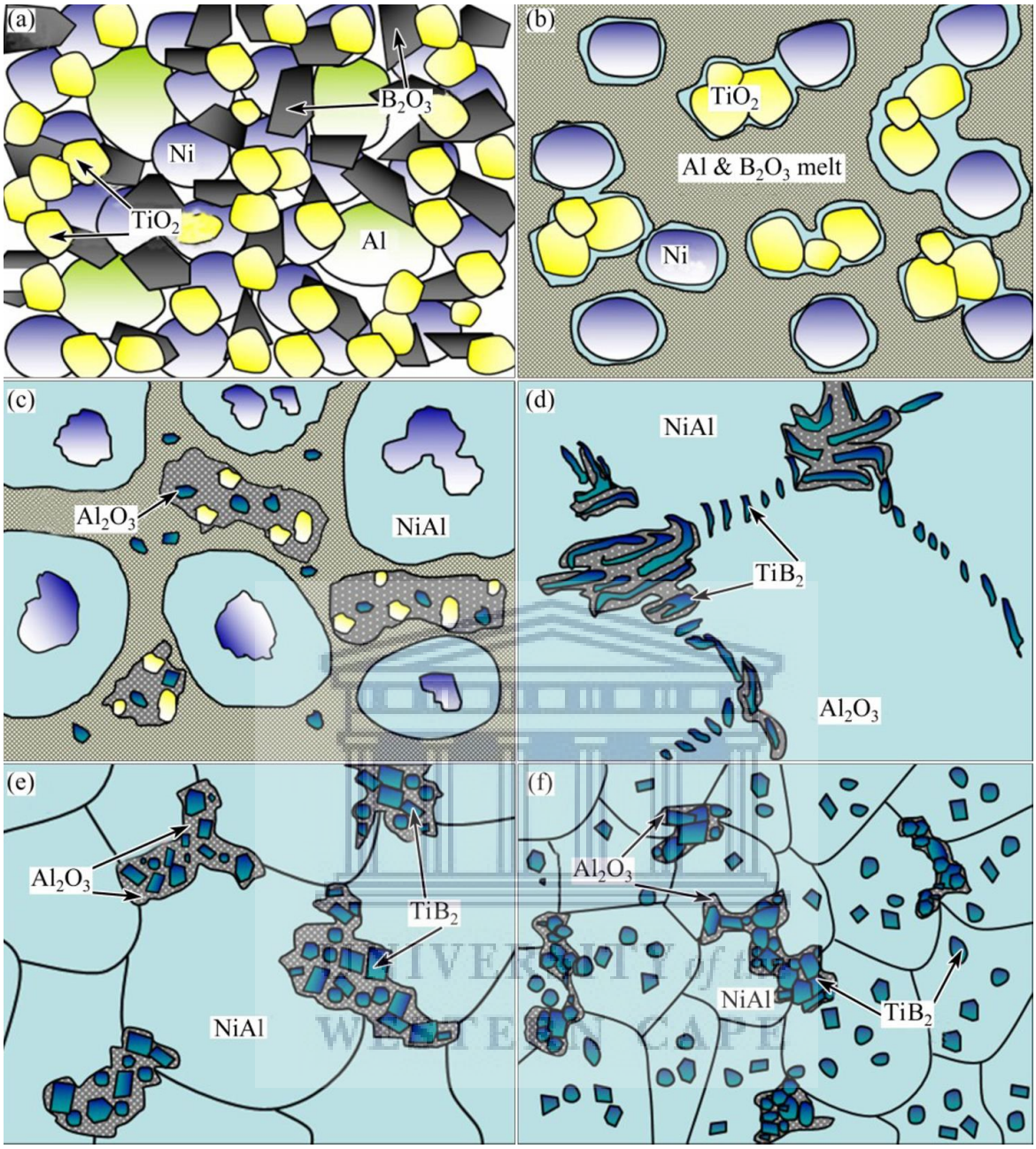


**Figure 2.7**: a) Sketch of reaction processes and structure evolution modes: (a) Mixed initial powders; (b) Al and $B_2O_3$ begin to melt; (c) Grains of NiAl, $TiB_2$ and $Al_2O_3$ formatting; (d−f) Morphologies of products with 10%, 20% and 30% (Al+$TiO_2$+$B2O_3$), respectively **[47]**.

Similarly, Shokati et al., **[48]** fabricated NiAl matrix composite powder reinforced with 0–40 wt.% ($TiB_2$–TiN) from Ni, Al, Ti and hexagonal boron nitride (h-BN) powders via combustion synthesis. The first reaction between Ni and Al caused an energy release

http://etd.uwc.ac.za/

which melted Al(Ni), Ni, NiAl and Ti and decomposed BN into free B and N which in turn diffused and dissolved into the Ni-Al–Ti liquid phases. Finally, TiN and $TiB_2$ particulates precipitate out of the saturated solution. Good bonding between reinforcement and matrix, increased and uniformity of distribution of reinforcements in NiAl matrix and formation of sub-micron $TiB_2$ and TiN embedded in NiAl matrix resulted in high hardness making this composite powder a good precursor for thermal spray applications.

Rahaei **[16]** achieved improved mechanical properties (Table 2.5) compared to those documented in literature and deduced that ±28 vol.% TiC content in 3D space of the continuous NiAl matrix leads to attainment of discrete TiC particles. Feasibility of heat transfer and decreasing of thermal stress in comparison with long-range interconnectivity of TiC particles in NiAl-TiC (bi-continuous) composite makes this composite a good candidate material for high temperature applications.

UNIVERSITY of the
WESTERN CAPE

**Table 2.5**: Mechanical properties of NiAl intermetallic and Ni-Al-TiC composite achieved by Rahaei **[16]** compared to previous studies.

| Mechanical Properties | This research | Literature (Ni-Al-X vol.% TiC Composite) |
|---|---|---|
| Hardness (Hv) | $391 \pm 20_{(x=0)}$, $899 \pm 78_{(X=28)}$ | $374 \pm 15$ [59], 311–425 [2] NiAl coarse $grain_{(X=0)}$, $909 \pm 79_{(X=30)}$ [59] Ni-Al-TiC |
| $G_f$ (MPa) | $548 \pm 49_{(x=0)}$, $733 \pm 78_{(X=28)}$ | $425–700_{(X=0)}$ [2] $670 \pm 80_{(x=80)}$ [47], $665 \pm 26$ [52] |
| $K_{IC}$ (MPa$\sqrt{m}$) | $6.2 \pm 0.3_{(x=0)}$, $9.9 \pm 0.8_{(x=28)}$ | $5–6.5_{(x=0)}$ [2] NiAl, $8.9_{(X=20)}$ [33], $10.7 \pm 0.5_{(X=70)}$ [48], $10.23 \pm 0.38$ [52] Ni-Al-TiC |

Widodo et al., **[17]** concluded that the exothermicity of the system increases with addition of $TiO_2$/Al/C content into NiAl. This resulted in increased maximum reaction temperature

porosity during in-situ fabrication of NiAl-TiC-$Al_2O_3$ intermetallic ceramic composite via self-propagation synthesis using Ni, Al, C and $TiO_2$ as precursors. The reactions occur in two stages whereby exothermic reaction of Ni and Al leads to the formation of NiAl followed by $TiO_2$, Al, and C forming TiC-$Al_2O_3$. Olusoji et al., **[18]** arrived at a similar conclusion that high sintering heating rate resulted in porosity due to lack of contact area between particles during ex-situ fabrication of multi-walled carbon nanotubes (CNT) reinforced NiAl fabricated via planetary ball milling of Ni, Al and CNT elementary powders followed by spark plasma sintering at 50, 100 and 150 °C/min **[50]**. Recently, Troncy et al., **[8]**, aluminothermically reacted pre-oxidized Ni with Al to fabricate mixed compounds of $Ni_xAl_y$ containing in-situ continuous generated network of $Al_2O_3$ surrounding $Ni_xAl_y$ intermetallic compounds in a composite that has a potential to form self-healing coatings.

### 2.2.3 Enhanced tribology of NiAl composites

Self-healing/lubricating is a technique that has been used to improve tribological properties of various materials and silver has been added to various microstructures as its malleability results in self-healing/lubricating. Feng et al., **[55]** synthesized NiAl-NbC-Ag composites via vacuum-hot-pressing sintering with direct addition of $AgNbO_3$ powders onto NiAl intermetallic alloy to form a composite that exhibited lower friction coefficient compared to NiAl. Additionally, the lubricating glaze layer consisting of $Ag_2Nb_4O_{11}$, $AgNbO_3$ and $AgNb_3O_8$ was formed by tribo-chemical reaction on the worn surfaces when the test temperatures got to 600 °C and 800 °C. Han et al., **[56]** synthesized NiAl/muscovite composites via spark plasma sintering of Ni, Al, $B_2O_3$ and $KAl_2(AlSi_3O_{10})(OH)_2$ (muscovite) with the muscovite well dispersed in the self-lubricating composite microstructure resulting in improved wear properties peaking at 9 wt% muscovite content. Zhu et al., **[57]** synthesized NiAl, NiAl-Cr-Mo and ZnO/Cuo reinforced

UNIVERSITY of the WESTERN CAPE

NiAl-Cr-Mo matrix composites via high temperature solid state reaction forming new phases (such as $NiZn_3$, $Cu_{0.81}Ni_{0.19}$ and $Al_2O_3$) during the fabrication process. The ZnO reinforced NiAl-Cr-Mo matrix composites exhibited low wear rate at 800 and 1000 °C in comparison with NiAl and NiAl-Cr-Mo while the CuO reinforced NiAl-Cr-Mo matrix composites exhibited self-lubricating performance at 800 °C, which was attributed to the presence of the glaze layer containing CuO and $MoO_3$. Liu et al., **[58]** ex-situ added hydrothermally synthesized silver vanadate ($Ag_3VO_4$) nanoparticles to pre-mechanically milled Ni and Al powder and further milled to fabricate NiAl-$Ag_3VO_4$ composite. The sintered composite consisted of Ag, and V oxide precipitates distributed homogeneously in the nanocrystalline NiAl matrix. An increase in $Ag_3VO_4$ content resulted in increase in density while microhardness decreased due to formation of high density soft metallic Ag. Excellent tribological properties were obtained at 900 °C due to the production of silver vanadate "lubricant". Shi eat al., **[59]** reinforced NiAl matrix with different solid lubricant additions (PbO, $Ti_3SiC_2$–$MoS_2$, $Ti_3SiC_2$–$WS_2$) to fabricate self-lubricating composites for use in high temperature friction and wear applications. Pin-on-disc dry sliding wear tests on the fabricated composite against $Si_3N_4$ balls showed:

i) Composites with $Ti_3SiC_2$–$MoS_2$ binary lubricant exhibited excellent self-lubricating and anti-wear properties over a wide temperature range,

ii) $MoS_2$ lubricated better at low temperatures, while $Ti_3SiC_2$ lubricated better at high temperatures, and,

iii) $Ti_3SiC_2$–$MoS_2$ binary lubricant presented the best synergetic lubricating effect of the three candidate compositions.

For the current study, NiAl intermetallic alloy reinforced with TiC particles was synthesized via cold pressing and sintering of the elemental Ni, Al, and TiC particles powders. This study has been submitted for scientific peer review.

UNIVERSITY of the WESTERN CAPE

## 2.3 STEEL METAL MATRIX COMPOSITES

Stainless steel is still the lifeblood for several industrial applications due to their multipurpose attributes, long life cycle and recyclability. Clare Broadbent **[60]** demonstrated the benefits of recycling steel to achieve a circular economy. It is therefore vital to widen the scope of this material into applications where it is not traditionally used. Careful incorporation of chosen reinforcements into steel matrices will open a myriad of further specialised applications for this material. TiC reinforced steels have attracted interest as engineering materials for a few attractive attributes derived from the composite material.

Tul et al., **[61]** explored TiC reinforced steels as engineering materials for inertial instruments and aerospace applications due to their excellent mechanical properties and machinability. Due to demands for dimensional stability in extreme operational environments for these components to avoid navigation errors, the study used thermal-cold cycling to improve the dimensional stability of TiC reinforced steel matrix composite. Xiao et al., **[62]** on the other hand investigated the microstructure, properties, and dimensional stability of a TiC-reinforced steel matrix composite during tempering to identify the underlying stabilizing mechanisms using commercial annealed TiC reinforced steel and concluded that the composite achieved optimal properties after 10 h (figure 2.8) of tempering.

Cho et al., **[63]** Fabricated TiC reinforced stainless steel composites via liquid pressing infiltration process and investigated their high-temperature compressive strengths and concluded that TiC reinforcement successfully suppressed softening of SUS431 matrix, resulting in about 5 times higher strength than that of SUS431 at 1050 °C.

UNIVERSITY of the WESTERN CAPE

Zhenming et al., **[64]** concluded via thermodynamics and metallographic evaluation that TiC is formed preferentially between austenite dendrites at the end of the solidification. This TiC then acts as heterogeneous nuclei for the crystallization of the $(Fe,Mn)_3C$ (cementite) and $\gamma_2$-Fe (austenite) intergrowth eutectic during in-situ synthesis of the composite via melting of the steel: (wt.%): 1.0 C, 8.0 Mn, 1.0 Si, 0.3 Ti, 0.032 P and 0.025S

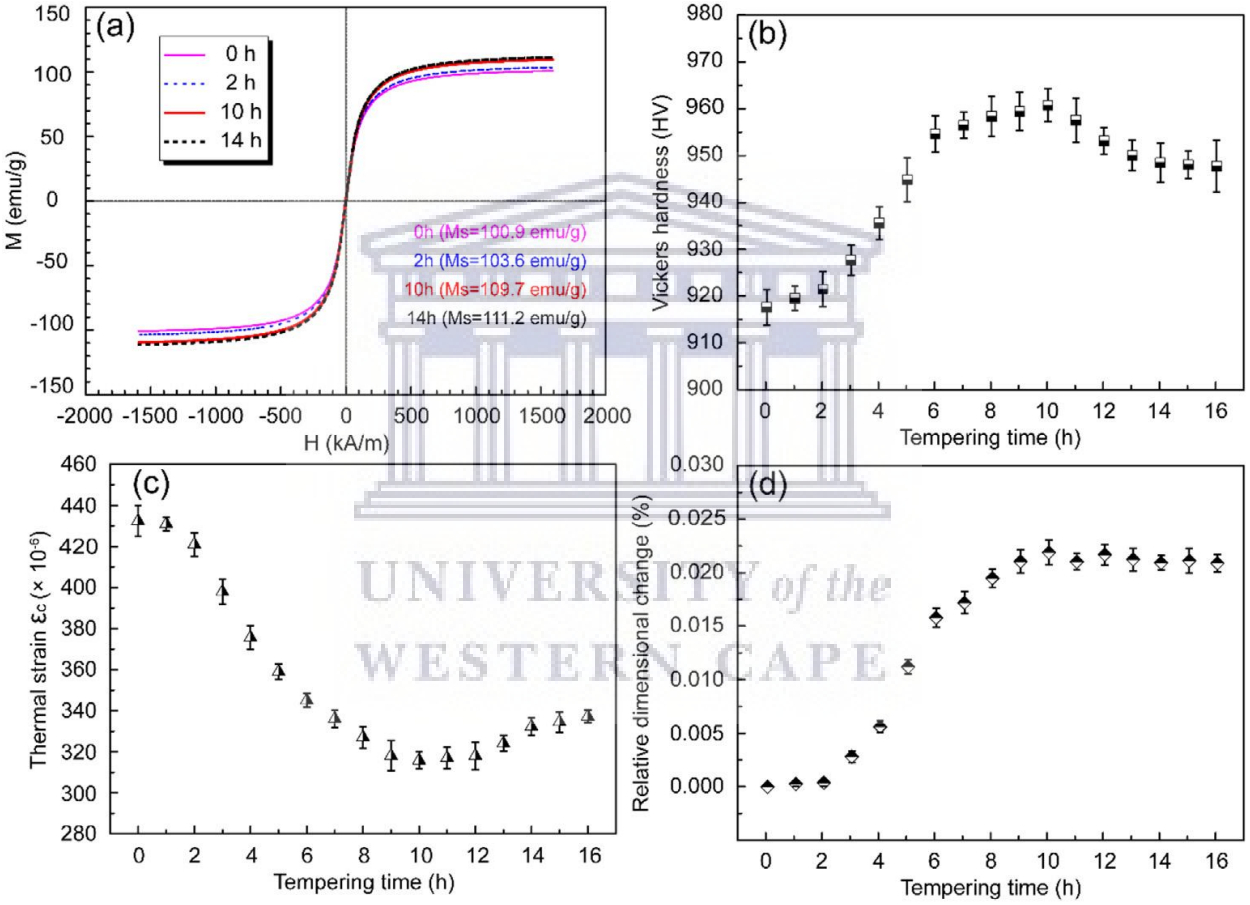


**Figure 2.8**: Properties of TiC-reinforced steel matrix composite tempered for various tempering times: (a) magnetic property, (b) hardness, (c) thermal strain, and (d) dimensional changes **[62]**.

Recent research work has used additive manufacturing to fabricate bulk reinforced steels as well as deposition of a reinforced surface layer on steel substrates. Chen et al., **[65]**

UNIVERSITY of the WESTERN CAPE

used course (> 50 µm) TiC to reinforce steel via laser cladding. The researchers could afford to use course particles due to high temperatures attained during fabrication, which melted and dissolved the course TiC to form fine TiC of various shapes. Li et al., **[66]** fabricated an ultrafine-grained Austenite matrix with uniformly distributed and nano-sized $VC_x$ particulate with an ultimate tensile strength of 1400 MPa via selective laser melting of pre milled submicron-sized $V_8C_7$ (3 wt%) ceramic and 316L (97 wt%) powders depicted in figure 2.9. Paraye et al., **[67]** modified the surface of AISI 4340 steel via in-situ incorporation of vanadium carbide used Tungsten Inert Gas (TIG) fusion of finely ground vanadium and graphite powder on the steel substrate. Metallographic evaluation of the modified layer revealed a fusion zone free of micro cracks and porosity with micron (cuboidal and rod) as well as nano (cuboidal) size vanadium carbide particles within the martensite matrix resulting in significant increase in the hardness of the modified region as depicted in Figure 2.10.

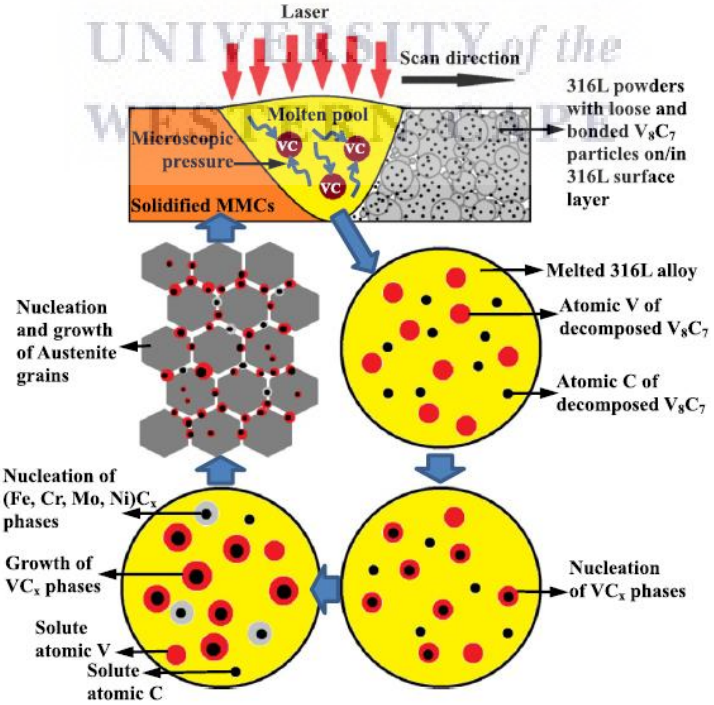


**Figure 2.9**: Schematic of formation mechanism for the SLM printed 316L based MMCs microstructure characteristics **[66]**.

http://etd.uwc.ac.za/

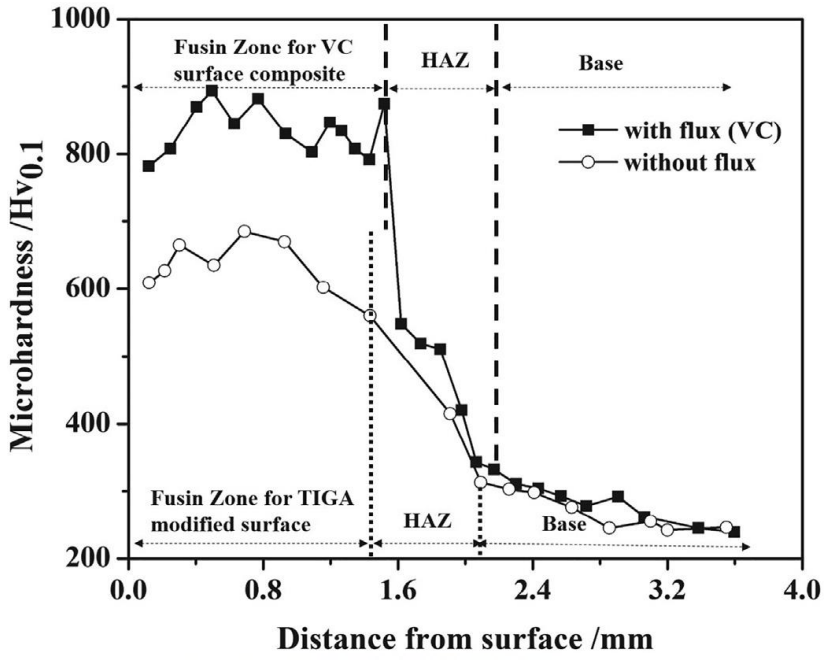


**Figure 2.10**: Microhardness distribution of the surface modified with and without flux across the various region **[67]**.

Saeedi et al., **[68]** used pulsed Nd: YAG laser to inject NiCr and NiCr–TiC powders onto the AISI 420 Martensitic stainless steel substrate to form a metal matrix composite layer of NiCr–TiC reinforced steel with enhanced hardness. Zhang et al., **[69]** synthesized TiC reinforced H13 steel matrix composites via laser deposition processing of premixed H13 and TiC powders and subjected the resulting composites to heat treatment to investigate the effect of tempering on the microstructure and mechanical properties. Upon tempering at 650 °C the mainly martensite structure transformed into tempered martensite and fine carbides with improved wear resistance despite a drop in hardness and tensile strength compared to the untampered samples. Tempering/annealing of the unequilibrium microstructures resulting from fabrications associated with high cooling rates is a critical step in achieving the final microstructure in steels. Radajewski et al., **[70]** concluded that the solution annealing step is necessary after spark plasma sintering (SPS). In their study the investigators synthesized steel matrix composite reinforced with 10 vol% Mg- PSZ via

UNIVERSITY of the WESTERN CAPE

SPS. The α′-martensite formed upon the subsequent quench and partition (Q&P) treatment (figure 2.11) of the solution-annealed microstructure increases the matrix strength of the steel and enhances stress transfer to the Mg-PSZ particles during deformation. Without the solution-annealing step no α′-martensite is formed during quenching and the subsequent partitioning plays no role on the flow behaviour.

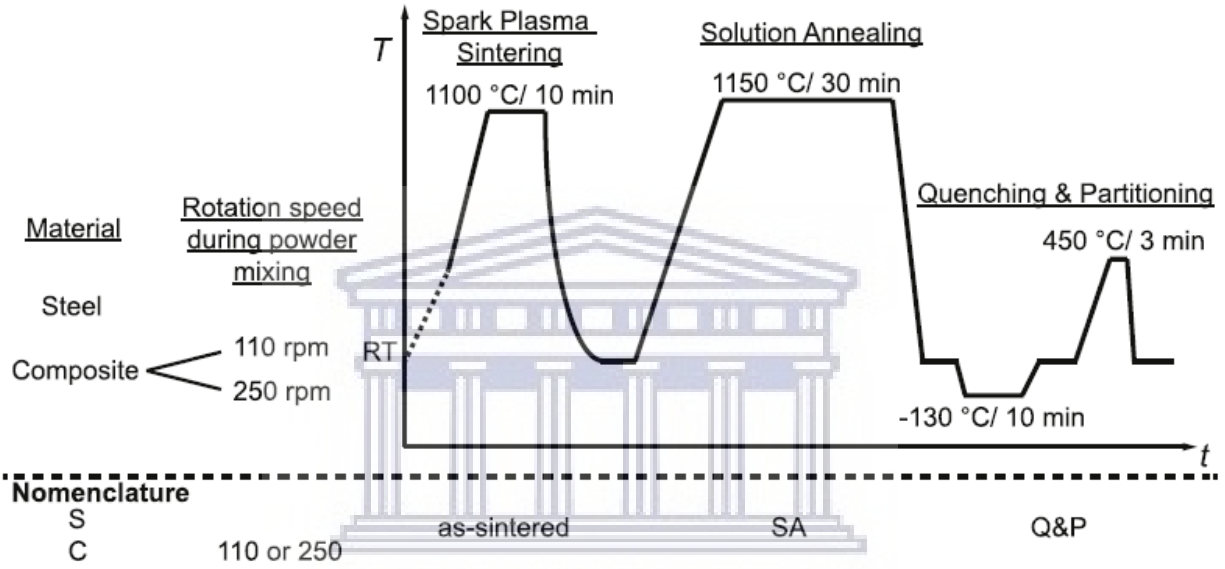


**Figure 2.11**: Schematic representation of the sample processing procedure **[70]**.

UNIVERSITY of the
WESTERN CAPE

Some fabrication routes yield superior properties than others as discovered by García et al., **[71]** who compared the tribological performance of tooling steel matrix composites reinforced with different amounts of vanadium carbide (VC) fabricated via metal injection moulding (MIM) and fabricated via conventional (mixing, compaction and sintering) PM technique. The higher carbide additions resulted in better wear while MIM samples performed better than those fabricated via conventional PM technique. Fudger et al., **[72]** fabricated steel encapsulated metal matrix composites via casting or infiltrating a molten MMC into a steel shell and measured over 100% increases in tension in the 304 steel

and nearly 100% increase in compression in the $Al_2O_3$ due to the high coefficient of expansion mismatch between 304 SS surrounding the Al-$Al_2O_3$.

Determining bulk properties of MMCs is often a challenge and Ma et al., **[73]** used Hadfield steel reinforced with niobium carbide as an example to propose a conceptual model to calculate the bulk hardness of particle-reinforced metal matrix composites. This is done by simulating an indentation process on a specimen of a homogenous material, whose stress-strain curve is exactly same as the one extracted from modelling a single direction tension/compression testing on a much smaller scale equivalent MMC rather than simulation on a specimen of the MMC directly. This is done to overcome the difficulty associated with implementing the numerical simulation directly on the MMC, as it requires a huge amount of calculation time as the MMC specimen used for indentation modelling may contain millions of particles.

For the current study, Steel/Ni-TiC composite produced by compaction and sintering had its microstructure and hardness investigated. The study was then published in a peer reviewed scientific journal:

UNIVERSITY of the
WESTERN CAPE

## 2.4 METAL OXYNITRIDES

Transition **[74–83]**, rare earth and alkaline **[76,81]** earth metal oxynitrides have found prominence as an important class of materials due to unique properties derived from combining the desirable attributes of both the oxides and the nitrides **[74]**. The increased covalence and more polarization of bonds with metals due to nitrogen's less electronegativity and more polarizability than oxygen affects the electronic properties resulting in new magnetic, conducting and dielectric materials **[75]**. Oxynitrides have found applications in improving wear and corrosion **[74,78,82]**, capacitance **[80–83]**, pigments **[84]**, phosphors, dielectrics, magnets **[75]** and arguable their most researched application, photocatalysis. Photocatalytic prowess of oxynitrides has been a subject of research in the field of energy and environmental applications such as production of Hydrogen via water splitting **[74–76,81]**, pollutant degradation, $CO_2$ conversion and antimicrobial disinfection **[76]**.

### 2.4.1 Metal Oxynitrides in Photocatalysis

Superior light harvesting ability (narrow band-gap energy) compared to metal oxides (> 3 eV) and moderate photostability has transition metal oxynitride perovskites [$AB(O,N)_3$] thrust into the research spotlight as an emerging class of inorganic materials **[74,81]**.

In their review, Manan et al., **[74]** provides a summary of the progress in visible-light induced water splitting via oxynitrides for generation of hydrogen as a clean and sustainable source of energy and gives an overview on the photocatalysts developed in the past several years, Table 2.6.

UNIVERSITY of the WESTERN CAPE

**Table 2.6**: Overview of visible light photocatalysts developed over the past several years **[74]**.

| Photocatalysts | |
|---|---|
| **Titanium oxide and titanate oxide** | **Metal oxynitrides** |
| $TiO_2$–Cr–Sb | TaON |
| $TiO_2$–N | $Ti_3O_3N_2$ |
| $SrTiO_3$–Cr–Ta | $Zr_3O_3N_2$ |
| $SrTiO_3$–Cr–Sb | **Metal sulfides** |
| $La_2Ti_2O_7$–Cr | CdS |
| $La_2Ti_2O_7$–Fe | CdS–CdO–ZnO |
| **Other transition metal oxides** | CdS–Zn |
| $BiVO_4$ | ZnS–Cu |
| $Ag_3VO_4$ | ZnS–Ni |
| $SnNb_2O_6$ | ZnS–Pb |
| $Nb_2O_5$ | $(AgIn)_xZn_{2(1-x)}S_2$ |
| $Ta_2O_5$ | $Sm_2Ti_2S_2O_5$ |
| $BiTaO_4$ | $(CuIn)_xZn_{2(1-x)}S_2$ |
| ZnO | $(CuAg\ In)_xZn_{2(1-x)}S_2$ |
| $Bi_2O_3$ | $Na_{14}In_{17}Cu_3S_{35}$ |
| $WO_3$ | **Metal perovskite oxynitride** |
| $Ga_2O_3$ | $LaTaON_2$ |
| **Mixed metal oxynitrides** | $LaMg_xTa_{1-x}O_{1+3x}N_{2-3x}$ |
| $(Ga_{1-x}Zn_x)(N_{1-x}O_x)$ | $CaTaO_2N$ |
| $(Zn_{1+x}Ge)(N_2O_x)$ | $SrTaO_2N$ |
| **Metal nitride** | $BaTaO_2N$ |
| $Ta_3N_5$ | $Sr_2Nb_2O_{7-x}N_x$ |
| **Metal free nitride** | $LaTiO_2N$ |
| $C_3N_4$ | $CaNbO_2N$ |
| | $SrNbO_2N$ |
| | $BaNbO_2N$ |
| | $Y_2Ta_2O_5N_2$ |

UNIVERSITY of the WESTERN CAPE

In their study Sakar et al., **[24]** gave a more rounded overview touching on types, applications, and synthesis of photocatalytic oxynitrides, figure 2.12.

Fuertes **[75]** explored oxynitrides of transition metals, alkaline earth metals and rare earth metals showing a variety of optical, magneto/electric (dielectric, thermoelectric, ferromagnetic, spin glass or magnetoresistance) and photocatalytic (in water splitting and organic reactions) properties. The study acknowledges that the most active area of

http://etd.uwc.ac.za/

research for oxynitride materials has been in photocatalytic applications, however results in various other important fields (such as batteries **[85,86]**) are emerging.

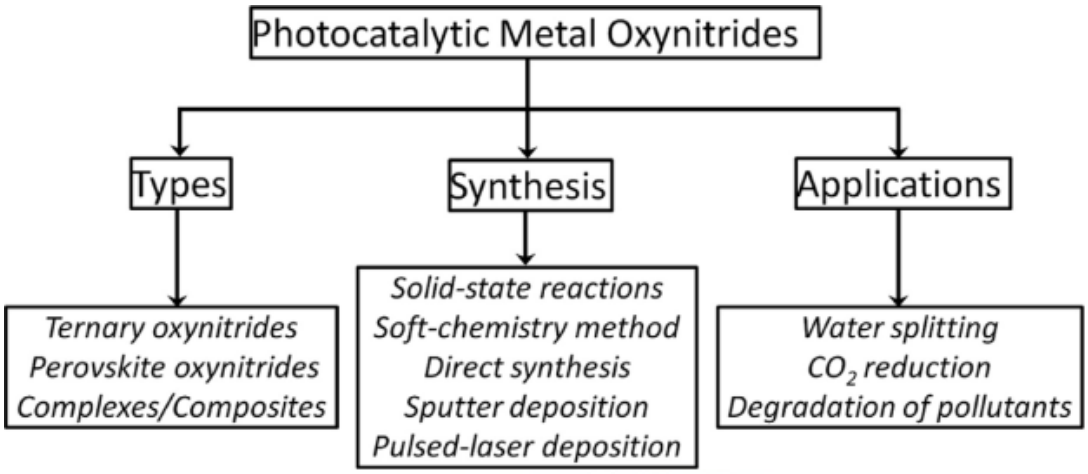


**Figure 2.12**: Types, synthesis and applications of photocatalytic metal oxynitrides **[76]**.

### 2.4.2 Synthesis of Metal Oxynitrides

Metal oxynitrides are generally prepared by exposing corresponding metal oxides with a nitriding agent at elevated temperatures. The important parameters determining the kinetics of the nitriding process are flow rate (of the nitriding agent), temperature, test piece placement (in the reaction chamber), and time.

In their recent review, Mirabbos et al., **[81]** interrogate recent advances on enhancing the photocatalytic activity of selected transition metaloxynitride perovskites and related works, challenges and future perspectives of these materials. They concluded that changing the synthesis approach, reducing the defect density that acts as a recombination centre for photo-generated charge carriers, increasing the conductivity, and engineering their band structures, namely the conduction and valence band positions substantially improves photocatalytic activity of transition metal oxynitride perovskites.

http://etd.uwc.ac.za/

Thermal ammonolysis **[74–77]**

This involves the use of gaseous $NH_3$ as a nitriding agent on a corresponding oxide at elevated temperatures according to the equation:

*Oxide + $NH_3$ (g) = Oxynitride + $H_2O$ (v)*

At temperatures above 500 °C $NH_3$ dissociates into $N_2$ and $H_2$. Low temperature processing results in difficulty with achieving homogeneous N stoichiometry and inferior sintering densification. If a reducing environment is desired, a gas mixture of $N_2/H_2$ (90/10 or 95/5 v/v) is used at high temperatures (1300 – 1600 °C) on a stoichiometric mixture of metal oxides, carbonates and/or nitrides under a high-pressure nitrogen. This solid-state reaction requires high activation energy due to the high triple bond energy between the N atoms, which requires the use of high temperatures, high flow rate of the nitriding (gas) agent and/or longer times. Oró-Solé et al., **[87]** synthesized a new $EuTi_{0.5}O_{3-x}N_x$ perovskites with tuned N/O ($0.87<N<1.63$) ratios by carefully controlling the treatment temperature and ammonia flow rate during the ammonolysis of scheelite $EuW_{0.5}O_4$. The study concludes that increasing nitrogen content results in changes on the structural and magneto-electric properties such as contraction of the unit cell volume and a reduction of symmetry from cubic to orthorhombic.

UNIVERSITY of the
WESTERN CAPE

I. Soft Chemistry **[74,76]**

As stated above, the reaction kinetics for nitriding can be sluggish due to the stability of the $N_2$ triple bond. Co-precipitation, sol-gel, Pechini method, templating and ultrafast evaporation-induced self-assembly or a combination of these is used to synthesize the precursor (oxide) instead of the traditional calcination. This resulting precursor exhibits improved sensitivity and reactivity and consequently

the reaction time, temperature and amount of nitriding gas can be reduced during the subsequent nitriding step.

II. Direct Synthesis **[74,76,77,88]**

During direct synthesis, an N-rich agent such as urea, amides, imides, and azides are used as sources of nitrogen. Formation of carbon residues, impurities and secondary phases has been reported as a drawback when using excess N sources such as urea. Gomathi et al., **[77]** synthesized ternary metal oxynitrides of the formulae $MTaO_2N$ (M = Ca, Sr or Ba), $MNbO_2N$ (M = Sr or Ba), $LaTiO_2N$ and $SrMoO_{3-x}N_x$. Urea was used as the nitriding agent by heating the corresponding metal carbonates and transition metal oxides with excess urea. The investigators claim this route yields metal oxynitrides that are generally stoichiometric and in the form of nanoparticles.

III. Sputter Deposition **[74,76]**

Thin films of perovskite oxynitrides have been successfully deposited on substrate surfaces via reactive radio frequency magnetron sputtering for photocatalytic applications. Unfortunately, this process has been reported to suffer from off stoichiometry thin films.

IV. Pulsed-Laser Deposition **[74,76]**

Similarly, to sputter deposition, pulsed-laser deposition is used to achieve thin films of oxynitrides on a substrate. A lattice mismatch between the deposited surface layer and the substrate is the major drawback since this process is based on the epitaxial growth of material onto a substrate.

UNIVERSITY of the WESTERN CAPE

Various recent endeavours to fabricate suitable metal oxynitride materials have used (a variation of) one or more of these fabrication routes. Dutta et al., **[89]** recently synthesized (figure 2.13) a cobalt nitride-vanadium oxynitride nanohybrid on carbon cloth (CVN/CC) with significantly enhanced water splitting activity via a facile synthetic method which surpasses the integrated state-of-the-art Pt-C and $RuO_2$ electrocatalysts in terms of both efficiency and durability.

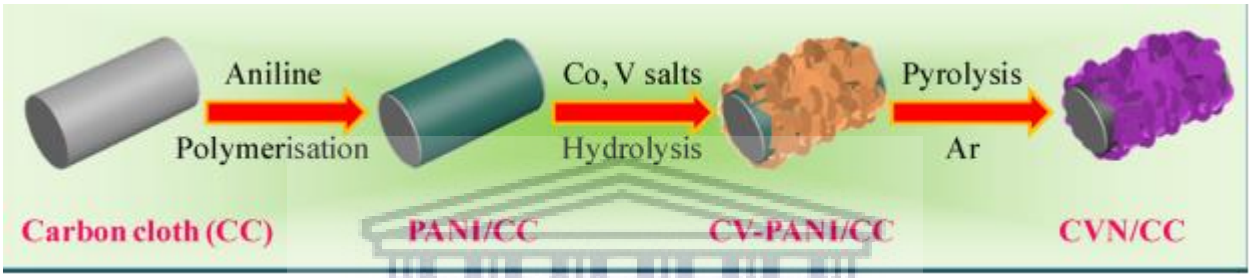


**Figure 2.13**: Schematic representation for the synthesis of CVN/CC

Wang et al., **[78]** synthesized a zirconium oxynitride ($Zr_2N_2O$) coating on 304 stainless steel by incorporating a controlled amount of oxygen into ZrN with plasma enhanced atomic layer deposition. The resulting oxynitride (figure 2.14) exhibited corrosion current density one order of magnitude lower than that of the ZrN coated substrate (figure 2.15a).

UNIVERSITY of the
WESTERN CAPE


**Figure 2.14**: Schematic representation for deposition process of $ZrN_xO_y$ coating on 304 SS **[78]**.

Hirpara et al., **[82]** used reactive magnetron sputtering method with optimized $O_2/N_2$ ratio to synthesize tantalum oxynitride thin film on the same (stainless steel 304 grade)

substrate. The coated material exhibited three times higher corrosion resistance in diluted hydrochloric acid than non-coated substrate (figure 2.15b).

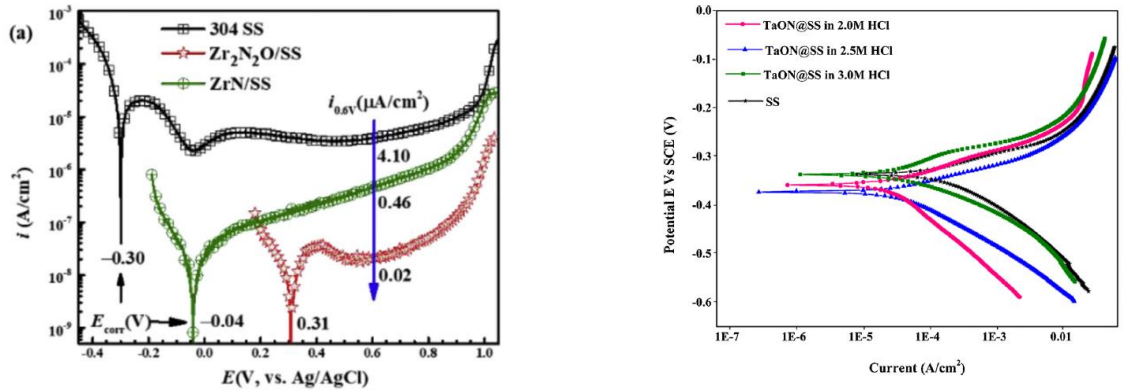


**Figure 2.15**: a) Potentiodynamic polarization curves for 304 SS, Zr2N2O/SS, ZrN/SS **[78]** as well as, b) Polarization test for tantalum oxynitride film-coated and bare SS 304 samples in 2.0 M, 2.5M and 3.0M HCl electrolyte at room temperature **[82]**.

Direct current magnetron sputtering was used by Venkataraj et al., **[90]** to grow thin films of several transition metal (Ti, Zr, Hf, Nb and Ta) oxynitrides at room temperature. They observed that the resulting film properties had a strong dependence on the deposition conditions. In their investigation, Venkataraj did not only develop a simulation package that reproduced the variation of the deposition rate, target voltage and film stoichiometry with reactive gas flow but also explained both the film formation mechanism as well as the significant improvement in film properties based on their results.

Belosludtsev **[91]** showed the possibility of fabricating low surface roughness thin aluminium antireflective oxynitride films using magnetron sputtering.

Recently Wu et al., **[80]** devised a strategy for the deposition of CoON layer on the flexible conductive substrate to prepare a flexible asymmetric super (FAS) electrode (CoON-CC) by electrodeposition and calcination (figure 2.16). The resulting FAS delivers a high aeral

UNIVERSITY of the WESTERN CAPE

capacitor of 2.12 F $cm^{-2}$(651.5 F $g^{-1}$) and energy density of 1.17 Wh $cm^{-2}$ as well as excellent flexibility and cycle performance, outperforming previously reported Co-based asymmetric supercapacitor.

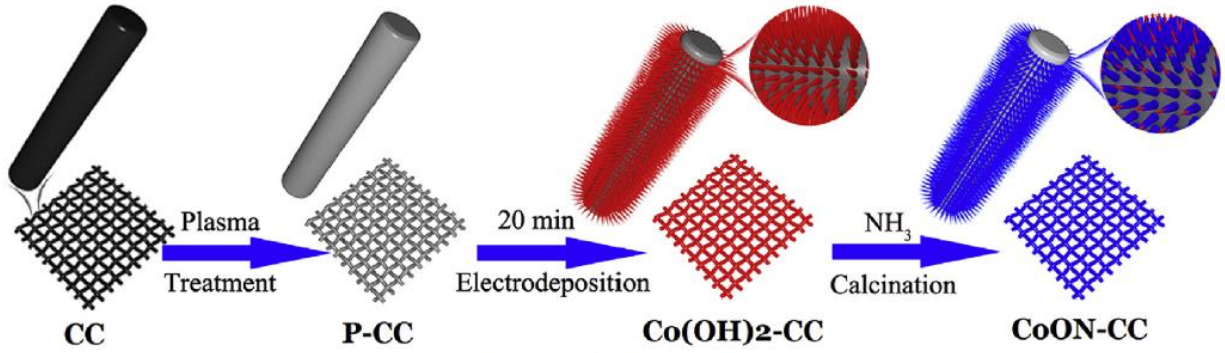


**Figure 2.16**: Schematic presentation for the fabrication of CoON-CC electrode **[80]**.

Earlier, Wang et al., **[83]** designed and synthesized molybdenum tungsten oxynitride with a porous architecture enlarged specific surface area with complete hydrophilicity as well as optimized electrical conductivity, which synergistically strengthen its supercapacity properties via nitriding its bimetallic oxide counterpart under ammonia atmosphere (figure 2.17).

UNIVERSITY of the
WESTERN CAPE

Yang et al., **[92]** used $C_3N_4$ as a nitriding agent in what would be direct synthesis to synthesize $SrNbO_2N$ and $CaTaO_2N$ from their oxide precursors at low formation temperature. The investigator, however, point out the formation of metal cyanamide intermediate as being crucial in achieving the low temperature synthesis of the nearly pure single phase oxynitride perovskites. Although this would be suitably classified as direct (nitrogen rich $C_3N_4$ as a nitriding agent) synthesis it also incorporates soft chemistry (metal cyanamide as crucial intermediate to reduce activation energy) synthesis. Li et al., **[93]**, used a combination of direct synthesis with urea as a nitriding agent along with

pressure-less spark plasma sintering to synthesize $ATaO_2N$ (A = Sr, Ba) within 10 minutes with oxynitride phase of 96.9% and 97.8% for $SrTaO_2N$ and $BaTaO_2N$ respectively.

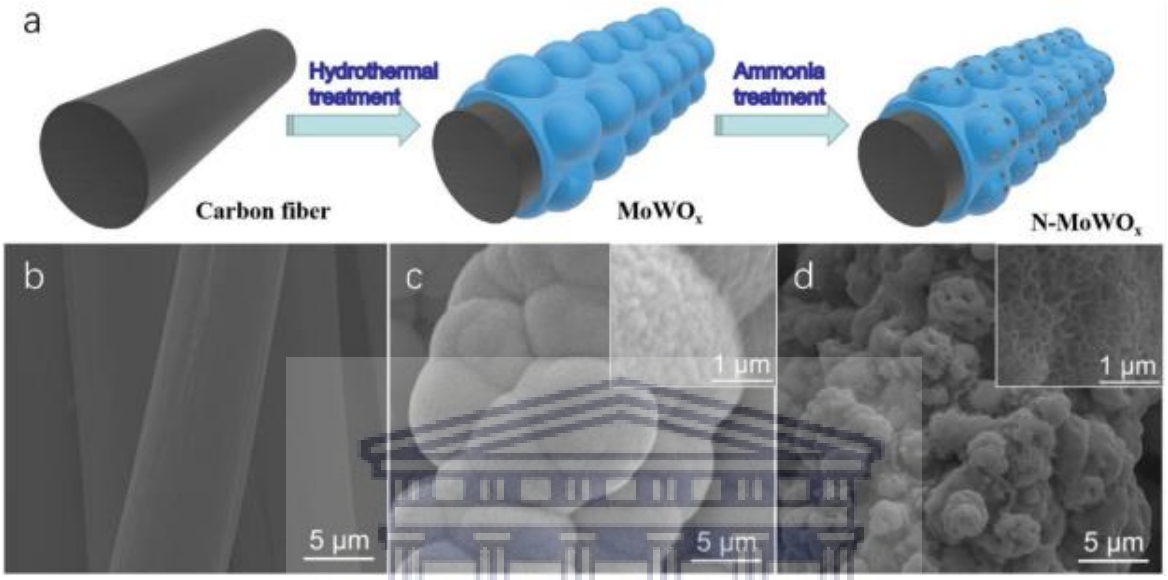


**Figure 2.17**: a) Schematic representation for the synthesis of N-$MoWO_x$ on carbon substrate as well as SEM images of the b) carbon fiber, c) $MoWO_x$ and (d) N-MoWOx **[83]**.

UNIVERSITY of the
WESTERN CAPE

As acknowledged by Fuertes **[75]** that despite the most active area of research for oxynitride materials being in photocatalytic applications, various other important fields such as batteries are emerging. Pozo-Gonzalo et al., **[94]** used ammonolysis of a suitable precursor to fabricate nanoporous molybdenum oxynitride and studied its suitability as an oxygen reduction catalyst in a 0.1M KCl aqueous solution for metal air batteries of fuel cells. In their study the investigators compared the molybdenum oxynitride to that of vanadium and tungsten oxynitrides and asserted that vanadium and molybdenum oxynitrides present superior performance in the series which they attributed to both (Mo and V oxynitrides) attaining an optimal composition of catalyst/binder/carbon and a small

http://etd.uwc.ac.za/

percentage of oxygen in the oxynitride composition. More recently, Ko et al., **[95]** used RF sputtering to directly deposit the most applied material (Lithium phosphorus oxynitride (LiPON)) in the thin film battery industry. A 200 nm layer on Li foil provided the best stability and performance of the Li anode in the cycling evaluation of Li│Li symmetric cells and $LiCoO_2$│Li cells.

An oxynitride with reduced particle size exhibits improved photocatalytic performance through increasing the active surface area, which allows the generation of more electron-hole pairs that contribute to the water reduction and oxidation reactions. Most research has thus been designed to synthesize oxynitrides with increased surface area as can be seen from several studies highlighted in this review referring to nanoscale products. Haydous et al., **[96]** achieved an eightfold increase in the BET surface of $BaTaO_xN_y$ perovskite particles using laser fragmentation method in liquid flow to increase the specific surface area up to a maximum BET area of 32.43 $m^2g^{-1}$. Wang et al., **[97]** hydrothermally fabricated $Zn_2GeO_4$ precursor nanorods with a smooth surface followed by nitriding of the precursor at 800 °C for 6 h to synthesize $(Zn_{1+x}Ge)(N_2O_x)$ nanotubes (Figure 2.18) with rough surface area without a template for formation of a tube structure. The researchers attribute the transformation of the nanorods onto nanotubes despite no template for formation of a tube structure to ordered morphological transformation from $Zn_2GeO_4$ nanorod during nitriding. The resulting $(Zn_{1+x}Ge)(N_2O_x)$, exhibited enhanced photocatalytic $NO_x$ decomposition activity under both ultraviolet and visible light irradiation compared to the one synthesized via conventional solid-state reaction.

UNIVERSITY of the WESTERN CAPE


**Figure 2.18**: Schematic representation for the two-steps preparation process of $(Zn_{1+x}Ge)(N_2O_x)$ nanotubes **[97]**.

To tailor the optical, electronic, and structural properties of the oxynitrides, continuous control of anion composition is desirable during synthesis. Harayama et al., **[79]** developed a compact ΔE-E telescope elastic recoil detection analysis (ERDA) system (figure 2.19) designed to identify the recoils of O and N from metal oxynitrides thin films irradiated with 40 MeV $^{35}Cl^{7+}$. The investigators also confirmed availability of the gas ionization chamber for identifying the recoils of lithium, carbon, and fluorine over and above those of O and N.

UNIVERSITY of the
WESTERN CAPE

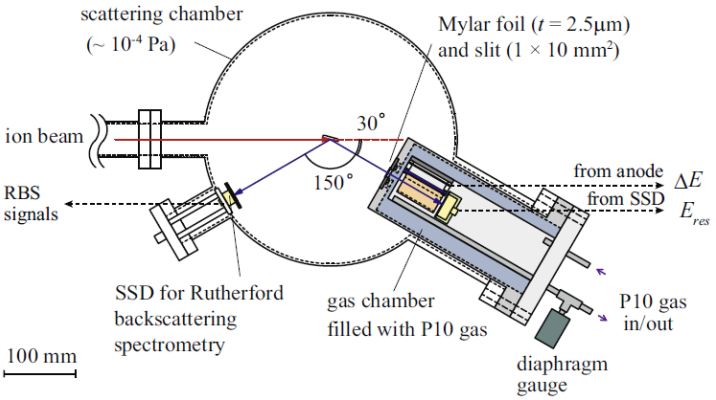


**Figure 2.19**: Schematic of scattering chamber setup equipped with the DE-E telescope ERDA and the RBS detectors **[79]**.

http://etd.uwc.ac.za/

As stated previously, titanium as a transition metal has its oxynitride as one class of materials that has been studied for various applications. Due to their enhance stability in air and moisture as well as smaller band gaps compare to pure oxides, nitrogen doping in $TiO_2$ tunes the band gap from ultraviolet to visible range which leads to electronic and/or optical properties **[74]**.

For the current study, $TiO_{2-x}N_x$ synthesized via annealing of commercial purity titanium powder in air was characterized. The study was then published in a peer reviewed journal. The Titanium oxynitrides were then used as reinforcement material for the selected matrices, e.g. - A356Al alloy, Sn, Ni and Ti powders were blended with Titanium oxynitride followed by cold pressing and sintering. The resulting composite structure was characterised. This study has been submitted for scientific peer review.

UNIVERSITY of the
WESTERN CAPE

http://etd.uwc.ac.za/

## 2.5 References


2.1 D. Miracle, Metal matrix composites – From science to technological significance, Compos. Sci. Technol. 65 (2005) 2526–2540. https://doi.org/10.1016/j.compscitech.2005.05.027.

2.2 Advances in laser processing of Metal Matrix Composites (MMCS), in: Gisario, Annamaria; Veniali, F, Rome, 2010. https://doi.org/10.2351/1.5062072.

2.3 J. Hemanth, Development and property evaluation of aluminum alloy reinforced with nano-ZrO2 metal matrix composites (NMMCs), Mater. Sci. Eng. A. 507 (2009) 110–113. https://doi.org/10.1016/j.msea.2008.11.039.

2.4 Y. Yang, J. Lan, X. Li, Study on bulk aluminum matrix nano-composite fabricated by ultrasonic dispersion of nano-sized SiC particles in molten aluminum alloy, Mater. Sci. Eng. A. 380 (2004) 378–383. https://doi.org/10.1016/j.msea.2004.03.073.

2.5 Z. Zhang, D.L. Chen, Contribution of Orowan strengthening effect in particulate-reinforced metal matrix nanocomposites, Mater. Sci. Eng. A. 483–484 (2008) 148–152. https://doi.org/10.1016/j.msea.2006.10.184.

2.6 C. Borgonovo, D. Apelian, Manufacture of Aluminum Nanocomposites: A Critical Review, Mater. Sci. Forum. 678 (2011) 1–22. https://doi.org/10.4028/www.scientific.net/MSF.678.1.

2.7 G. Govender, The Light Metals Development Network Yearly Report for the Period 1 April 2019 – 31 March 2020 to the Department of Science and Innovation of South Africa – Focus Area: Light Metals (Aluminium), Pretoria, 2020.

2.8 R. Troncy, G. Bonnet, F. Pedraza, Microstructural characterization of NiAl–Al2O3 composite materials obtained by in situ aluminothermic reduction of NiO for potential coating applications, Mater. Chem. Phys. (2020) 123124.


UNIVERSITY of the WESTERN CAPE

https://doi.org/10.1016/j.matchemphys.2020.123124.

2.9 M. Krasnowski, S. Gierlotka, S. Ciołek, T. Kulik, Nanocrystalline NiAl intermetallic alloy with high hardness produced by mechanical alloying and hot-pressing consolidation, Adv. Powder Technol. 30 (2019) 1312–1318. https://doi.org/10.1016/j.apt.2019.04.006.

2.10 M. Krasnowski, S. Gierlotka, T. Kulik, NiAl-B composites with nanocrystalline intermetallic matrix produced by mechanical alloying and consolidation, Adv. Powder Technol. 30 (2019) 2742–2750. https://doi.org/10.1016/j.apt.2019.08.021.

2.11 H. Zhang, H. Zhu, J. Huang, J. Li, Z. Xie, In-situTiB2-NiAl composites synthesized by arc melting: Chemical reaction,microstructure and mechanical strength, Mater. Sci. Eng. A. 719 (2018) 140–146. https://doi.org/10.1016/j.msea.2018.01.125.

2.12 A. Albiter, M. Salazar, E. Bedolla, R.A.L. Drew, R. Perez, Improvement of the mechanical properties in a nanocrystalline NiAl intermetallic alloy with Fe, Ga and Mo additions, Mater. Sci. Eng. A. 347 (2003) 154–164. https://doi.org/10.1016/S0921-5093(02)00563-4.

2.13 Z. Sun, B. Liu, C. He, L. Xie, Q. Peng, Shift of creep mechanism in nanocrystalline NiAl alloy, Materials (Basel). 12 (2019). https://doi.org/10.3390/ma12162508.

2.14 K. Bochenek, M. Basista, Advances in processing of NiAl intermetallic alloys and composites for high temperature aerospace applications, Prog. Aerosp. Sci. 79 (2015) 136–146. https://doi.org/10.1016/j.paerosci.2015.09.003.

2.15 X. Fan, W. Huang, X. Zhou, B. Zou, Preparation and characterization of NiAl–TiC–TiB2 intermetallic matrix composite coatings by atmospheric plasma spraying of SHS powders, Ceram. Int. 46 (2020) 10512–10520. https://doi.org/10.1016/j.ceramint.2020.01.052.

2.16 M.B. Rahaei, In-Situ Manufacturing of NiAl-TiC Composites with Three Dimensional (3D) Discrete Particular Network and Bi-Continuous Microstructures,

UNIVERSITY of the WESTERN CAPE

Adv. Powder Technol. 30 (2019) 1025–1033. https://doi.org/10.1016/j.apt.2019.02.017.

2.17 T.W.B. Riyadi, T. Zhang, D. Marchant, X. Zhu, NiAl–TiC–Al2O3 composite formed by self-propagation high-temperature synthesis process: Combustion behaviour, microstructure, and properties, J. Alloys Compd. 805 (2019) 104–112. https://doi.org/10.1016/j.jallcom.2019.04.349.

2.18 O.O. Ayodele, A.O. Adegbenjo, M.A. Awotunde, M.B. Shongwe, P.A. Olubambi, The influence of heating rate on the microstructural evolutions and mechanical properties of spark plasma sintered multi-walled carbon nanotubes reinforced NiAl intermetallic matrix composites, Mater. Sci. Eng. A. 773 (2020) 138869. https://doi.org/10.1016/j.msea.2019.138869.

2.19 J.K. Sonber, T.S.R.C. Murthy, K. Sairam, A. Nagaraj, S. Majumdar, V. Kain, ZrB2 based novel composite with NiAl as reinforcement phase, Int. J. Refract. Met. Hard Mater. 70 (2018) 56–65. https://doi.org/10.1016/j.ijrmhm.2017.09.013.

2.20 Ş. Talaş, G Oruç, Characterization of TiC and TiB2 reinforced Nickel Aluminide (NiAl) based metal matrix composites cast by in situ vacuum suction arc melting, Vacuum. 172 (2020). https://doi.org/10.1016/j.vacuum.2019.109066.

2.21 F. Hadef, Synthesis and disordering of B2 TM-Al (TM = Fe, Ni, Co) intermetallic alloys by high energy ball milling: A review, Powder Technol. 311 (2017) 556–578. https://doi.org/10.1016/j.powtec.2017.01.082.

2.22 T. Chen, J.M. Hampikian, N.N. Thadhani, Synthesis and characterization of mechanically alloyed and shock-consolidated nanocrystalline NiAl intermetallic, Acta Mater. 47 (1999) 2567–2579. https://doi.org/10.1016/S1359-6454(99)00059-2.

2.23 E. Liu, J. Jia, Y. Bai, W. Wang, Y. Gao, Study on preparation and mechanical property of nanocrystalline NiAl intermetallic, Mater. Des. 53 (2014) 596–601.

UNIVERSITY of the WESTERN CAPE

http://etd.uwc.ac.za/

https://doi.org/10.1016/j.matdes.2013.07.052.

2.24 O.O. Ayodele, M.A. Awotunde, A.O. Adegbenjo, M.B. Shongwe, B.A. Obadele, P.A. Olubambi, Synthesis and heating rate effect on the mechanical properties of NiAl intermetallic compound, Mater. Today Proc. 28 (2020) 785–788. https://doi.org/10.1016/j.matpr.2019.12.298.

2.25 K.H. Biranvand, M. Vaezi, M. Razavi, Thermodynamic study on the formation of order-disorder structure of the NiAl intermetallic compound by semi-empirical model, Phys. B Condens. Matter. 561 (2019) 43–53. https://doi.org/10.1016/j.physb.2019.02.050.

2.26 M.V. J. SUBRAHMANYAM, Review Self-propagating high-temperature synthesis, J. Mater. Sci. 27 (1992) 6249–6273. https://link.springer.com/content/pdf/10.1007/BF00576271.pdf.

2.27 Y. Shu, A. Suzuki, N. Takata, M. Kobashi, Fabrication of porous NiAl intermetallic compounds with a hierarchical open-cell structure by combustion synthesis reaction and space holder method, J. Mater. Process. Technol. 264 (2019) 182–189. https://doi.org/10.1016/j.jmatprotec.2018.09.010.

2.28 H.L. Zhao, F. Qiu, S.B. Jin, Q.C. Jiang, High work-hardening effect of the pure NiAl intermetallic compound fabricated by the combustion synthesis and hot pressing technique, Mater. Lett. 65 (2011) 2604–2606. https://doi.org/10.1016/j.matlet.2011.05.091.

2.29 O. Ozdemir, S. Zeytin, C. Bindal, A study on NiAl produced by pressure-assisted combustion synthesis, Vacuum. 84 (2009) 430–437. https://doi.org/10.1016/j.vacuum.2009.09.006.

2.30 X. Fan, L. Zhu, W. Huang, Investigation of NiAl intermetallic compound as bond coat for thermal barrier coatings on Mg alloy, J. Alloys Compd. 729 (2017) 617–626. https://doi.org/10.1016/j.jallcom.2017.09.190.

UNIVERSITY of the WESTERN CAPE

http://etd.uwc.ac.za/

2.31 E.T. Kubaski, O.M. Cintho, J.L. Antoniassi, H. Kahn, J.D.T. Capocchi, Obtaining NiAl intermetallic compound using different milling devices, Adv. Powder Technol. 23 (2012) 667–672. https://doi.org/10.1016/j.apt.2011.08.005.

2.32 M.H. Enayati, F. Karimzadeh, S.Z. Anvari, Synthesis of nanocrystalline NiAl by mechanical alloying, J. Mater. Process. Technol. 200 (2008) 312–315. https://doi.org/10.1016/j.jmatprotec.2007.09.023.

2.33 A. Mashreghi, M.M. Moshksar, Partial martensitic transformation of nanocrystalline NiAl intermetallic during mechanical alloying, J. Alloys Compd. 482 (2009) 196–198. https://doi.org/10.1016/j.jallcom.2009.03.156.

2.34 E.T. Kubaski, O.M. Cintho, J.D.T. Capocchi, Effect of milling variables on the synthesis of NiAl intermetallic compound by mechanical alloying, Powder Technol. 214 (2011) 77–82. https://doi.org/10.1016/j.powtec.2011.07.038.

2.35 Y. Sun, P. Lin, S.J. Yuan, A novel method for fabricating NiAl alloy sheet components using laminated Ni/Al foils, Mater. Sci. Eng. A. 754 (2019) 428–436. https://doi.org/10.1016/j.msea.2019.03.069.

2.36 Y. Sun, P. Lin, S.J. Yuan, A novel process for integrated forming and reaction synthesis of NiAl alloy curved shells, J. Mater. Process. Technol. 285 (2020) 116798. https://doi.org/10.1016/j.jmatprotec.2020.116798.

2.37 T. Volpp, E. Göring, W.M. Kuschke, E. Arzt, Grain size determination and limits to Hall-Petch behavior in nanocrystalline NiAl powders, Nanostructured Mater. 8 (1997) 855–865. https://doi.org/10.1016/S0965-9773(98)00019-1.

2.38 A.A. Zaitsev, Z.A. Sentyurina, E.A. Levashov, Y.S. Pogozhev, V.N. Sanin, P.A. Loginov, M.I. Petrzhik, Structure and properties of NiAl-Cr(Co,Hf) alloys prepared by centrifugal SHS casting. Part 1 – Room temperature investigations, Mater. Sci. Eng. A. 690 (2017) 463–472. https://doi.org/10.1016/j.msea.2016.09.075.

2.39 S. García-Galán, G. Arámburo-Pérez, C. González-Rivera, J. Juárez-Islas, The

UNIVERSITY of the WESTERN CAPE

effect of Cu-macroalloying on β-NiAl intermetallic compound obtained by mechanical alloying, J. Mater. Process. Technol. 143–144 (2003) 551–554. https://doi.org/10.1016/S0924-0136(03)00353-4.

2.40 K. Bochenek, W. Węglewski, J. Morgiel, M. Basista, Influence of rhenium addition on microstructure, mechanical properties and oxidation resistance of NiAl obtained by powder metallurgy, Mater. Sci. Eng. A. 735 (2018) 121–130. https://doi.org/10.1016/j.msea.2018.08.032.

2.41 Z.P. Xing, L.G. Yu, J.T. Guo, J.Y. Dai, G.Y. An, Z.Q. Hu, Microstructure and compression properties of NiAl-matrix in situ composites reinforced by TiC particulate, J. Mater. Sci. Lett. 14 (1995) 443–445. https://doi.org/10.1007/BF00274567.

2.42 Z. Zhang, L. Li, J.C. Yang, γ-Al2O3 thin film formation via oxidation of β-NiAl(1 1 0), Acta Mater. 59 (2011) 5905–5916. https://doi.org/10.1016/j.actamat.2011.05.064.

2.43 M. Beyhaghi, J. Vahdati Khaki, M. Manawan, A. Kiani-Rashid, M. Kashefi, S. Jonsson, In-situ synthesis and characterization of nano-structured NiAl-Al2O3 composite during high energy ball milling, Powder Technol. 329 (2018) 95–106. https://doi.org/10.1016/j.powtec.2018.01.052.

2.44 H. Zhang, H. Zhu, J. Huang, J. Li, Z. Xie, In-situ TiB2-NiAl composites synthesized by arc melting: Chemical reaction, microstructure and mechanical strength, Mater. Sci. Eng. A. 719 (2018) 140–146. https://doi.org/10.1016/j.msea.2018.01.125.

2.45 J. Shen, B. Zou, X. Cai, S. Dong, X. Cao, Fabrication and properties of TiB2-TiC reinforced NiAl coatings by reactive plasma spraying on AZ91D magnesium alloy, Surf. Coatings Technol. 378 (2019) 125055. https://doi.org/10.1016/j.surfcoat.2019.125055.

2.46 H.Z. Cui, L. Ma, L.L. Cao, F.L. Teng, N. Cui, Effect of NiAl content on phases and

UNIVERSITY of the WESTERN CAPE

microstructures of TiC-TiB 2-NiAl composites fabricated by reaction synthesis, Trans. Nonferrous Met. Soc. China (English Ed. 24 (2014) 346–353. https://doi.org/10.1016/S1003-6326(14)63067-3.

2.47 X. jie SONG, H. zhi CUI, L. li CAO, P.Y. GULYAEV, Microstructure and evolution of (TiB2+Al2O3)/NiAl composites prepared by self-propagation high-temperature synthesis, Trans. Nonferrous Met. Soc. China (English Ed. 26 (2016) 1878–1884. https://doi.org/10.1016/S1003-6326(16)64265-6.

2.48 A.A. Shokati, N. Parvin, M. Shokati, Combustion synthesis of NiAl matrix composite powder reinforced by TiB 2 and TiN particulates from Ni-Al-Ti-BN reaction system, J. Alloys Compd. 585 (2014) 637–643. https://doi.org/10.1016/j.jallcom.2013.09.020.

2.49 M. Awotunde, A. Adegbenjo, O. Ayodele, M. Okoro, M. Shongwe, P. Olubambi, Influence of carbon nanotubes addition on the mechanical properties of nickel aluminide – NiAl, Mater. Today Proc. (2020) 8–12. https://doi.org/10.1016/j.matpr.2019.12.231.

2.50 O.O. Ayodele, A.O. Adegbenjo, M.A. Awotunde, S.O. Akinwamide, M.B. Shongwe, P.A. Olubambi, Planetary ball milling of MWCNTs reinforced NiAl composites, Mater. Today Proc. (2020). https://doi.org/10.1016/j.matpr.2019.12.291.

2.51 B. Li, Y. Gao, X. Hou, C. Li, H. Guo, Y. Kang, Y. Li, Q. Zheng, S. Zhao, Microstructure, mechanical and tribological properties of NiAl matrix composites with addition of BaO/TiO2 binary oxides, Tribol. Int. 144 (2020). https://doi.org/10.1016/j.triboint.2019.106108.

2.52 H. Zhao, F. Qiu, S. Jin, Q. Jiang, High room-temperature plastic and work-hardening effect of the NiAl-matrix composites reinforced by particulates, Intermetallics. 19 (2011) 376–381. https://doi.org/10.1016/j.intermet.2010.10.023.

2.53 H.L. Zhao, F. Qiu, S.B. Jin, Q.C. Jiang, Effect of different strain rates on

UNIVERSITY of the WESTERN CAPE

compression property and work-hardening behavior for the NiAl-matrix composite with 1.7wt.% NbB 2 and Nb xC, Mater. Sci. Eng. A. 534 (2012) 22–25. https://doi.org/10.1016/j.msea.2011.10.113.

2.54 H.L. Zhao, F. Qiu, S.B. Jin, Q.C. Jiang, Compression properties and work-hardening effect of the NiAl-matrix composite with TaB 2 and TaB, Intermetallics. 27 (2012) 1–5. https://doi.org/10.1016/j.intermet.2012.01.016.

2.55 X. Feng, C. Lu, J. Jia, J. Xue, Q. Wang, Y. Sun, W. Wang, G. Yi, High temperature tribological behaviors and wear mechanisms of NiAl–NbC–Ag composites formed by in-situ decomposition of AgNbO3, Tribol. Int. 141 (2020) 105898. https://doi.org/10.1016/j.triboint.2019.105898.

2.56 Y. Han, K. Yang, P. Jing, B. Xue, W. Ma, Mechanical and tribological properties of NiAl/muscovite composites, J. Alloys Compd. 741 (2018) 765–774. https://doi.org/10.1016/j.jallcom.2018.01.169.

2.57 S. Zhu, Q. Bi, M. Niu, J. Yang, W. Liu, Tribological behavior of NiAl matrix composites with addition of oxides at high temperatures, Wear. 274–275 (2012) 423–434. https://doi.org/10.1016/j.wear.2011.11.006.

2.58 E. Liu, Y. Bai, Y. Gao, G. Yi, J. Jia, Tribological properties of NiAl-based composites containing Ag 3VO4 nanoparticles at elevated temperatures, Tribol. Int. 80 (2014) 25–33. https://doi.org/10.1016/j.triboint.2014.06.014.

2.59 X. Shi, W. Zhai, M. Wang, Z. Xu, J. Yao, S. Song, Y. Wang, Tribological behaviors of NiAl based self-lubricating composites containing different solid lubricants at elevated temperatures, Wear. 310 (2014) 1–11. https://doi.org/10.1016/j.wear.2013.12.002.

2.60 C. Broadbent, Int J Life Cycle Assess, Int J Life Cycle Assess. 21 (d. g.) 1658–1665. https://doi.org/10.1007/s11367-016-1081-1.

2.61 X.X. Tu, L.R. Xiao, X.J. Zhao, Z.Y. Cai, Z.W. Peng, D.M. Wei, Effects of thermal-

UNIVERSITY of the WESTERN CAPE

cold cycling on the dimensional stability of TiC reinforced steel matrix composite, Mater. Lett. 279 (2020) 10–14. https://doi.org/10.1016/j.matlet.2020.128483.

2.62 L.R. Xiao, X.X. Tu, X.J. Zhao, Z.Y. Cai, Y.F. Song, Microstructural evolution and dimensional stability of TiC-reinforced steel matrix composite during tempering, Mater. Lett. 259 (2020) 8–12. https://doi.org/10.1016/j.matlet.2019.126871.

2.63 S. Cho, Y.H. Lee, S. Ko, H. Park, D. Lee, S. Shin, I. Jo, Y. Kim, S.B. Lee, S.K. Lee, Enhanced high-temperature compressive strength of TiC reinforced stainless steel matrix composites fabricated by liquid pressing infiltration process, J. Alloys Compd. 817 (2020) 152714. https://doi.org/10.1016/j.jallcom.2019.152714.

2.64 X. Zhenming, L. Gaofei, G. Qingfeng, J. Qichuan, TiC as heterogeneous nuclei of the (Fe, Mn)3C and austenite intergrowth eutectic in austenite steel matrix wear resistant composite, Mater. Res. Bull. 39 (2004) 457–463. https://doi.org/10.1016/j.materresbull.2003.10.014.

2.65 H. Chen, Y. Lu, Y. Sun, Y. Wei, X. Wang, D. Liu, Coarse TiC particles reinforced H13 steel matrix composites produced by laser cladding, Surf. Coatings Technol. 395 (2020) 125867. https://doi.org/10.1016/j.surfcoat.2020.125867.

2.66 B. Li, B. Qian, Y. Xu, Z. Liu, J. Zhang, F. Xuan, Additive manufacturing of ultrafine-grained austenitic stainless steel matrix composite via vanadium carbide reinforcement addition and selective laser melting: Formation mechanism and strengthening effect, Mater. Sci. Eng. A. 745 (2019) 495–508. https://doi.org/10.1016/j.msea.2019.01.008.

2.67 N.K. Paraye, P.K. Ghosh, S. Das, A novel approach to synthesize surface composite by in-situ grown VC reinforcement in steel matrix via TIG arcing, Surf. Coatings Technol. 399 (2020) 126129. https://doi.org/10.1016/j.surfcoat.2020.126129.

2.68 R. Saeedi, R. Shoja-Razavi, S.-R. Bakhshi, M. Erfanmanesh, A. Ahmadi-Bani,

UNIVERSITY of the WESTERN CAPE

Optimization and characterization of laser cladding of NiCr and NiCr–TiC composite coatings on AISI 420 stainless steel, Ceram. Int. (2020) 1–14. https://doi.org/10.1016/j.ceramint.2020.09.284.

2.69 M. Zhang, C. Li, Q. Gao, J. Fang, T.L. Wu, K.H. Wang, The effect of heat treatment on microstructure and properties of laser-deposited TiC reinforced H13 steel matrix composites, Optik (Stuttg). 206 (2020) 164286. https://doi.org/10.1016/j.ijleo.2020.164286.

2.70 M. Radajewski, S. Decker, M. Wendler, L. Krüger, Materials Science & Engineering A Influence of solution annealing on microstructure and mechanical properties of a quenched and partitioned steel matrix composite processed by SPS, Mater. Sci. Eng. A. 799 (2021) 140277. https://doi.org/10.1016/j.msea.2020.140277.

2.71 C. García, F. Martín, G. Herranz, C. Berges, A. Romero, Effect of adding carbides on dry sliding wear behaviour of steel matrix composites processed by metal injection moulding, Wear. 414–415 (2018) 182–193. https://doi.org/10.1016/j.wear.2018.08.010.

2.72 S. Fudger, D. Sediako, P. Karandikar, C. Ni, Residual stress induced mechanical property enhancement in steel encapsulated light metal matrix composites, Mater. Sci. Eng. A. 699 (2017) 10–17. https://doi.org/10.1016/j.msea.2017.05.073.

2.73 L. Ma, C. Huang, K. Dolman, X. Tang, J. Yang, Z. Shi, Z.S. Liu, A method to calculate the bulk hardness of metal matrix composite using Hadfield steel reinforced with niobium carbide particles as an example, Mech. Mater. 112 (2017) 154–162. https://doi.org/10.1016/j.mechmat.2017.06.005.

2.74 M. Ahmed, G. Xinxin, A review of metal oxynitrides for photocatalysis, Inorg. Chem. Front. 3 (2016) 578–590. https://doi.org/10.1039/C5QI00202H.

2.75 A. Fuertes, Metal oxynitrides as emerging materials with photocatalytic and electronic properties, Mater. Horizons. 2 (2015) 453–461.

UNIVERSITY of the WESTERN CAPE

http://etd.uwc.ac.za/

https://doi.org/10.1039/C5MH00046G.

2.76 M. Sakar, R.M. Prakash, K. Shinde, G.R. Balakrishna, Revisiting the materials and mechanism of metal oxynitrides for photocatalysis, Int. J. Hydrogen Energy. 45 (2020) 7691–7705. https://doi.org/10.1016/j.ijhydene.2019.04.222.

2.77 A. Gomathi, S. Reshma, C.N.R. Rao, A simple urea-based route to ternary metal oxynitride nanoparticles, J. Solid State Chem. 182 (2009) 72–76. https://doi.org/10.1016/j.jssc.2008.10.004.

2.78 X.Z. Wang, T.P. Muneshwar, H.Q. Fan, K. Cadien, J.L. Luo, Achieving ultrahigh corrosion resistance and conductive zirconium oxynitride coating on metal bipolar plates by plasma enhanced atomic layer deposition, J. Power Sources. 397 (2018) 32–36. https://doi.org/10.1016/j.jpowsour.2018.07.009.

2.79 I. Harayama, K. Nagashima, Y. Hirose, H. Matsuzaki, D. Sekiba, Development of ΔE-E telescope ERDA with 40 MeV 35Cl7+ beam at MALT in the University of Tokyo optimized for analysis of metal oxynitride thin films, Nucl. Instruments Methods Phys. Res. Sect. B Beam Interact. with Mater. Atoms. 384 (2016) 61–67. https://doi.org/10.1016/j.nimb.2016.07.019.

2.80 X. Wu, B. Huang, Q. Wang, Y. Wang, Evaluation of the role of nitrogen atoms in cobalt oxynitride electrodes for flexible asymmetric supercapacitors, Electrochim. Acta. 353 (2020) 136603. https://doi.org/10.1016/j.electacta.2020.136603.

2.81 M. Hojamberdiev, K. Kawashima, Exploring flux-grown transition metal oxynitride perovskites for photocatalytic water oxidation: A minireview, Energy Reports. 6 (2020) 13–24. https://doi.org/10.1016/j.egyr.2019.09.021.

2.82 J. Hirpara, V. Chawla, R. Chandra, Investigation of tantalum oxynitride for hard and anti-corrosive coating application in diluted hydrochloric acid solutions, Mater. Today Commun. 23 (2020) 101113. https://doi.org/10.1016/j.mtcomm.2020.101113.

UNIVERSITY of the WESTERN CAPE

2.83 Z. Wang, X. Liu, J. Liu, Y. Zeng, J. Shi, Y. Tong, X. Lu, Porous molybdenum tungsten oxynitrides enable long-life supercapacitors with high capacitance, J. Power Sources. 442 (2019) 227247. https://doi.org/10.1016/j.jpowsour.2019.227247.

2.84 R. Aguiar, D. Logvinovich, A. Weidenkaff, A. Rachel, A. Reller, S.G. Ebbinghaus, The vast colour spectrum of ternary metal oxynitride pigments, Dye. Pigment. 76 (2008) 70–75. https://doi.org/10.1016/j.dyepig.2006.08.029.

2.85 C. Pozo-Gonzalo, O. Kartachova, A.A.J. Torriero, P.C. Howlett, A.M. Glushenkov, D.M. Fabijanic, Y. Chen, S. Poissonnet, M. Forsyth, Nanoporous transition metal oxynitrides as catalysts for the oxygen reduction reaction, Electrochim. Acta. 103 (2013) 151–160. https://doi.org/10.1016/j.electacta.2013.04.012.

2.86 J. Ko, D.H. Cho, D. Kim, Y.S. Yoon, Suppression of formation of lithium dendrite via surface modification by 2-D lithium phosphorous oxynitride as a highly stable anode for metal lithium batteries, J. Alloys Compd. (2020) 156280. https://doi.org/10.1016/j.jallcom.2020.156280.

2.87 J. Oró-Solé, C. Frontera, A.P. Black, A. Castets, K.L. Velásquez-Méndez, J. Fontcuberta, A. Fuertes, Structural, magnetic and electronic properties of EuTi0.5W0.5O3-xNx perovskite oxynitrides, J. Solid State Chem. 286 (2020). https://doi.org/10.1016/j.jssc.2020.121274.

2.88 Q. Yang, Y. Masubuchi, M. Higuchi, Synthesis of perovskite-type oxynitrides SrNb(O,N)3 and CaTa(O,N)3 using carbon nitride, Ceram. Int. 46 (2020) 13941–13944. https://doi.org/10.1016/j.ceramint.2020.02.191.

2.89 S. Dutta, A. Indra, Y. Feng, H.S. Han, T. Song, Promoting electrocatalytic overall water splitting with nanohybrid of transition metal nitride-oxynitride, Appl. Catal. B Environ. 241 (2019) 521–527. https://doi.org/10.1016/j.apcatb.2018.09.061.

2.90 S. Venkataraj, D. Severin, S.H. Mohamed, J. Ngaruiya, O. Kappertz, M. Wuttig,

UNIVERSITY of the WESTERN CAPE

Towards understanding the superior properties of transition metal oxynitrides prepared by reactive DC magnetron sputtering, Thin Solid Films. 502 (2006) 228–234. https://doi.org/10.1016/j.tsf.2005.07.280.

2.91 A. Belosludtsev, N. Kyžas, A. Selskis, R. Narbutiene, Design, preparation and characterization of antireflective coatings using oxynitride films, Opt. Mater. (Amst). 98 (2019) 109430. https://doi.org/10.1016/j.optmat.2019.109430.

2.92 Q. Yang, Y. Masubuchi, M. Higuchi, Synthesis of perovskite-type oxynitrides SrNb(O,N)3 and CaTa(O,N)3 using carbon nitride, Ceram. Int. 46 (2020) 13941–13944. https://doi.org/10.1016/j.ceramint.2020.02.191.

2.93 D. Li, L. Zeng, B. Li, X. Yang, Q. Yu, Z. Wu, Rapid synthesis of dielectric tantalum-based oxynitrides, Mater. Des. 187 (2020) 108416. https://doi.org/10.1016/j.matdes.2019.108416.

2.94 C. Pozo-Gonzalo, O. Kartachova, A.A.J. Torriero, P.C. Howlett, A.M. Glushenkov, D.M. Fabijanic, Y. Chen, S. Poissonnet, M. Forsyth, Nanoporous transition metal oxynitrides as catalysts for the oxygen reduction reaction, Electrochim. Acta. 103 (2013) 151–160. https://doi.org/10.1016/j.electacta.2013.04.012.

2.95 J. Ko, D.H. Cho, D. Kim, Y.S. Yoon, Suppression of formation of lithium dendrite via surface modification by 2-D lithium phosphorous oxynitride as a highly stable anode for metal lithium batteries, J. Alloys Compd. (2020) 156280. https://doi.org/10.1016/j.jallcom.2020.156280.

2.96 F. Haydous, F. Waag, W. Si, F. Li, S. Barcikowski, B. Gökce, T. Lippert, The effect of downstream laser fragmentation on the specific surface area and photoelectrochemical performance of barium tantalum oxynitride, Appl. Surf. Sci. 510 (2020) 145429. https://doi.org/10.1016/j.apsusc.2020.145429.

2.97 J. Wang, Y. Asakura, S. Yin, Synthesis of zinc germanium oxynitride nanotube as a visible-light driven photocatalyst for NOx decomposition through ordered

UNIVERSITY of the WESTERN CAPE

morphological transformation from Zn2GeO4 nanorod obtained by hydrothermal reaction, J. Hazard. Mater. 396 (2020) 122709. https://doi.org/10.1016/j.jhazmat.2020.122709.




http://etd.uwc.ac.za/

# CHAPTER THREE

# 3. SYNTHESIS OF NiAl, OXYNITRIDES AND MMCs

## 3.1 FABRICATION OF NiAl ALLOY

Elemental Ni (99.8%) and Al (99.9%) powders were blended to obtain a homogeneous mixture at 1:1 at. ratio. The blended powder was then cold pressed into cylindrical (17mm diameter) coupons at 15 MPa. The cold-pressed coupons were sintered at 750 °C ± 10 °C and 1300 °C ± 10 °C in a tube furnace in air. At 750 °C the three compact samples were sintered for 24, 48 and 120 h each while at 1300 °C ± 10 °C three samples were annealed for 24 h followed by air cooling. The 1300 °C – sintered samples (brittle lumps) were easily crushed into powder by using a porcelain rod in a porcelain bowl due to their brittle nature after sintering. The 750 °C (120 h) was subjected to thermal oxidation at similar temperature and time (750 °C (120 h).

UNIVERSITY of the
WESTERN CAPE

## 3.2 FABRICATION OF TiC-REINFORCED NiAl BASED ALLOY

Elemental Ni (99.8%), Al (99.9%) and nanoparticles (50 – 100 nm) of TiC powders were blended according $Ni_{62.5}Al_{37.5}TiC_{1.28}$ composition. The powder mixture was cold-pressed into cylindrical (17mm diameter) coupons at 20 MPa and sintered at 650 ºC in a Carbolite tube furnace flowing with argon (Ar) for 6 hours (h). The morphology of the Ni, Al and TiC powders, the microstructure of the sintered and polished NiAlTiC were investigated using a high-resolution scanning electron microscope (HR-SEM, Auriga ZEISS) coupled with a Robinson Backscatter Electron Detector and an Oxford Link Pentafet energy dispersive x-ray spectroscopy (EDS) detector. MicroVickers hardness tests were performed applying a load of 300 Kgf and dwelling time of 10s were employed for the micro-hardness

measurements. Hardness profiles throughout the specimens were measured at 0.2mm intervals and average of 32 measurements.

## 3.3 FABRICATION OF TiC-REINFORCED STEEL BASED ALLOY

The steel powder is composed 0.68 wt.% Si, 1.78 wt.% Cr, 1.08 wt.% Mn and 0.29 wt.% C. The steel and nickel powders were mixed at 3:1 weight ratio and added to 1.0 and 1.5 wt% nanosized (50 – 100 nm) TiC powder, respectively. The 3:1 powder ratio in composition was chosen since Ni is an austenite stabilizer to induce ductility of the matrix. Addition of 1.0 and 1.5 wt% nanosized TiC powder was added to improve the hardness of the composite material and produce a composite material with combination of hardness and ductility. Powder mixtures were then cold pressed at 30 MPa enough pressure to produce compacts with minimum porosity, sintered in the argon flowing tube furnace at 1400 °C for 2 hours to avoid contamination such as $O_2$ and $N_2$ gases. Metallographic examinations were conducted on the as-sintered specimens, which were ground up-to 4000 SiC grit papers, with subsequent polishing in colloidal silica. The microstructures were observed by the scanning electron microscopy (SEM) which is equipped with energy dispersion spectroscopy (EDS) for micro-analyses. In addition to this, phase identification was performed using x-ray diffraction (XRD) technique with CuKα radiation λ=1.54062 Å and 2θ from 20°-90°. Micro-Vickers hardness (HV) measurements were performed at applied load of 500 gf and dwelling time of 10s. Hardness profiles throughout the specimens were measured at average of at-least 10 measurements.

UNIVERSITY of the WESTERN CAPE

## 3.4 FABRICATION OF Ti OXYNITRIDE

Atomised commercially pure (CP) Ti (99.8%) powder was used in the current investigation. Samples of CP Ti powder were annealed in a muffle furnace for 2 h in air at 500, 600, 700 and 800 °C, respectively followed by furnace-cooling. Another sample of CP Ti powder was annealed at 800 °C followed by air-cooling. The density of the powders was measured by Micromeritics AccuPyc II 1340 Gas Pycnometer. Powder morphology analysis was conducted using a high-resolution scanning electron microscope (HR-SEM, Auriga ZEISS) coupled with a Robinson Backscatter Electron Detector and an Oxford Link Pentafet energy dispersive x-ray spectroscopy (EDS) detector. Phase evolution was determined with the use of a PANalytical X'pert PRO PW 3040/60 X-ray diffraction (XRD) machine, using Cu Kα radiation as source. The topography of the spherical Ti powder particles was analysed using atomic force microscopy (AFM, Veeco, Digital Instruments). Thermal analysis was carried out using Differential Scanning Calorimetry (DSC) and Thermo Gravinometry (TG) incorporated in NETZSCH STA. Powder samples were heated up to 1200 °C and cooled to room temperature using $Al_2O_3$ as a baseline during the thermal analysis. A heating rate of 20 °C $min^{-1}$ under argon gas with 20 ml/L standard flow rate was used.

UNIVERSITY of the WESTERN CAPE

## 3.5 FABRICATION OF Ti OXYNITRIDE-REINFORCED NiAl BASED ALLOY

Atomised pure Ti (99.8%) powder was used in the current investigation. The powder was annealed in a muffle furnace for 2 h under normal air atmospheric conditions at 500, 600, 700, 800 °C followed by furnace cooling. On another experiment, the powder was annealed at 800 °C followed by air-cooling. Micromeritics AccuPyc II 1340 Gas Pycnometer measured the density of the powders. Microstructural examinations were

http://etd.uwc.ac.za/

conducted using conventional methods. The specimen alloys were ground up-to 4000 SiC grit papers into a mirror-like surface, with subsequent polishing in colloidal silica. The morphology of the crushed powders was investigated using a high-resolution scanning electron microscope (HR-SEM, Auriga ZEISS) coupled with a Robinson Backscatter Electron Detector and an Oxford Link Pentafet energy dispersive x-ray spectroscopy (EDS) detector. Phase evolution was determined with the use of a PANalytical X'pert PRO PW 3040/60 X-ray diffraction (XRD) machine, using Cu Kα radiation as source. The surface morphology of the powders was characterized using Zeiss-Auriga field-emission scanning electron microscope (FE-SEM) attached with a Robinson Backscatter Electron Detector (RBSD) and an Oxford Link Pentafet energy dispersive x-ray spectroscopy (EDS) detector. A PANalytical X'pert PRO PW 3040/60 X-ray diffraction (XRD) machine fitted with a Cu Kα radiation source was used to probe the structure and crystallinity of nanostructures.

UNIVERSITY of the
WESTERN CAPE

http://etd.uwc.ac.za/

# CHAPTER FOUR

## Investigation into the thermal behaviour of the B2–NiAl intermetallic alloy produced by compaction and sintering of the elemental Ni and Al powders

*Published in Vacuum Journal*

**Abstract**

A cubic B2–NiAl alloy was synthesized by mixing of elemental Ni and Al powders followed by cold compacting and sintering of some samples at 750 °C and other samples at 1300 °C. The alloys sintered at 1300 °C exhibited a brittle B2–NiAl structure easily crushable into powder, while the 750 °C sintered alloys were not nearly as brittle. Electron Backscatter Diffraction (EBSD) results show that the B2–NiAl alloy sintered at 750 °C for a longer time (120 h) has larger grain size associated with the <111> -oriented grains encountering high mobility boundaries than the alloy sintered at 750 °C for a shorter time (48 h). Sample morphologies were analysed using the Scanning Electron Microscope (SEM). Structural development of the alloy was studied via the x-ray diffraction (XRD) technique. The B2–NiAl intermetallic developed a thin scale of stable $Al_2O_3$ alloy due to oxidation in air at 750 °C for 120 h. As a result, further oxidation on the sample's surface was restricted, except the traces of $Al_2O_3$ formed via intergranular oxidation transformed into a metastable monoclinic oxynitride phase due to nitrogen (N) contamination.

**Keywords:** B2-NiAl, Brittle, Cubic, Intermetallic, EBSD

UNIVERSITY of the WESTERN CAPE

## 4.1 Introduction

Nickel aluminide (Al–Ni) are promising materials for high-temperature applications due to high stability of the $Al_3Ni$ eutectic at elevated temperatures. This important heat-resistant class of alloy materials is used in manufacturing of aerospace gas turbine engine blades. The major drawback of this alloy class is making them into a net or near net components owing to their poor machinability **[1]**. Ni–Al compounds have an excellent combination of mechanical, physical and chemical properties such as low density, high melting point, high temperature oxidation resistance, high strength and catalytic characteristics **[2, 3]**. These alloys are also widely used as coatings for protecting low temperature substrate materials from high temperature corrosion in oxidizing or carburizing atmospheres **[4–6]**. NiAl–based composites exhibit excellent wear properties at high temperatures **[7]**. The microstructure of nanocrystalline NiAl has been studied extensively to understand their properties **[8]** including corrosion behaviour **[9]**. This class of materials has found application in the petrochemical industry as a catalyst **[10, 11]**. Rayhan et al. **[12]** studied the reduction of benzophenones and concluded that the nature of the hydrogenated products depends on temperature, reaction time, volume of water, and amount of Raney Ni–Al alloy being used (in/during) environmentally friendly chemical process. Raney Ni–Al alloy in water is a powerful reducing agent **[12]**. Additionally, Xu et al. **[13]** utilized Ni–Al compounds for the decomposition of methanol into $H_2$, CO and $CO_2$. Formation of intermetallic Al–Ni alloy occurs through exothermic reactions between Ni and Al **[14–17]**. The intermetallic can be successfully formed via mechanical alloying of elemental Ni and Al powder mixtures **[18–20]**. Nanocrystalline NiAl materials are fabricated via mechanical alloying of elemental Ni and Al powders followed by hot-pressing sintering technique. Al–Ni nano-powder with 45 at.% nickel has been synthesized via explosion of electrically heated twisted pure Al and Ni wires in an argon atmosphere **[21]**. This combustion

UNIVERSITY of the WESTERN CAPE

reaction between Al and Ni takes place in a thermal explosion mode under near adiabatic conditions **[22]**. At temperatures between 1300 °C and 1600 °C, β-NiAl generates sudden heat and an increase in temperature to produce an alloy with good ductility **[22]**. The production of the intermetallic has been reportedly carried out in an electrical resistance furnace in open air under 150 MPa uniaxial pressure at 1050 °C for 1 h **[23]**. Dong et al. **[24]**, reported a porous NiAl synthesized form 575 °C–750 °C temperature range after pre-heating at 575 °C. In their study, Dong et al. concluded that the pore size strongly depends on the volume expansion determined by the intensity of exothermic reaction from the preheating temperature to the final sintering temperature. Hinstling–Brounstein diffusion model showed that the thermal explosion phenomenon is impossible at solid-phase interaction **[25]**. The NiAl intermetallic alloy has a poor fracture toughness at room temperature due to its high ordering energy with slip limited to <100> plane as its three independent slip systems are below the ductile-to-brittle transition temperature (DBTT) **[26]**. During fabrication of AlNi alloy, sintering has been explored at various temperatures and environments. For example, Dong et al. **[24]**, preheated the NiAl compacts prior to sintering at 1000 °C under controlled environment. The reaction between Ni and Al has been found to occur at the melting temperature of aluminium resulting in a temperature rise to between 854 °C and 1300 °C in multilayer Ni/Al reaction piles conducted in vacuum **[22]**. In the current study, we studied the difference in Ni50Al powder compacts sintered at 750 °C and 1300 °C in air. The effect of air cooling from 1300 °C and material characterization are discussed in detail including EBSD technique to determine the preferential growth of grains with <111> orientations.

UNIVERSITY of the
WESTERN CAPE

## 4.2 Experimental Details

*Experimental work*

Elemental Ni (99.8%) and Al (99.9%) powders were blended to obtain a homogeneous mixture at 1:1 at. ratio. The blended powder was then cold pressed into cylindrical (17mm diameter) coupons at 15 MPa. The cold-pressed coupons were sintered at 750 °C ± 10 °C and 1300 °C ± 10 °C in a tube furnace in air. At 750 °C the three compact samples were sintered for 24, 48 and 120 h each while at 1300 °C ± 10 °C three samples were annealed for 24 h followed by air cooling. 24, 48 and 120 h sintering temperatures were picked as durations whereby any structural chages due elevated temperature exposure in air would be expected to occur. The 1300 °C – sintered samples (brittle lumps) were easily crushed into powder by using a porcelain rod in a porcelain bowl due to their brittle nature after sintering. The 750 °C (120 h) was subjected to thermal oxidation at similar temperature and time (750 °C (120 h).

*Characterization*

UNIVERSITY of the
WESTERN CAPE

The morphology of the elemental Ni and Al, blended nickel aluminium (NiAl) powders as well sintered NiAl was investigated using a high-resolution scanning electron microscope (HR-SEM, Auriga ZEISS) coupled with a Robinson Backscatter Electron Detector and an Oxford Link Pentafet energy dispersive x-ray spectroscopy (EDS) detector. Samples analysed using EBSD were polished up to colloidal silica followed by electro-polishing according to Mathabathe et al. **[27]**. The specimens produced good diffraction patterns, and orientation determination consisted of 1, Kikuchi band detection, 2, Kikuchi band identification. It has indexing of pattern, 3, determination of orientation which was based on calculation of the orientation of the corresponding crystal lattice with respect to reference frame. The crystal orientation is then defined by three Euler angles ($\phi 1$, $\varphi$, $\phi 2$) Stojakovic **[28]**. Representation of successive conventional rotations to match the crystal

orientation with a Cartesian co-ordinate system related with sample surface **[27]**. Furthermore, grain orientation, was studied using advanced fit band detection and indexing algorithm, the HKL CHANNEL 5. Phase evolution was determined with the use of a PANalytical X'pert PRO PW 3040/60 X-ray diffraction (XRD) machine, using Cu Kα radiation as a source. Thermal analysis of the milled powder (brittle sample sintered at 1300 °C) as well as the three samples with high 3- dimensional stability (sintered at 750 °C) was carried out using a Differential Scanning Calorimetry (DSC). Three samples sintered at 750 °C were sectioned using a precision cutter with diamond blade to 3×3×3mm and heated up to 1200 °C in air and cooled to room temperature for the DSC evaluation. The green density and porosity of the Ni50Al compacts were determined by using the Archimedes' principle using water as the medium. A Micromeritics AccuPyc II 1340 gas pycnometer was used to measure the true density of the sintered material while the Microtrac Bluewave Particle Size Analyser was used to measure the particle sizes of the elemental Ni and Al. Oxygen content on the sintered NiAl was determined by means of ELTRA ONH 2000 PC under Helium gas atmosphere. Microhardness measurements on the sintered samples was performed according to ASTM standards E384-11.

UNIVERSITY of the
WESTERN CAPE

A load of 20 kg/f was applied with a dwelling time of 10s were employed during the microhardness testing. The hardness on the sintered samples was measured from the surface into the bulk of the specimen. Nine hardness measurements were taken at each fixed distance from the surface (and at 0.2mm intervals) and an average hardness value (for the particular distance) was computed from the nine values.

http://etd.uwc.ac.za/

## 4.3 Results and Discussion

*4.3.1 Low temperature annealing (750 °C)*

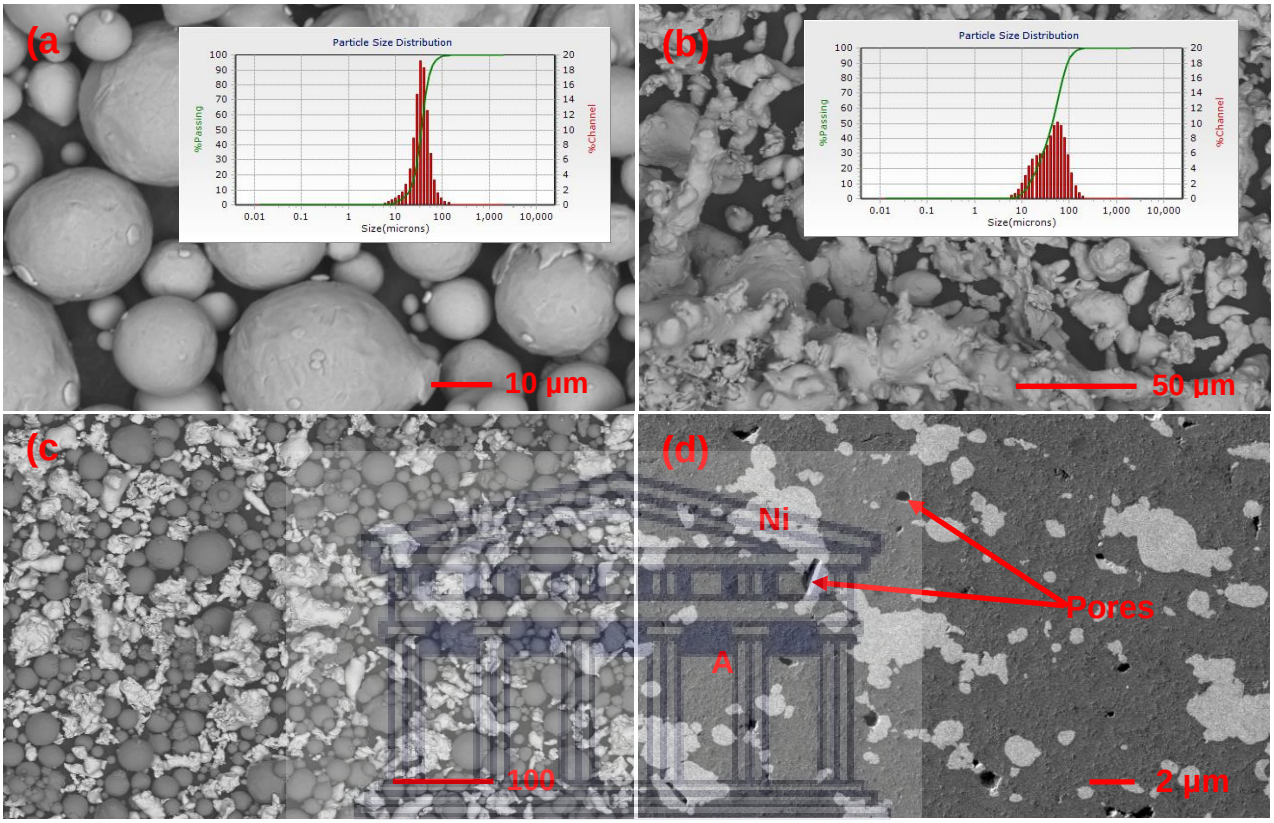


UNIVERSITY of the WESTERN CAPE

**Figure 4.1**: SEM images of (a) Al, (b) Ni, with particle size distribution analysis (inset) (c) Blended and (d) cold pressed Ni50Al powder particles.

esSEM images of the elemental (a) Al, (b) Ni and the (c) blended NiAl powders are shown in Fig. 4.1. The Al powder particles are spherical with a narrow particle size range d50=35.20 µm which complement the SEM results. Ni powder has irregular/dendritic powder particles with a broad particle size range distribution d50=43.64 µm. After mixing Ni and Al powders (Fig. 4.1c), the powder was cold pressed into green compacts prior to sintering. SEM image of a compacted pellet, cross sectioned and polished is shown in Fig. 4.1d. Deformed elemental Ni and Al particles are fused together with minor spherical and irregular shaped pores widely distributed across the sample. It was previously shown

http://etd.uwc.ac.za/

that cold compaction is an important factor prior to sintering since re-arrangement of particles and crystal orientation is realized **[29]**. Green density of the samples was determined by the Archimedes principles while the density of the sintered samples were measured by the Pycnometer and porosity was determined according to eq. (2). Table 4.1 displays the calculated densities of the green compacts ranging from 4.701 g/cm$^3$ to 4.810 g/cm$^3$ obtained by using eq. (1). Upon sintering at 750 °C for 24, 48 and 120 h, the densities of the samples increased to 5.59 ± 0.081 g/cm$^3$, 5.61 ± 0.065 g/cm$^3$, 5.65 ± 0.032 g/cm$^3$, respectively. The sample sintered 1300 °C (24 h) measured a density of 5.60 ± 0.069 g/cm$_3$. From the theoretical density of the B2 NiAl (5.913 g/cm$^3$) **[30,31]**, the relative densities upon sintering for 24, 48 and 120 h (750 °C) are computed at 94.5%, 94.9% and 95.6% (**Table 4.1**).

$$\rho = \frac{m}{v} \qquad (1)$$

where ρ (density of the sample), m=mass and v=volume. Porosity can thus be calculated using the relation:

$$\sigma = 1 - \frac{\rho_t}{\rho_m} \qquad (2)$$

where σ is porosity, $\rho_t$ is the theoretical density while $\rho_m$ is the measured density. The oxygen content of the B2 NiAl alloy progressively increased upon sintering at 750 °C from 0.103 ± 0.026% (24 h), 0.120 ± 0.031% (48 h) and 0.152 ± 0.045% (120 h). The 1300 °C sintered sample has an oxygen content of 0.276 ± 0.027%. After additional oxidation for 120 h on of the 750 °C sample sintered for 24 h, the oxygen content further increased to 2.499 ± 0.332%.

UNIVERSITY of the WESTERN CAPE

http://etd.uwc.ac.za/

**Table 4.1**: The Green, sintered, relative densities and % porosity of the B2 NiAl alloys sintered at 750 °C for 24, 48,120 h and 1300 °C (24 h).

| Sample | Green Density | Measured Density (ρ) (g/cm$^3$) after sintering | Relative Density (%) after sintering | Porosity (%)after sintering |
|---|---|---|---|---|
| Ni–Al solid (750 °C) 24 h | 4.701 | 5.59 ± 0.081 | 94.5 | 5.50 |
| Ni–Al solid (750 °C) 48 h | 4.758 | 5.61 ± 0.065 | 94.9 | 5.10 |
| Ni–Al solid (750 °C) 120 h | 4.810 | 5.65 ± 0.032 | 95.6 | 4.40 |
| Ni–Al powder (1300 °C) 24 h | 4.756 | 5.60 ± 0.069 | 94.7 | 5.30 |

**Fig. 4.2** shows the SEM images of the NiAl upon sintering for 24, 48 and 120 h at 750 °C in air. The microstructure in **Fig. 4.2a** reveals some porosity and oxides formed preferentially at the grain boundaries. Microstructures are showing an equiaxed structure with defined grains formed after an exothermic reaction between Ni and Al (**Fig. 4.2a–c**). The increased holding time encouraged grain growth and densification as seen in **Fig. 4.2a–c**.

To investigate the structural development of the sintered samples, XRD analysis was conducted. Fig. 4.3a–c shows the XRD pattern revealing a single cubic NiAl phase when sintered at 750 °C for 24, 48 and 120 h. Lattice parameter 2.881 Å was detected on the 24 and 48 h samples. These lattice parameters belong to the cubic AlNi crystal structure with Pm-3m # 221 space group and number matched by the PDF reference code 00-044-1186 (24, 48 h) and chemical formula Al0·96Ni1.04. Furthermore, the 120 h samples has 2.887 Å lattice parameter and cubic structure according to the standard JCPDS file by the reference code 03-065-0420 with AlNi chemical formula. The observed cell parameters in the table are derived from powder lines or diffraction spots with ranges of the standard deviations (SD), coefficient of variation (%), standard deviation error of 0.0126, 0.4385 and 0.0056, respectively. Previous studies revealed a range in lattice parameters in B2–NiAl such as 2.866 Å, 2.842 Å and 2.839 Å determined by Nelson and Riley method

UNIVERSITY of the WESTERN CAPE

during mechanical alloying **[32]**. Moreover, the stoichiometric B2 AlNi calculated using the embedded atom method (EAM) yielded lattice parameter of 2.83 Å **[33]**.

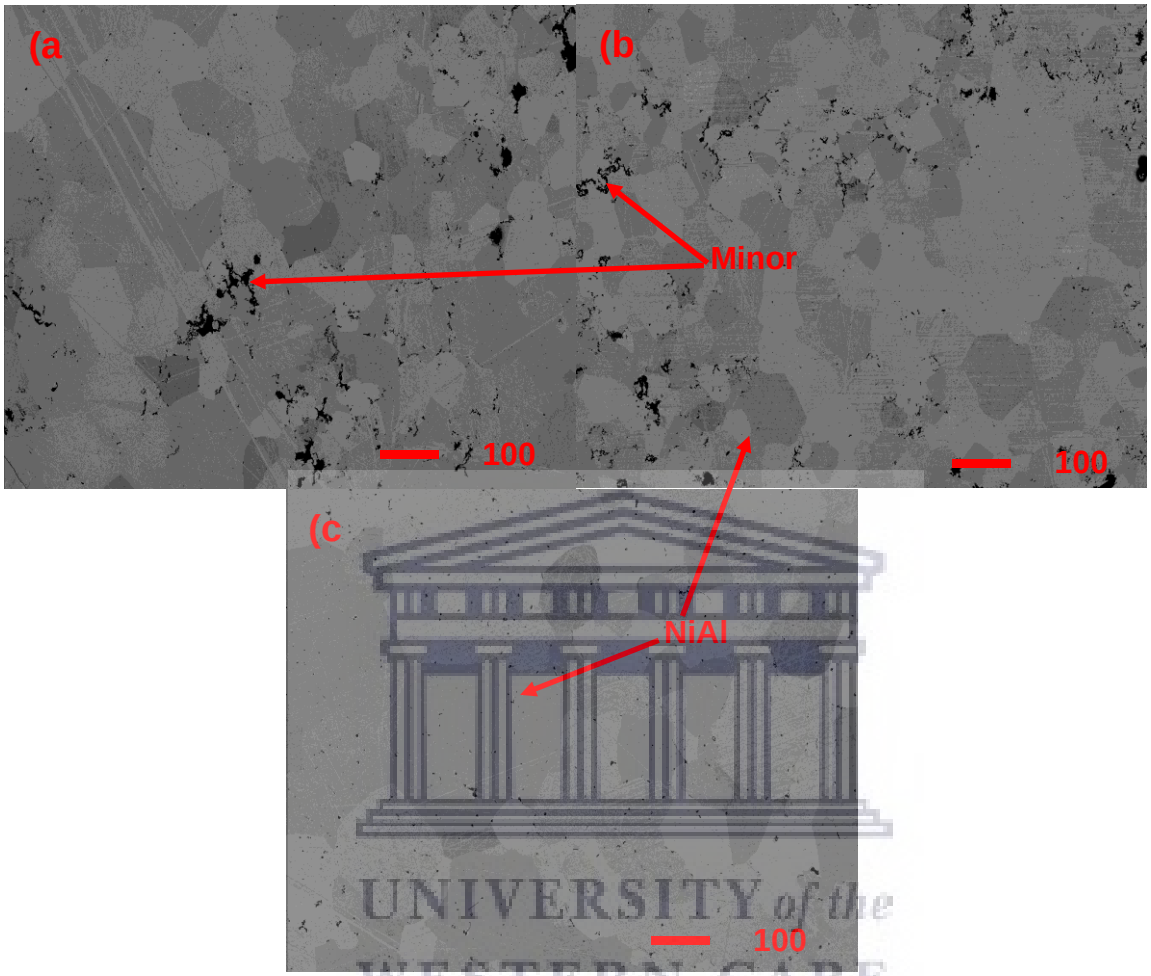


UNIVERSITY of the
WESTERN CAPE

**Figure 4.2**: SEM images of the NiAl alloy sintered for (a) 24, (b) 48 and (c) 120 h at 750 °C in air.

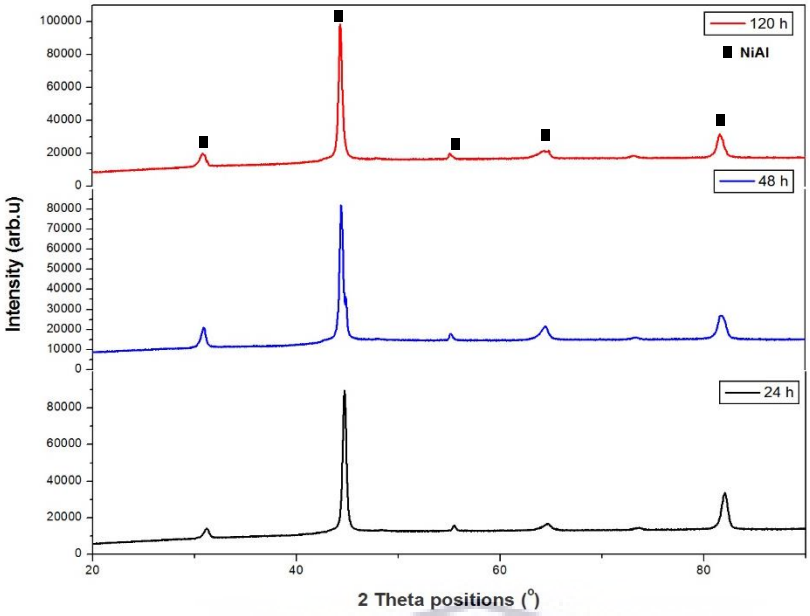


**Figure 4.3**: XRD pattern of the NiAl compacts sintered at 750 °C for 24, 48 and 120 h in air.

Therefore, the lattice parameters of the B2–NiAl can vary as observed in the current study. The crystal structure of NiAl is primitive cubic CsCl structure and its space group is Pm-3m different to body centered cubic structure. Although the presence of minor oxide phase was observed in the SEM image (**Fig. 4.2**), it could not be detected by the XRD technique. In order to validate the crystallography of the sintered NiAl alloys, the samples with the least % porosity after sintering (48 and 120 h) were analysed using EBSD. The phase distribution map of the NiAl alloy sintered at 750 °C for 48 h is shown in **Fig. 4. 4**.

A single B2–NiAl phases perforated by pores and oxides are shown in **Fig. 4.4a–c**. **Fig. 4.4c** shows the orientation map for indexing with a generic FCC structure of the B2- phase and corresponding IPF colouring scheme. This reveals a true intrinsic mechanism of reactive nucleation and growth; atomic intermixing between layers of FCC (Ni and Al) with interfaces orientated normal to the [001] direction.

UNIVERSITY of the WESTERN CAPE

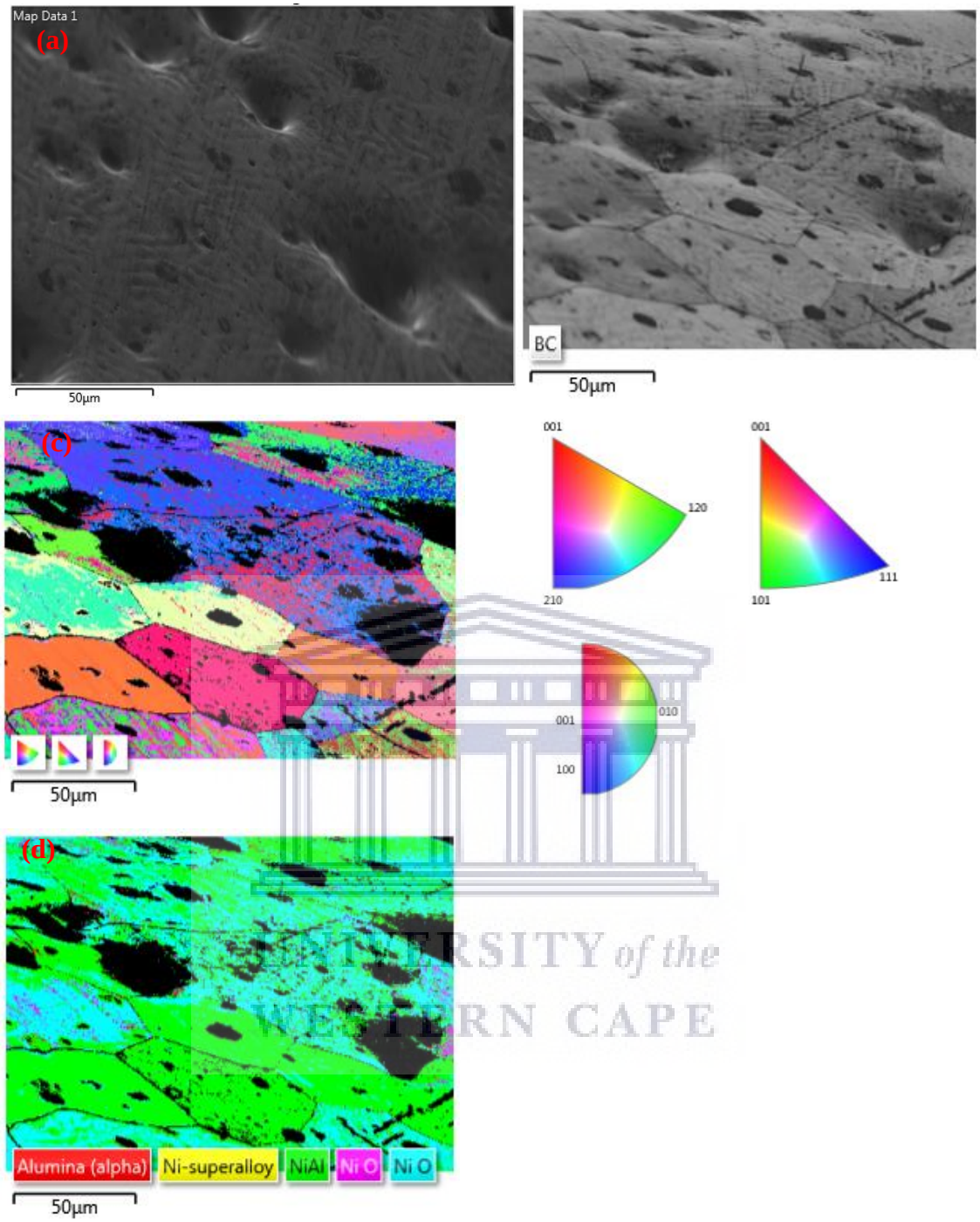


**Figure 4.4**: EBSD map analysis of the NiAl alloy sintered at 750 °C for 48 h (a) Electron image, (b) Band contrast image, (c) Inverse pole figure maps (IPF) and (d) Phase colour map. (For interpretation of the references to colour in this figure legend, the reader is referred to the Web version of this article).

UNIVERSITY of the WESTERN CAPE

The orientation map (**Fig. 4.4c**) shows the most substantial contrast between the large irregularly shaped regions with strong <110> fiber texture and localities with small equiaxed grains and a more random orientation. The phase colour map of the resulting B2 NiAl is shown **Fig. 4.4d**. On prolonged sintering (120 h), the large <110> - orientated regions were formed as shown in **Fig. 4.5c**.

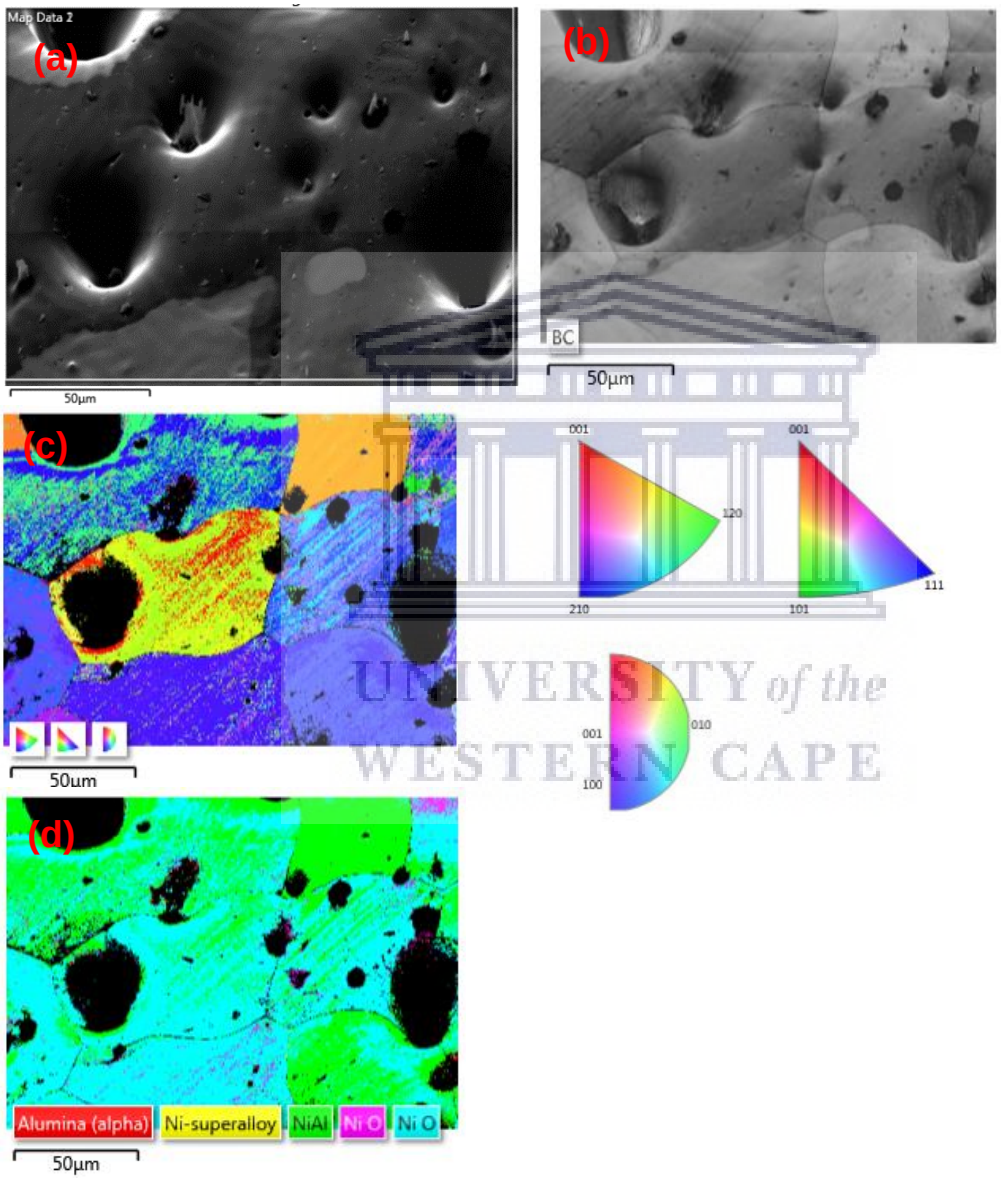


**Figure 4.5**: EBSD maps of the NiAl alloy sintered at 750 °C for 120 h (a) Electron image, (b) Band contrast image, (c) Inverse pole figure maps (IPF) and (d) Phase colour map. (For interpretation of the references to colour in this figure legend, the reader is referred to the Web version of this article).

UNIVERSITY of the WESTERN CAPE

These large <110> -oriented domains may be deformed grains observed on the 24 h sintered microstructure prior to recrystallization. The volume fraction of the irregular shaped <110> grains in NiAl sintered at 750 °C for 120 h is smaller than sintered for 24 h, depicting that the <100> grains in this specimen alloy were formed by dynamic recrystallization. Harris et al. **[34]**, reported that the <111> fiber textures are mainly associated with deformation at higher temperatures, retained or strengthened by annealing. Since grain boundary is related to the distribution of grain orientations **[34]**, shown by the grain boundary maps in (**Fig. 4.6 a-b**), the crystallographic texture in NiAl evolution may lead to the ability to modify drawbacks such as cracking and porosity.


**Figure 4.6**: Grain boundary maps of the NiAl alloy sintered at 750 °C for: (a) 48 and (b) 120 h.

Additionally, as noted in the orientation map **Fig. 4.5c**, the <111> -oriented grains are a fraction of recrystallized grains and are larger than the mean grain size. The alloy sintered at 750 °C for 120 h has larger grain size compared to the alloy sintered at 48 h, which suggest that these <111> -oriented grains have high mobility boundaries (**Fig. 4.6b** over that in **Fig. 4.6a**) which gave them an advantage during grain growth. According to the NiAl phase diagram, the Ni50Al composition begins to solidify from 1638 °C with a wider

http://etd.uwc.ac.za/

range of concentration which narrows with cooling (top→bottom analysis) on Ni50at.%Al alloy composition. This mechanism is a thermodynamic feasibility of the melting and solidification route.

The NiAl phase diagram confirms the stability of the B2–NiAl at room temperature (**Fig. 4.7**). Powder metallurgical route of producing NiAl is not represented in the equilibrium phase diagram. On contrary, compacted NiAl alloy powder inherits the bottom → top direction but involves the melting of Al at 660 °C followed by Ni dissolution in liquid aluminium. The schematic illustration of the formation mechanism upon liquid sintering is shown in **Fig. 4.8**. The exothermic reaction occurs immediately after formation of Al liquid and continues as Ni dissolves through a solid–liquid non-equilibrium interface **[22]**.

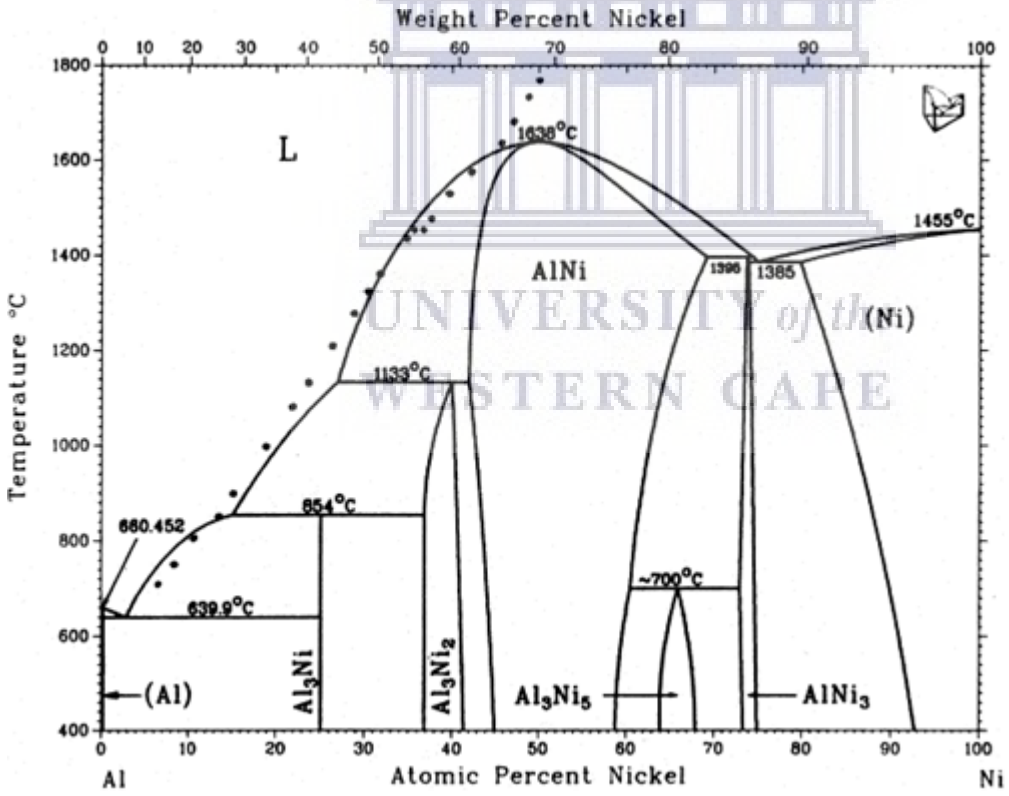


**Figure 4.7**: Al–Ni phase diagram.

UNIVERSITY of the WESTERN CAPE

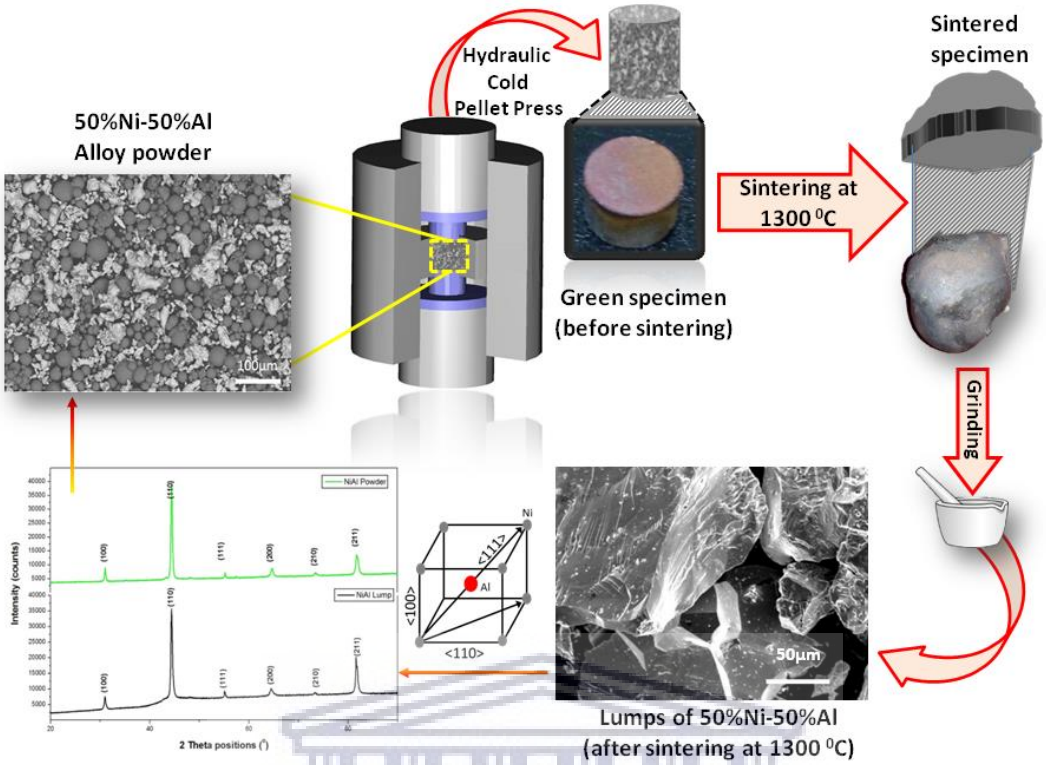


**Figure 4.8**: Schematic illustration of the formation mechanism of NiAl by sintering of elemental powders at 1300 °C in air.

Due to supersaturation, solid equilibrium NiAl forms around 750 °C and generates excessive heat associated with a sudden increase in temperature according to the chemical reactions (3), (4) and (5) below. The sample sintered at 1300 °C followed by quenching in air yielded brittle and fragile samples detected by the Reference code: 03-065-0420 easily crushed into powders, while the samples sintered at 750 °C exhibited an excellent 3D shape stability.

$$Ni + 3Al = NiAl_3 \text{ -150 kJ mol}^{-1} \quad (3)$$

$$NiAl_3 + Ni = Ni_2Al_3 \text{ -56 kJ mol}-1 \quad (4)$$

$$1/3Ni_2Al_3 + 1/3Ni = NiAl \text{ - 118 kJ mol}-1 \quad (5)$$

UNIVERSITY of the WESTERN CAPE

The $NiAl_3$ intermetallic phase has the highest Gibbs free energy of formation followed by the NiAl chemical reaction. Formation of the brittle intermetallic NiAl (subsequently crushed into powder) was made possible by the existence of intergranular cracking induced during air cooling from 1300 °C. Localized internal stresses in the grain boundaries existed since the alloy lacks sufficient slip systems **[35]**. Furthermore, the vacancy concentration (which is the other source of increased stress) depends on the stress state or extent of deformation **[35]**. Thermal stability and oxidation analysis of the sintered B2–NiAl samples is shown in **Fig. 9**.

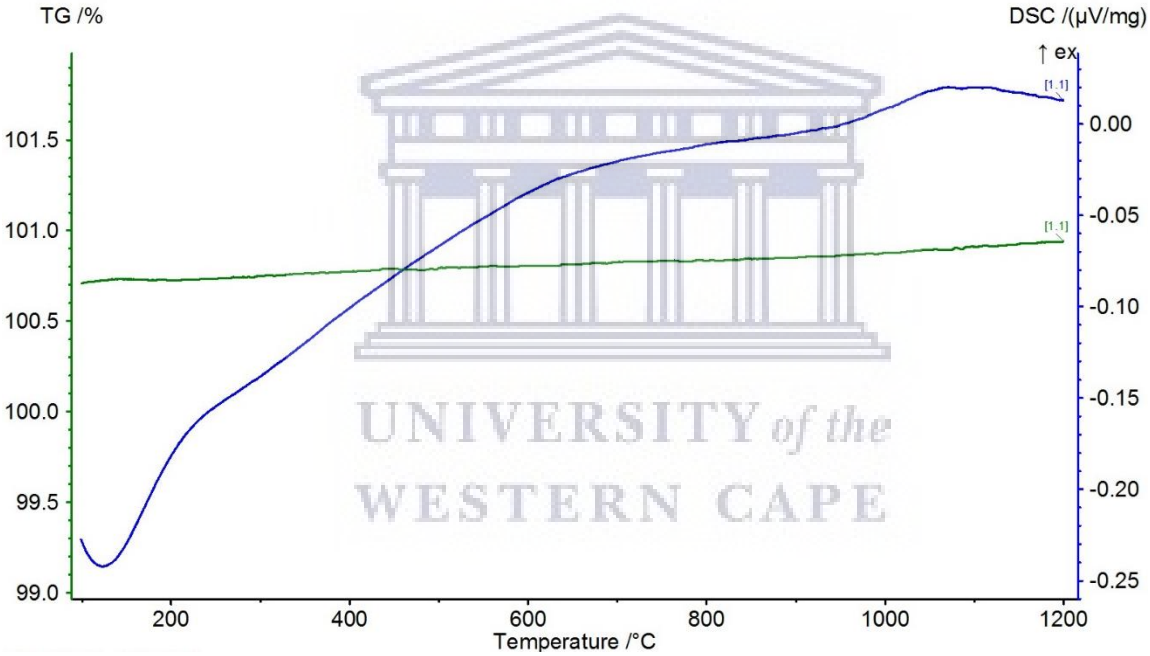


**Figure 4.9**: DSC-TG analysis of the 750 °C β-NiAl intermetallic alloy in air.

The DSC-TG curve of the sample sintered at 750 °C was conducted from 0 to 1200 °C in air. There is no evidence of phase transformation implying that the alloy is thermally stable in this temperature range. The presence of unreacted Ni and Al could have resulted in an endothermic peak due to second order phase transition **[36]** and melting, respectively. Weight gain due to oxidation is negligible from 0 °C to 1200 °C for one thermal cycle.

http://etd.uwc.ac.za/

Microhardness samples were sectioned normal to the oxidized surface and profiles of the samples sintered at 750 °C for 24, 48 and 120 h are shown in **Fig. 4.10**.

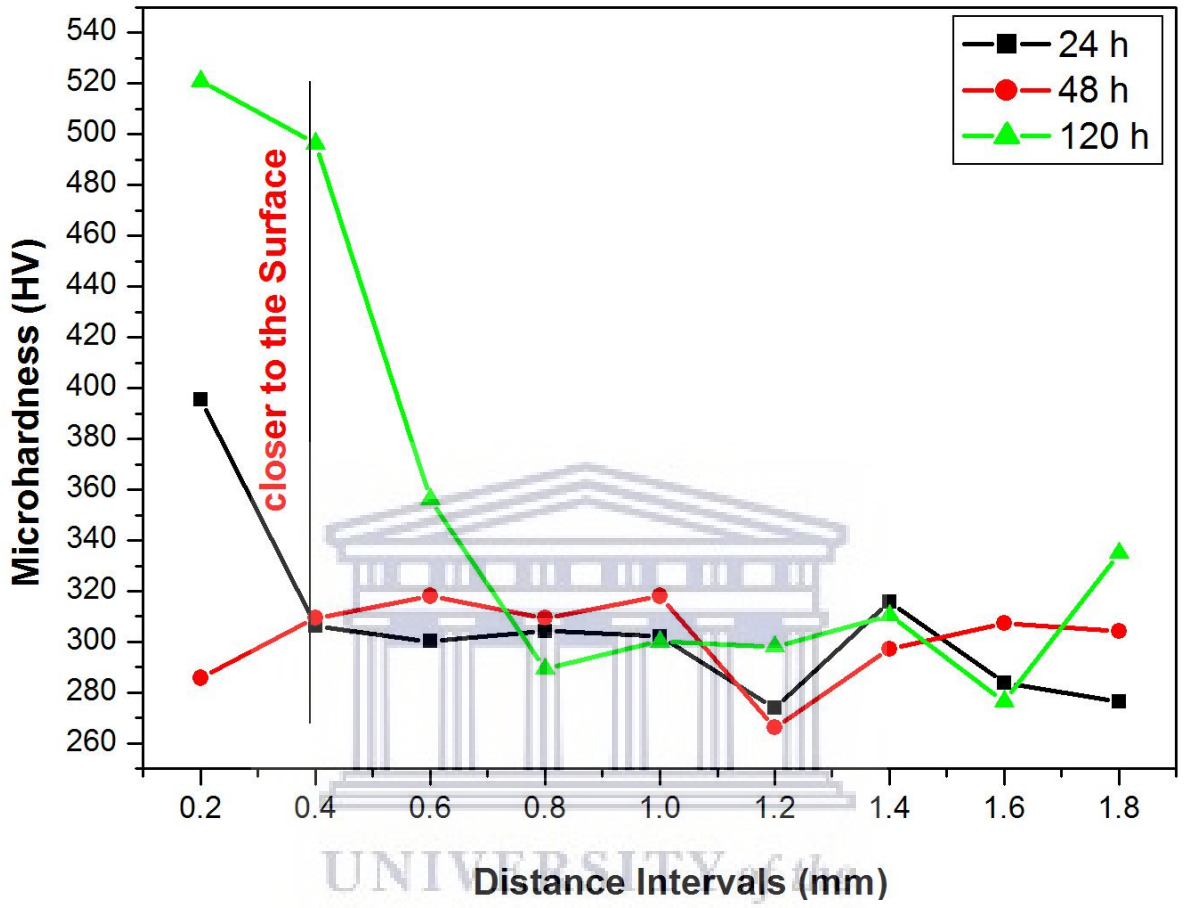


UNIVERSITY of the
WESTERN CAPE

**Figure 4.10**: The microhardness of the B2–NiAl sintered at 750 °C for 24, 48 and 120 h.

The surface layer of the samples display high hardness values due to oxidation when compared to the core area later (case) of the 24 and 120 h samples which is attributable to surface oxidation. The 24 h sample averaged 390 ± 17 HV while the 120 h yielded 520 ± 13 HV surface hardness. NiAl alloys were generally softer (290 ± 15 to 320 ± 19 HV) on the core and harder on the case for 24 h and 120 h, respectively. The surface of the sample sintered for 48 h is softer. This behaviour is unexpected and it could be due to some porosity on the sample surface. **Fig. 4.11** shows the SEM images of the B2–NiAl

intermetallic lump formed after sintering at 1300 °C for 24 h followed by air cooling. It has been reported that the formation of B2–NiAl is exothermic and sudden heat is generated at 1300 °C **[22]**. **Fig. 4.11a** shows the SEM micrograph of the brittle and fractured surfaces of NiAl intermetallic alloy with cleavage and chevron patterns mode of failure along the grain boundaries. The sintered samples were fragile and easily crushed/ground into powder form. The crushed powder in **Fig. 4.11b** shows distinguished fracture planes. A core-shell structure can be seen with a rod-type particle (core) protruding from the shell (case) in **Fig. 4.11c** and d typical of the developmental process for the crystal growth **[37]**.

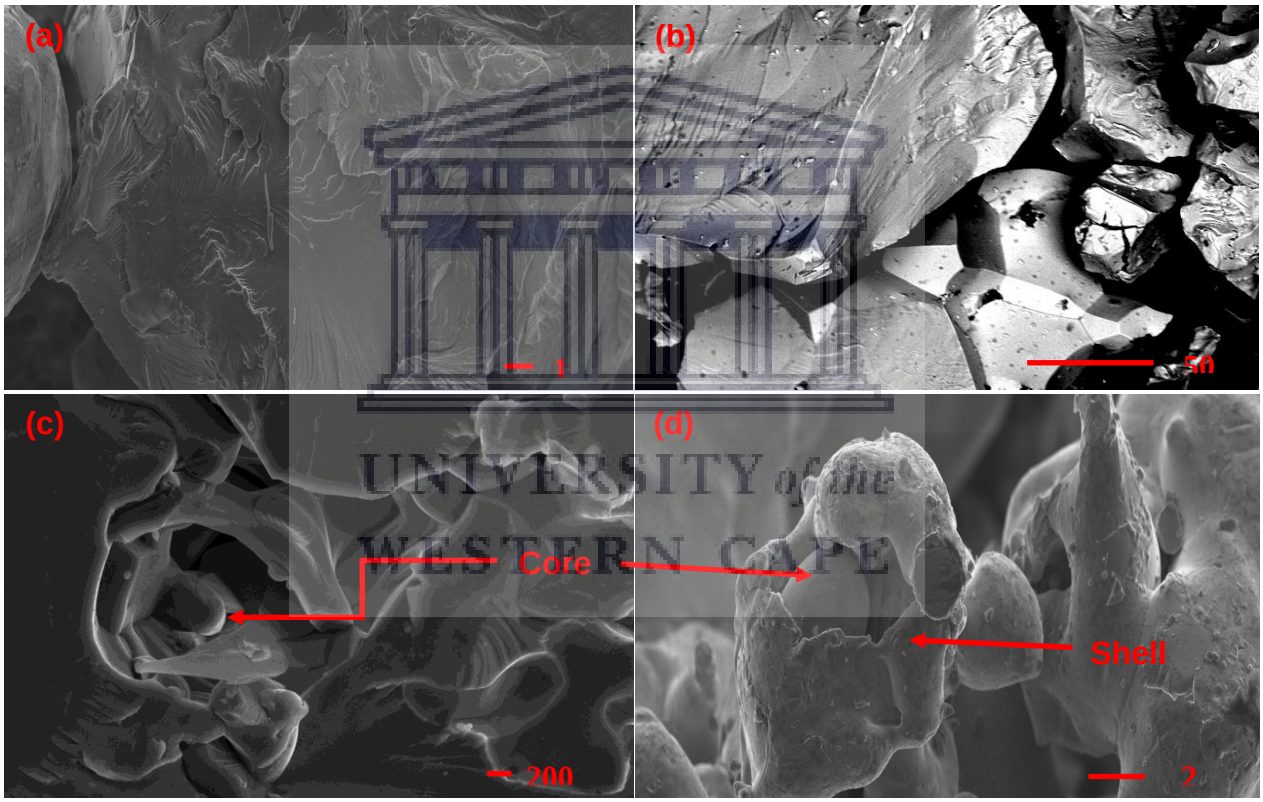


**Figure 4.11**: a-d: SEM images of sintered NiAl lumps revealing fractured surfaces and particle morphology. The sample were sintered at 1300 °C for 24 h and cooled in air and the resulting product was crushed into powder.

The measured density of ~5.60 g/cm$^3$ for B2–NiAl intermetallic alloy in the current work corresponds to those reported in literature as presented in **Table 4.1 [23,38]**. XRD pattern of the as-sintered B2–NiAl lumps and those of the powder after crushing the lumps are

http://etd.uwc.ac.za/

shown in **Fig. 4.12**. The analysis revealed an ordered single phase cubic B2 crystal structure of Pm-3m space group and CsCl superlattice structure with a=2.885 Å. It has been reported that the B2–NiAl intermetallic compound substitutes a single-crystal nickel-base superalloy due to its high melting temperature, low density and high oxidation resistance **[39]**. Accordingly, the B2–NiAl phase forms a protective oxide layer at temperatures above 1200 °C **[40]** but lack strength and toughness at room temperature **[41]**. The B2–NiAl phase exists over a wide concentration range extending across the stoichiometric (1:1) composition. Its unit cell consists of two simple cubic sub-lattices at equiatomic composition. All the Al atoms occupy the cube corners of one sublattice and Ni-atoms occupy the corners of the other sublattice **[42]**. Additionally, the crushed powder retained the B2 crystal structure (**Fig. 4.9a**) with a slightly smaller lattice parameter of a = 2.881 Å. Typically, NiAl reaction follows the sequence; Ni + Al→NiAl3→Ni2Al3→NiAl **[37,43]**. The fragile nature of the sample sintered at 1300 °C for 24 h is attributed mainly to air cooling and minor oxide impurities along the grain boundaries. XRD pattern of the cubic (B2)–NiAl alloy sintered at 750 °C for 120 h and further oxidized at 750 °C for 120 h in air is presented in **Fig. 4.13**. The B2–NiAl crystal structure shows stability after prolonged oxidation retaining a lattice parameter a=2.887 Å (**Fig. 4.13**). B2 NiAl lattice parameters obtained from XRD analysis were compared with the calculated lattice parameters using **Eq. (6)** on the (110) most intense peak and presented in **Table 4.2**.

UNIVERSITY of the WESTERN CAPE

**Table 4.2**: The XRD and calculated lattice parameters of the sintered NiAl at 750 °C for 120 h and their PDF reference codes as well as the measured oxygen content.

| Alloy | XRD Lattice parameter (Å) | Calculated Lattice parameter (Å) | Reference Codes | O content (wt.%) |
|---|---|---|---|---|
| B2–NiAl 24 h (750 °C) | 2.881 | 2.868 | 00-044-1186 | 0.103 ± 0.026 |
| B2–NiAl 48 h (750 °C) | 2.881 | 2.887 | 00-044-1186 | 0.120 ± 0.031 |
| B2–NiAl 120 h (750 °C) | 2.887 | 2.891 | 03-065-0420 | 0.152 ± 0.045 |
| B2–NiAl 24 h (1300 °C) | 2.881 | 2.879 | 00-044-1186 | 0.276 ± 0.027 |
| B2–NiAl (750 °C) oxidized at 750 °C for 120 h | 2.887 | 2.861 | 03-065-0420 | 2.499 ± 0.332 |

http://etd.uwc.ac.za/

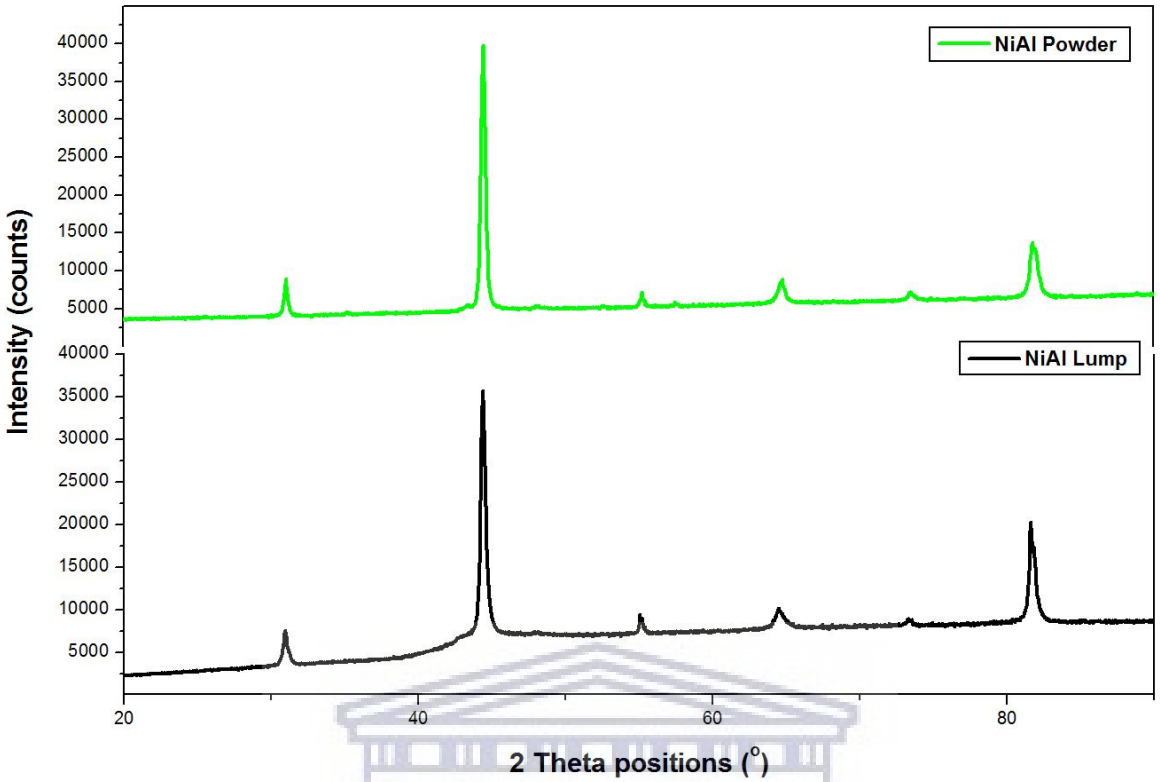


**Figure 4.12**: XRD pattern of the NiAl lump obtained after sintering at 1300 °C for 24 h and that of the lump after crushing into powder.

UNIVERSITY of the WESTERN CAPE

The detected oxide layer was predominantly $Al_2O_3$ on the surface of B2–NiAl alloy having lattice parameters a=4.735 Å; c=12.918 Å. Additionally, a monoclinic phase (a=5.743 Å; c=8.1046 Å) was detected and attributed to a metastable oxynitride which is attributed to N pick-up as confirmed by the EDS analysis in Fig. 13 **[44]**. These lattice parameters are not similar to those of the monoclinic aluminium oxide reported in literature (a=11.810 Å; b=2.90 Å; c=5.610 Å) **[43]**. Minor peaks of the rhombohedral (RHL) phase were also detected.

$$d_{hkl} = \frac{a_o}{\sqrt{(h^2 + k^2 + l^2)}} \quad \text{for BCC NiAl} \qquad (6)$$

where d is the d = spacing of (110) peak while $a_0$ is the lattice parameter. B2–NiAl alloy powder was further exposed at 750 °C in air for 120 h. There is evidence of excessive grain growth after thermal oxidation.

This alloy is resistant to oxidation due to a thin scale of the stable $Al_2O_3$ which forms a protective layer that inhibits further oxidation (**Fig. 4.14**). The presence of Al in NiAl promotes selective oxidation of Al during formation of an $Al_2O_3$ layer with no evidence of any Ni oxide **[44]**.

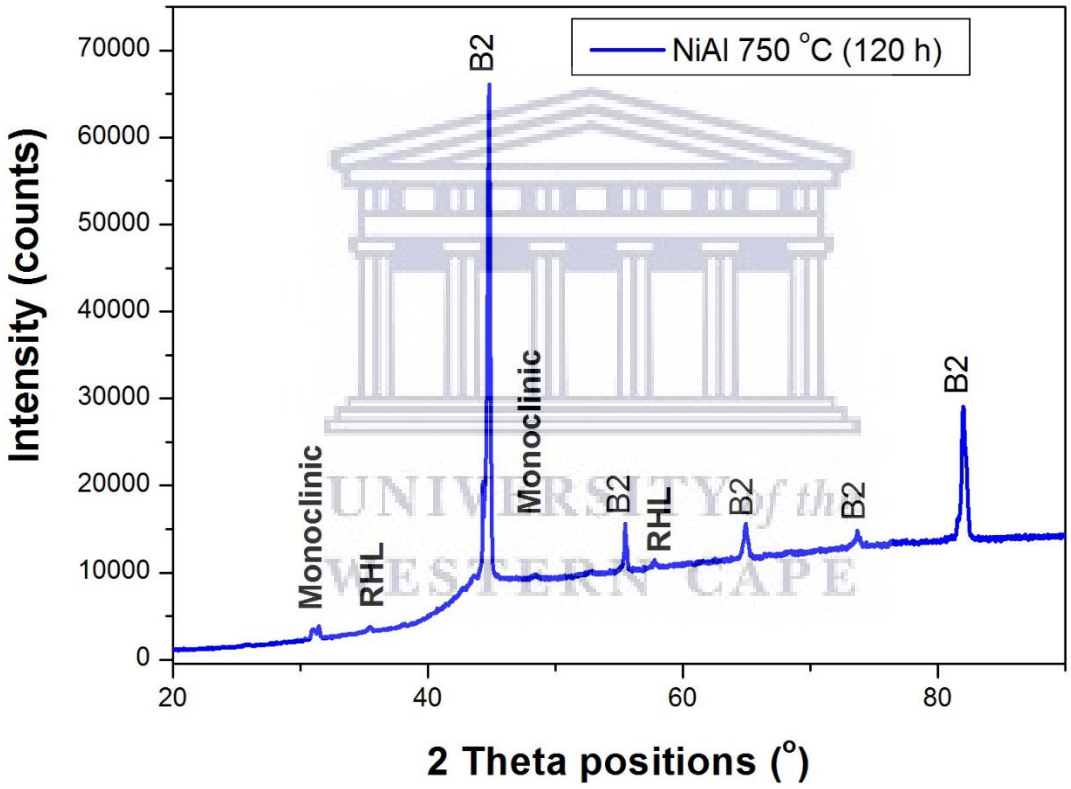


**Figure 4.13**: XRD pattern of the NiAl sample sintered at 750 °C for 120 h and further oxidized in air at 750 °C for 120 h.

Diffusion processes through the oxide layer is the rate determining factor for any further oxidation of the alloy and its kinetics can be described by the parabolic rate of a law of diffusion-controlled oxidation in **Eq. (7)**:

http://etd.uwc.ac.za/

$(\Delta m/A^2)=kp.t$ (7)

Whereby (Δm/A) is the weight gain per unit area, kp is the parabolic rate constant depending on oxidation temperature and is calculated from the slopes of the $(\Delta m/A)^2$ versus treatment time graphs and t is time **[44]**. The relationship between parabolic rate constant kp and temperature T can be expressed by an Arrhenius-type **Eq. (8)**:

$$D = D_0 exp\left(\frac{-Q}{RT}\right) \quad (8)$$

$D_0$ is a constant, Q is an activation energy (J/mol) for oxide formation, R is gas constant (8.314 J/mol.K) and T is absolute temperature (K). In the current experiment, negligible mass loss of 0.0002 g (0.02%) after 120 h at 750 °C on the sample was recorded.

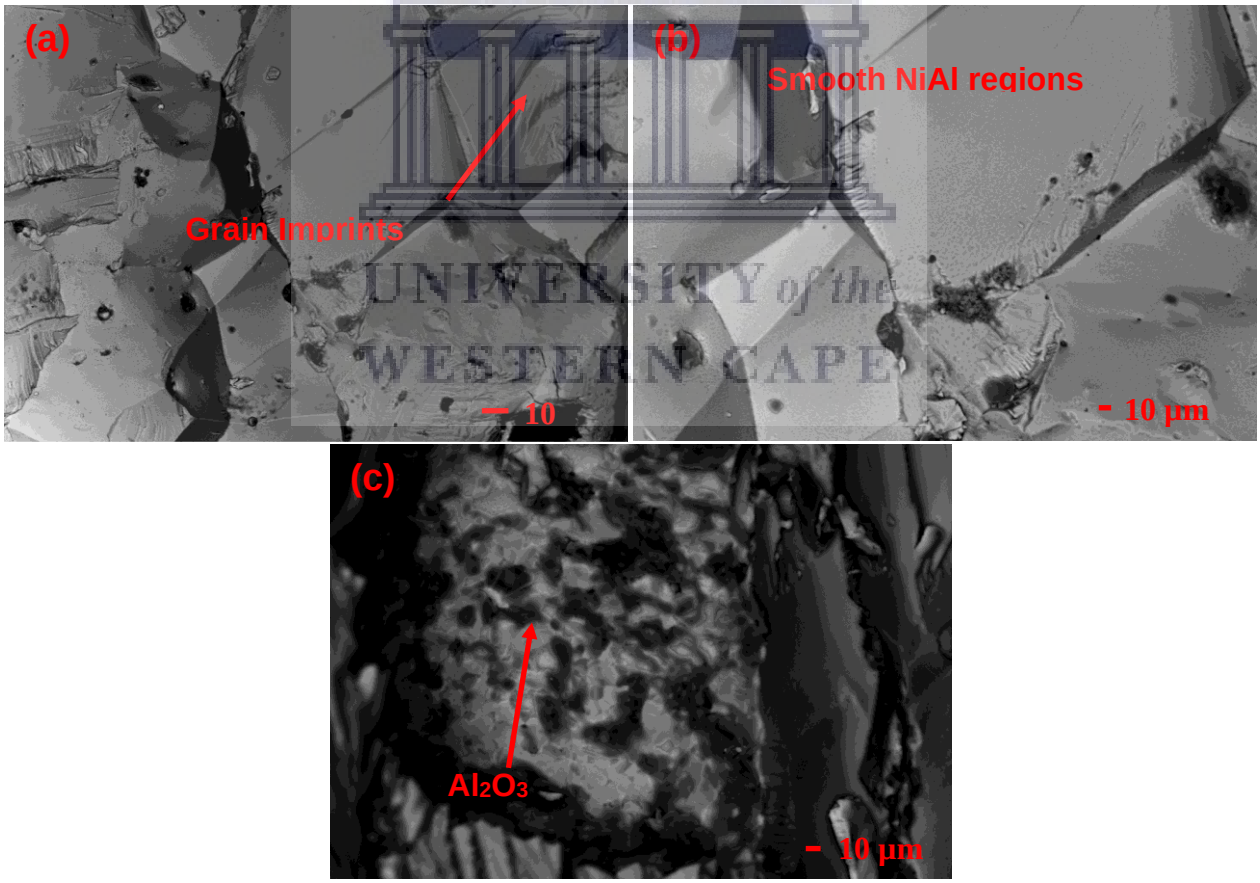


**Figure 4.14**: SEM images of the β-NiAl alloy sintered at 750 °C for 120 h and further oxidized in air at 750 °C for 120 h.

UNIVERSITY of the WESTERN CAPE

A spallation of the oxide layer was observed as shown in **Fig. 4.14c**. The underlying B2–NiAl alloy exposed by the oxide scale spallation shows a mixture of grain imprints and smooth regions resembling spallation behaviour **[43, 45]**. Zhang et al. **[46]**, emphasized the dependence of the epitaxial relationship between NiAl and γ-$Al_2O_3$ and surface roughness on the oxidation temperature. Additionally, there is lattice mismatch-induced strain energy during oxide growth between the γ-$Al_2O_3$ and the NiAl parent metal which promotes spallation of the oxide later. Elemental distribution is shown by the EDS mapping of the B2–NiAl oxidized alloy in **Fig. 4.15**. The nitrogen attributed to the stabilization of the metastable monoclinic oxynitride phase was detected. In general, NiAl intermetallic alloy shows good resistance to cyclic oxidation.

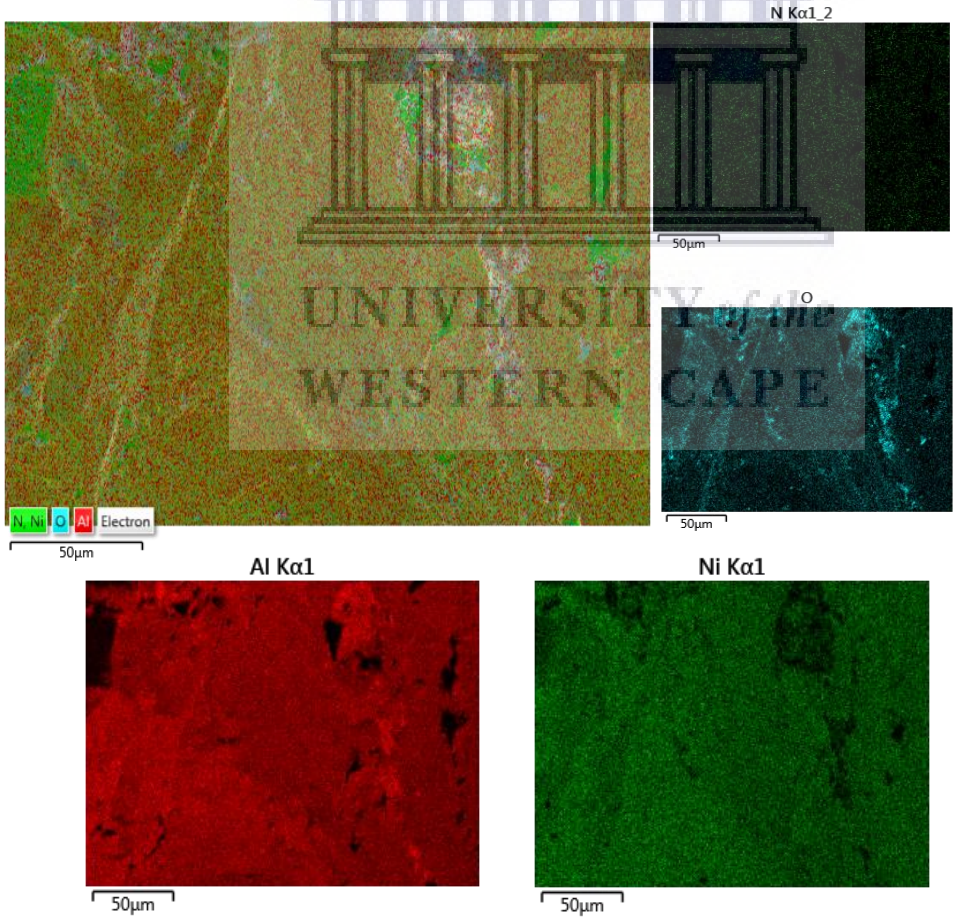


**Figure 4.15**: EDS mapping of the β-NiAl alloy powder after oxidation in air at 750 °C for 120 h.

UNIVERSITY of the WESTERN CAPE

## 4.4 Conclusion

A single phase cubic B2–NiAl alloy was synthesized through mixing of elemental Ni and Al powders followed by cold compacting and sintering. Microstructure of the sintered samples at 750 °C for 24, 48 and 120 h revealed equiaxed grain structure. The 750 °C for 24, 48 and 120 h process achieved well-sintered intermetallic alloys. Sintering of the Ni50 atm. %Al at 1300 °C yielded brittle B2 NiAl lumps that were easily crushable into powder form. Morphology of the brittle powder resembled core-shell growth properties. XRD analysis detected a single cubic B2–NiAl intermetallic phase with comparable lattice parameters for both sintering temperatures of at 750 and 1300 °C. EBSD results demonstrated that the microstructural grains in B2–NiAl alloy sintered at 48 and 120 h were recrystallized and consumed by preferential growth of grains in the <111> orientations, with prolonged annealing times. The density measured for the samples averaged at ~5.60 g/cm$^3$. The B2–NiAl intermetallic developed a thin scale of stable $Al_2O_3$ alloy due to oxidation in air at 750 °C for 120 h. As a result, further oxidation on the sample's surface was restricted, except the traces of $Al_2O_3$ that formed via intergranular oxidation and transformed into a metastable monoclinic oxynitride phase due N contamination.

UNIVERSITY of the
WESTERN CAPE

## References

4.1 L. Fang, S.F. Zhang, F. Xi, R.H. Yang, K. Mukai, Measurement and analysis of liquid density of Ni–Al binary alloys, J. Alloy. Compd. 493 (2010) 465–470.

4.2 E. Sugiarti, F. Destyorini, K.A. Zaini, Y. Wang, N. Hashimoto, S. Ohnuki, S. Hayashi, Characterization of Ni-based coatings on carbon steel by electron microscopy, Surf. Coat. Technol. 265 (2015) 68–77.

4.3 D.B. Miracle, Overview No. 104: The physical and mechanical properties of NiAl, Acta Mater. 41 (1993) 649–684.

http://etd.uwc.ac.za/

4.4 Z.D. Xiang, S.R. Rose, P.K. Datta, Low-temperature formation and oxidation resistance of nickel aluminide/nickel hybrid coatings on alloy steels, Scr. Mater. 59 (2008) 99–102.

4.5 C.M. Bao, U. Dahlborg, N. Adkins, M. Calvo-Dahlborg, Structural characterisation of Al–Ni powders produced by gas atomisation, J. Alloy. Compd. 481 (2009) 199-206.

4.6 D.J. Jarvis, D. Voss, IMPRESS Integrated Project—An overview paper, Mater. Sci. Eng. A 413 (2005) 583-591.

4.7 J. Guo, Z. Wang, L. Sheng, L. Zhou, C. Yuan, Z. Chen, L. Song, Wear properties of NiAl based materials, Prog. Nat. Sci: Mater. Int. 22 (5) (2012) 414–425.

4.8 M. Beyhaghi, J. V. Khaki, M. Manawan, A. Kiani-Rashid, M. Kashefi, S. Jonsson, In-situ synthesis and characterization of nano-structured NiAl-Al2O3 composite during high energy ball milling, Pow. Technol. 329 (2018) 95–106.

4.9 W.R. Osório, L.C. Peixoto, M.V. Canté, A. Garcia, Microstructure features affecting mechanical properties and corrosion behaviour of a hypoeutectic Al–Ni alloy, Mater. Des. 31 (2010) 4485–4489.

4.10 J.L. Cheng, H.H. Hng, H.Y. Ng, P.C. Soon, Y.W. Lee, Deposition of nickel nanoparticles onto aluminum powders using a modified polyol process, Mater. Res. Bull. 44 (2009) 95-99.

4.11 Z. Halem, N. Halem, M. Abrudeanu, S. Chekroude, C. Petot, G. Petot-Ervas, Transport properties of Al or Cr-doped nickel oxide relevant to the thermal oxidation of dilute Ni-Al and Ni-Cr alloys, Solid State Ion. 297 (2016) 13-19.

4.12 U. Rayhan, J.H. Do, T. Arimura, T. Yamato, Reduction of carbonyl compounds by Raney Ni-Al alloy and Al powder in the presence of noble metal catalysts in water, Comp. Rendus Chim. 18 (2015) 685-692.

4.13 Y. Xu, S. Kameoka, K. Kishida, M. Demura, A. Tsai, T. Hirano, Catalytic properties of Ni3Al intermetallic for methanol decomposition, Mater. Trans. 45

UNIVERSITY of the WESTERN CAPE

(2004) 3177-3179.

4.14 M.C. Dumez, R.M. Marin-Ayral, J.C. Tédenac, The role of experimental parameters in combustion synthesis of NiAl under high gas pressure, J. Alloy. Compd. 268 (1998) 141–151.

4.15 J.P. Lebrat, A. Varma, Self-propagating high-temperature synthesis of Ni3Al, Combust. Sci. Technol. 88 (1993) 211–222.

4.16 L. Plazanet, F. Nardou, Reaction process during relative sintering of NiAl, J. Mater. Sci. 33 (1998) 2129–2136.

4.17 P. Swaminathan, M.D. Grapes, K. Woll , S.C. Barron , D.A. Lavan , T.P. Weihs, Studying exothermic reactions in the Ni–Al system at rapid heating rates using a nanocalorimeter, J. Appl. Phys. 113 (2013) 143509.

4.18 M.H. Enayati, F. Karimzadeh, S.Z. Anvari, Synthesis of nanocrystalline NiAl by mechanical alloying, J. Mater. Proc. Technol. 200 (2008) 312–315.

4.19 S. Garćıa-Galán, G. Arámburo-Pérez, C. González-Rivera, J. Juárez-Islas, The effect of Cu-macroalloying on β-NiAl intermetallic compound obtained by mechanical alloying, J. Mater. Proc. Technol. 143–144 (2003) 551–554.

4.20 A. Mashreghi, M.M. Moshksar, Partial martensitic transformation of nanocrystalline NiAl intermetallic during mechanical alloying, J. Alloy. Compd. 482 (2009) 196–198.

4.21 A. Abraham, H. Nie, M. Schoenitz, A.B. Vorozhtsov, M. Lerner, A. Pervikov, N. Rodkevich, E.L. Dreizin, Bimetal Al–Ni nano-powders for energetic formulations, Combust. Flame 173 (2016) 179–186.

4.22 P. Zhu, J.C.M. Li, C.T. Liu, Reaction mechanism of combustion synthesis of NiAl, Mater. Sci. Eng. A 329-331 (2002) 57–68

4.23 O. Ozdemir, S. Zeytin, C. Bindal, A study on NiAl produced by pressure-assisted combustion synthesis, Vacuum 84 (2010) 430–437.

UNIVERSITY of the WESTERN CAPE

4.24 H.X. Dong, Y.H. He, J. Zou, N.P. Xu, B.Y. Huang, C.T. Liu, Effect of preheating treatment at 575 ◦C of green compacts on porous NiAl, J. Alloy. Compd. 492 (2010) 219–225.

4.25 V. Yu. Filimonov, K. B. Koshelev, A. A. Sytnikov, Thermal modes of heterogeneous exothermic reactions. Solid-phase interaction, Combust. Flame 185 (2017) 93–104.

4.26 M.L. Weaver, M.J. Kaufman, R.D. Noebe, The effects of alloy purity on the mechanical behavior of soft oriented NiAl single crystals, Scripta Metallurg. Mater. 29, (8) (1993) 1113-1118.

4.27 M. N. Mathabathe, A. S. Bolokang, G. Govender, R. J. Mostert, C. W. Siyasiya, Structure-property orientation relationship of a gamma/alpha2/Ti5Si3 in as-cast Ti-45Al-2Nb-0.7Cr-0.3Si intermetallic alloy, J. Alloy. Compd. 765 (2018) 690–699.

4.28 D. Stojakovic, Electron backscatter diffraction in materials characterization, Proc. Appl. Ceram. 6 (1) (2012) 1-13.

4.29 AS Bolokang, M.J. Phasha, Effect of mechanical milling and cold pressing on Co powder, J. Metallurgy. 2012 (2012) 1-7.

4.30 T. Chen, J.M. Hampikian, N.N. Thadhani, Synthesis and characterization of mechanically alloyed and shock-consolidated nanocrystalline NiAl intermetallic. Acta Mater. 47 (8) (1999) 2567-2579.

4.31 Kamil Bochenek, Witold Węglewski, Jerzy Morgiel, Michał Basista, Influence of rhenium addition on microstructure, mechanical properties and oxidation resistance of NiAl obtained by powder metallurgy, Mater. Sci. Eng. A 735 (2018) 121–130.

4.32 K.E. Harris, F. Ebrahimi, H. Garmestani, Texture evolution in NiAl, Mater. Sci. Eng. A 247 (1998) 187–194.

4.33 F. Ebrahimi, T. G. Hoyle, brittle-to-ductile transition in polycrystalline NiAl, Acta mater. 45 (10) (1997) 4193-4204.

UNIVERSITY of the WESTERN CAPE

4.34 AS Bolokang, M.J. Phasha, Thermal analysis on the curie temperature of nanocrystalline Ni powder produced by ball milling, Adv. Pow. Metallurg. 22 (2011) 518-521.

4.35 A. Slager, D. Kesse, A family of Ductile Intermetallic Compounds, Nat. Mater. 2 (2003) 587-591. S. An, J. Li, Y. Li, S. Li, Q. Wang, B. Liu, Two-step crystal growth mechanism during crystallization of an undercooled Ni50Al50 alloy, Scientific Reports | 6:31062 | DOI: 10.1038/srep31062.

4.36 O. Ozdemir, S. Zeytin, C. Bindal, Characterization of NiAl with cobalt produced by combustion synthesis, J. Alloy. Compd. 508 (2010) 216–221.

4.37 Q. Wu, S. Li, Y. Ma, S. Gong, Study on behavior of NiAl coating with different Ni/Al ratios, Vacuum 93 (2013) 37–44.

4.38 M. Adabi, A.A. Amadeh, Electrodeposition mechanism of Ni-Al composite coating, Trans. Non Ferr. Met. Soc. China 24 (2014) 3189–3195.

4.39 X. Yang, X. Peng, F. Wang, Effect of annealing treatment on the oxidation of an electrodeposited alumina-forming Ni–Al nanocomposite, Corros. Sci. 50 (2008) 3227–3232.

4.40 A. Paul, A.A. Kodentsov, F.J.J. van Loo, On diffusion in the β-NiAl phase, J. Alloy. Compd. 403 (2005) 147–153.

4.41 I. Levin, L.A. Bendersky, D.G. Brandon, M. Ruhle, Cubic to monoclinic phase transformation in alumina, Acta mater. 45 (9) (1997) 3659-3669.

4.42 A.S. Bolokang, D.E. Motaung, C.J. Arendse, T.F.G. Muller, Morphology and structural development of reduced anatase-$TiO_2$ by pure Ti powder upon annealing and nitridation: Synthesis of $TiO_x$ and $TiO_xN_y$ powders, Mater. Char. 100 (2015) 41–49.

4.43 C. Kaplin, R. Ivanov, M. Paliwal, I-H. Jung, M. Brochu, The effect of nanostructure on the oxidation of NiAl, Intermetallics 54 (2014) 209-217.

4.44 H.J. Grabke, Oxidation of NiAl and FeAl, Intermetallics 7 (1999) 1153–1158.

UNIVERSITY of the WESTERN CAPE

4.45 Z. Zhang, L. Li, J.C. Yang, γ-$Al_2O_3$ thin film formation via oxidation of β-NiAl (110), Acta Mater. 59 (2011) 5905–5916.

UNIVERSITY of the
WESTERN CAPE

http://etd.uwc.ac.za/

# CHAPTER FIVE

## Characterization of the $Ni_{62.5}Al_{37.5}TiC_{1.28}$ composite produced via cold pressing and sintering process

*Paper submitted for peer review*


### Abstract

The $Ni_{62.5}Al_{37.5}TiC_{1.28}$ composite was developed by powder mixing, compaction and sintering at 650 ºC**.** The chemical reaction during sintering showed that self-propagating high-temperature synthesis (SHS) occurs when a small amount of nanosized (50 – 100 nm) TiC powder was added. The effect of cold pressing on the low temperature TE is proposed. Martensite NiAl laths, $Ni_3Al$ and TiC phases were formed.


**Keywords:** Martensite; Thermal explosion; TiC; NiAl; cold pressing

UNIVERSITY of the WESTERN CAPE

### 5.1 Introduction

The Nickel aluminide (NiAl) alloys are interesting systems with melting temperature of 1640 ºC and contains the ordered B2 intermetallic NiAl with unique physical and mechanical properties for high temperature applications **[1]**. However, there is a need to improve its low temperature strength which limits the alloy application. The Ni-Al system reveals a range of phases depending on the starting chemical composition. These phases include the high-temperature $Al_3Ni$ eutectic used in production of aerospace gas turbine engine blades, hence it is considered an attractive structural material for high-temperature applications **[2]**. In particular, the Al45 at. %Ni was formed via explosion of electrically heated twisted pure Al and Ni wires in an argon atmosphere **[3]**. Operating temperatures as low as 575 °C–750 °C were effective to synthesize porous NiAl intermetallic alloy due

to exothermic reaction **[4]**. Thermal explosion (TE) and ignition of various Ni-Al powder blends, rolled and magnetron sputtered films, compacts of mechanically activated and non-activated mixtures were explored under mechanical activation. A single cubic B2–NiAl phase was synthesized through mixing of elemental Ni and Al powders followed by cold compacting and sintering **[5]**. Cubic B2–NiAl alloy was synthesized after sintering of the cold pressed compacts at 750 °C and 1300 °C, respectively. The compacts sintered at 1300 °C were brittle while those sintered at 750 °C sintered were not as brittle. The TE process of stoichiometric Ni–Al system was investigated by time-resolved X-ray diffraction techniques to trace the dynamics of phase transformation during rapid, gasless heterogeneous reactions **[6]**. Authors compared the TE of un-milled and mechanically milled NiAl and concluded that the former occur due to melting, while the latter is by solid state reaction. This behaviour implies that deformations create fresh surfaces for a solid-state reaction to occur between Ni and Al particles during mechanical milling. The mechanical activation leads to a decrease in activation barrier while the ignition becomes possible at low temperatures below the melting point of Al **[7]**. In this work, the effect of nanosized TiC powder on the microstructure of (Ni-37.5at%Al)-1.28vol%TiC composite was investigated. Nickel is a strategic metal for both ferromagnetic and non-magnetic shape memory alloys (SMAs) **[8-11]**. Despite limited investigations on this metal properties linked to SMAs, it has been shown to exhibit second-order phase transition (ferromagnetic to paramagnetic) when heated to high temperatures **[12, 13]**. This phase transition is affected by mechanical deformations **[14, 15]**. The formation of martensite laths reinforced with small amount of nanosized TiC reported in this paper has not been previously encountered by the authors. Moreover, it is proposed that surface mechanical deformation induced by cold pressing triggers the thermal explosion at lower temperatures.

UNIVERSITY of the
WESTERN CAPE

## 5.2 Experimental Work

Elemental Ni (99.8%), Al (99.9%) and nanoparticles of TiC powders were blended to synthesize a TiC reinforced NiAl. A NiAl with Ni-37.5at%Al was initially mixed followed by addition of 1.28 Vol.% TiC of the total TiC-NiAl mixture. The powder mixture was cold-pressed into cylindrical (17mm diameter) coupons at 20 MPa and sintered at 650 ºC in a Carbolite tube furnace with flowing argon (Ar) for 6 hours (h). The resulting composite is losely refered to as $Ni_{62.5}Al_{37.5}TiC_{1.28}$. The morphology of the Ni, Al and TiC powdersas well as the microstructure of the sintered and polished NiAlTiC composite were investigated using a high-resolution scanning electron microscope (HR-SEM, Auriga ZEISS) coupled with a Robinson Backscatter Electron Detector and an Oxford Link Pentafet energy dispersive x-ray spectroscopy (EDS) detector. MicroVickers hardness tests were performed by applying a load of 300 Kgf and dwelling time of 10s. Hardness was measured across the polished surface specimens at 0.2mm intervals and an average of 32 measurements computed per distance from the surface.

UNIVERSITY of the
WESTERN CAPE

## 5.3 Results and Discussion

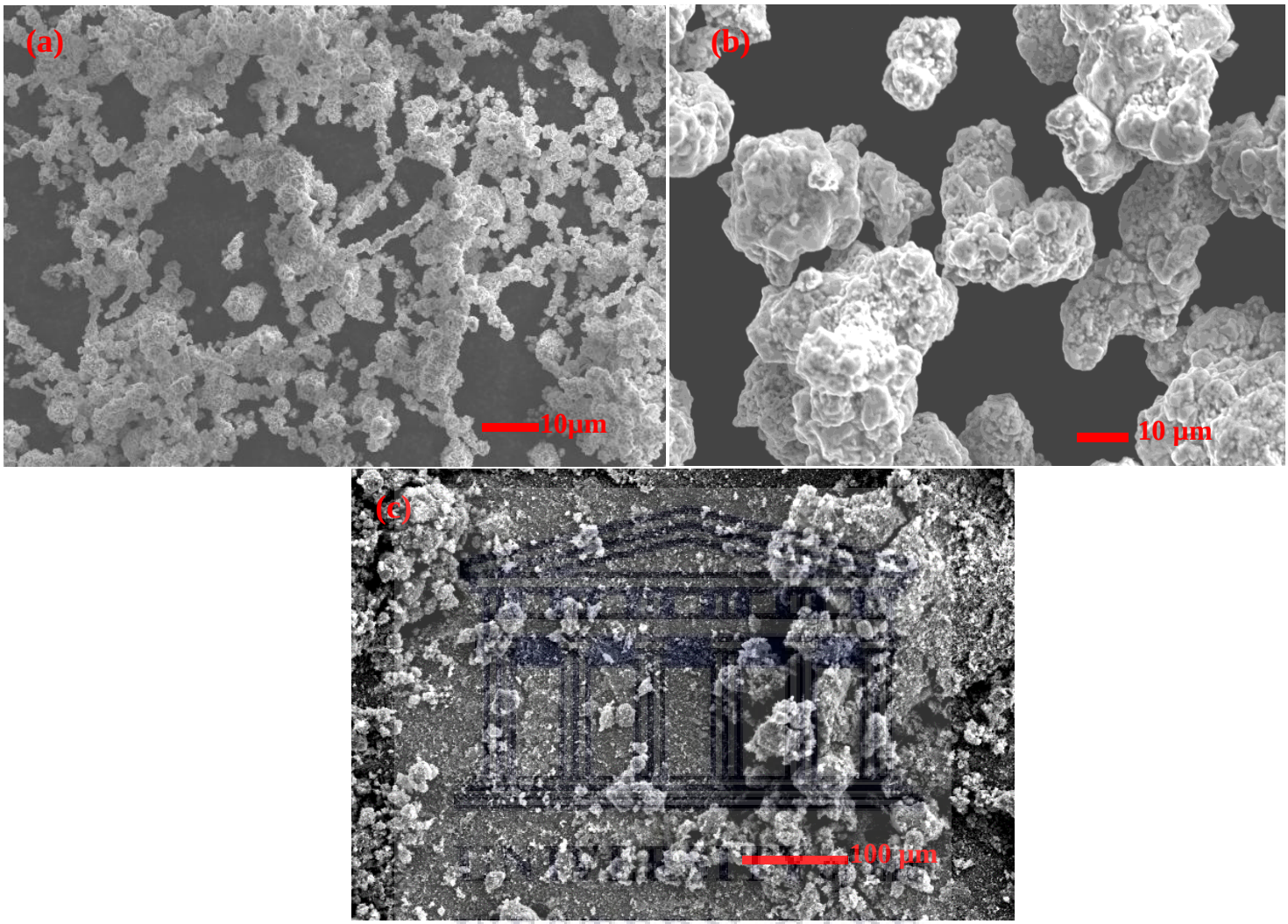


WESTERN CAPE

**Figure 5.1**: SEM images of the (a) Ni, (b) Al and (c) TiC powders.

The SEM images of the raw materials, Ni, Al and TiC powders are shown in **Fig. 5.1**. Ni powder comprises chains of ultrafine, spherical particles (~2 µm) revealing the agglomeration **(Fig. 5.1a)**. Similarly, the Al powder in **Fig. 5.1b** reveals large agglomerated particles ~40 µm in size. The fine agglomerated TiC powder is shown in **Fig. 5.1c**. Due to the low yield strength of the Al than Ni and TiC particles, it acts as a binder during compaction process forming stable compacts after cold pressing as illustrated in **Fig. 5.2a**. Cold compaction is a critical initial step of particle interaction between Ni and Al particles since the inter-particle contact makes the thermal reaction

http://etd.uwc.ac.za/

and ignition of the aggressive exothermic reaction evident in **Fig. 5.2a**. The thermodynamic reactions 1 and 2, respectively occur below the melting temperature of pure Al (660 ºC), hence the sintering process was performed at 650 ºC.

$$Ni + 3Al \rightarrow NiAl_3 \quad (1)$$

$$1/3Ni_2Al_3 + 1/3Ni \rightarrow NiAl \quad (2)$$

However, although the melting temperature of Ni is 1453 ºC, Ni undergoes the second-order phase transformation at ~356 ºC (Curie point) becoming paramagnetic **[12,13]**. This transition temperature can be affected by deformation of the powder particles. The deformation induced on the particles surfaces after cold pressing contributes to the ignition temperature occurring below the melting temperature of Al **[4, 14]**, also leading to a decrease in the activation barrier **[16]. Fig. 5.2b, c** reveals the thermal analysis of the cold pressed and free flowing Al powders. It is evident that the cold-pressed sample melted ~10 ºC lower than the free-flowing powder. This behaviour agree with our proposed mechanism on the effect of cold pressing on the ignition temperature of NiAl compacts during sintering. As a result, the occurrence of TE is justified by the broken crucible during sintering. All the samples were found attached to the bottom of the one piece of the broken crucible indicative of the expansion of the compacts during sintering.

UNIVERSITY of the WESTERN CAPE

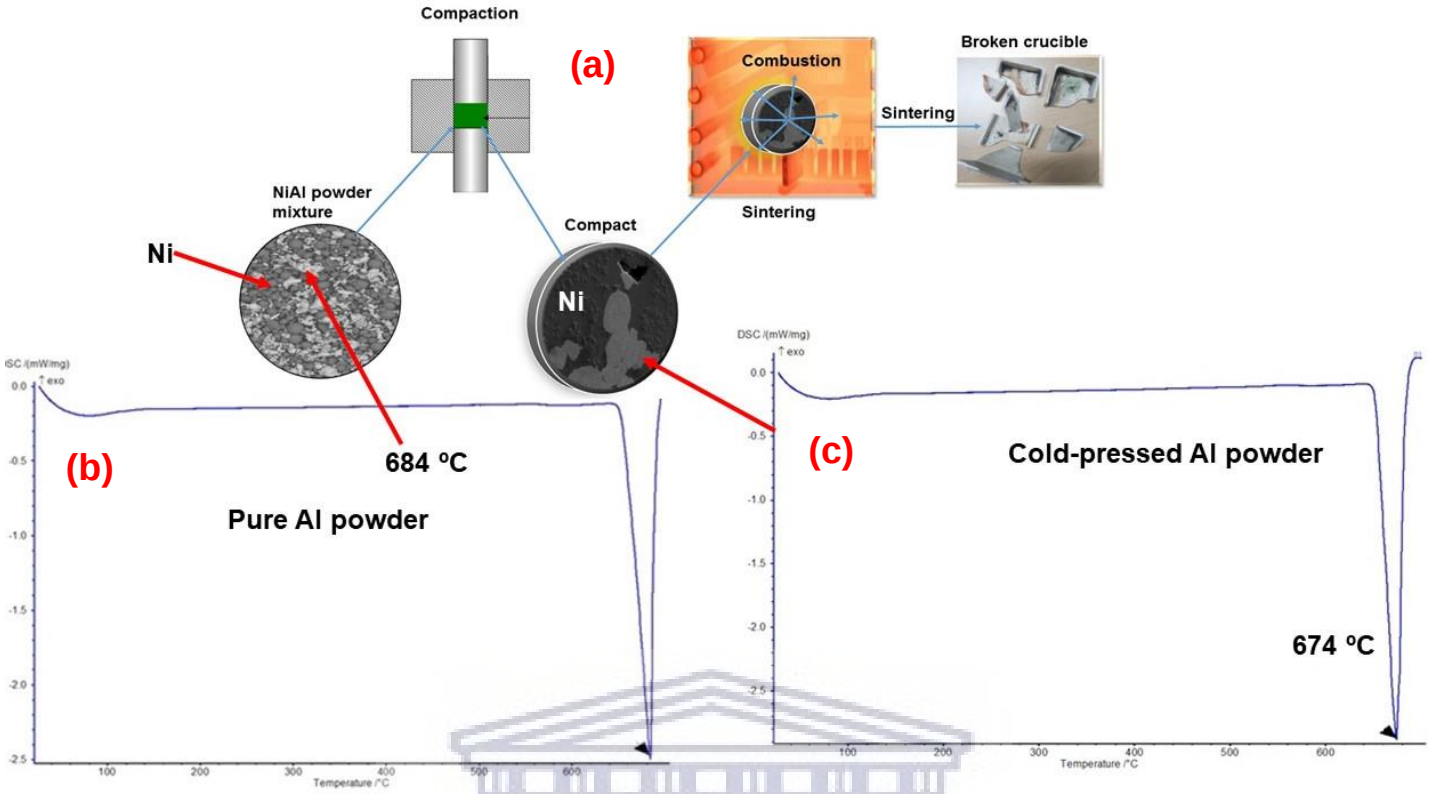


**Figure 5.2**: Schematic representation of the synthesis and thermal explosion of $Ni_{62.5}Al_{37.5}TiC_{1.28}$ composition during sintering.

**Fig. 5.3a-d** shows the SEM images of the $Ni_{62.5}Al_{37.5}TiC_{1.28}$ composite sintered at 650 ºC. The exothermic reaction accompanied by the TE during sintering is attributed to the alloy formation. **Fig. 5.3a** shows the resulting microstructure revealing all phases present after sintering. Of interest in this study, the fine martensite Ni-Al laths formed shown in **Fig. 5.3c**. The martensite plates are a ductile structure surrounded by the eutectic-type $Ni_3Al$ structure and hard TiC phase. $Ni_3Al$ phase shows the martensite plates by rapid cooling of bcc B2 phase transforming to fct ($L_{10}$) **[17]**. In the current study, the samples were furnace cooled. The TiC grains **(Fig. 5.3b, d)** are exposed as sharp edged and faceted structure. This $Ni_{62.5}Al_{37.5}TiC_{1.28}$ composite resist cutting by the diamond-cutting tool which is an indication of work hardening behaviour. The TiC particles embedded inside the $Ni_3Al$ intermetallic phase inhibits deformation of grains comprised of martensite plates and induces the balance between strength and ductility. Therefore, reinforcement of the

UNIVERSITY of the WESTERN CAPE

$Ni_{62.5}Al_{37.5}$ intermetallic alloy by nanosized TiC particles of 1.28 Vol.% composition is effective in strengthening the composite. The microstructures in **Fig. 5.3b** expose interfacial microsized pores.

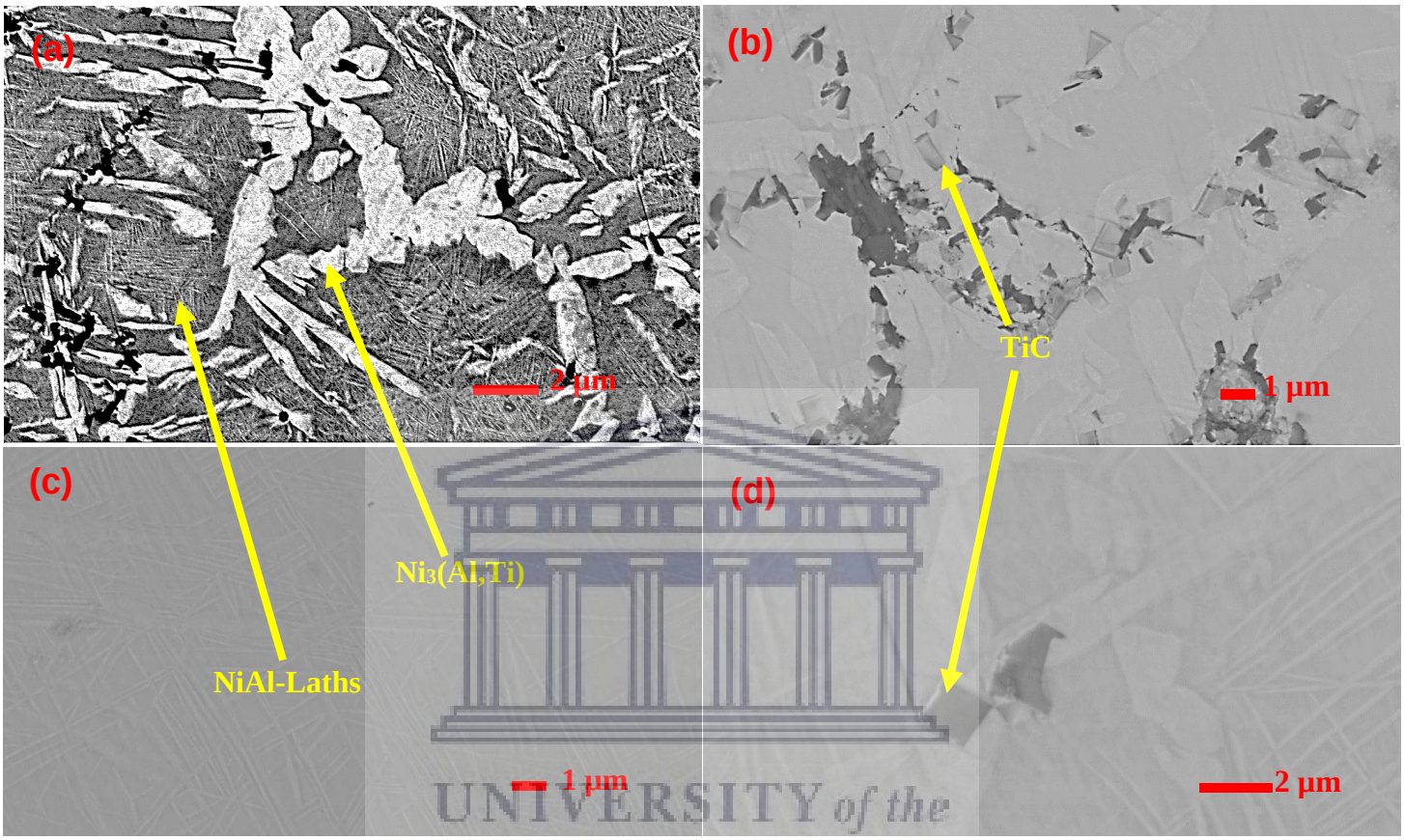


UNIVERSITY of the
WESTERN CAPE

**Figure 5.3**: SEM images of the 650 ºC-sintered $Ni_{62.5}Al_{37.5}TiC_{1.28}$

The EDS elemental mapping confirms the phases present in the sintered alloy as shown in **Fig. 5.4**. The Ni and Al phases form the matrix where martensite plates are located. TiC are widely distributed within the $Ni_3Al$ eutectic phase with small amounts of Ti. Evidence of Si contamination is due to the SiC contamination during polishing.

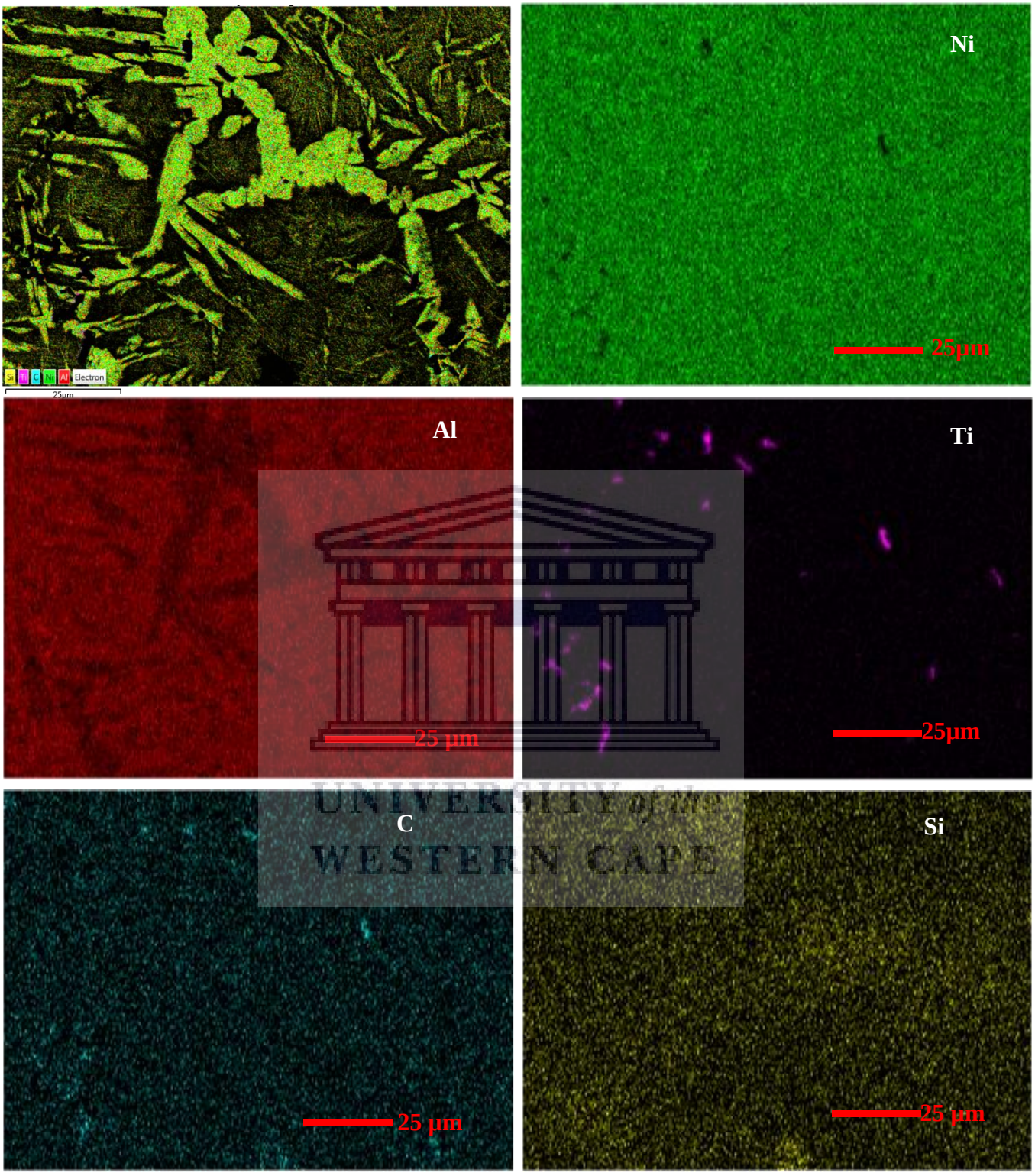


**Figure 5.4**: SEM-EDS elemental mapping of the 650 ºC-sintered $Ni_{62.5}Al_{37.5}TiC_{1.28}$ composite

UNIVERSITY of the WESTERN CAPE

$Ni_{62.5}Al_{37.5}$ is a Ni-rich composition on the Ni-Al phase diagram as represented in **Fig. 5.5b**. Due to addition of TiC particles that impeded diffusion in the microstructure, martensite structure was formed, as evident in **Fig. 5.5a**. The $Ni_{62.5}Al_{37.5}TiC_{1.28}$ composite resisting the cutting by the diamond cutting tool is an indication of the work hardening effect. This behaviour is like those shown by the Fe-Mn steels strengthening mechanism **[16]** due to intergranular brittle $Ni_3Al$ and TiC precipitates **[18, 19]**. The martensite phase has developed due to thermally activated dislocation motion by the movement of atoms over distances that are less than the inter-atomic spacing **[20]**. Mostly, the Ni-Al martensite laths are exposed after water quenching (WQ) due to residual stress **[21]**. The WQ promotes the $Ni_3Al$ precipitation at grain boundaries. Filho et al. **[22]** reported the twinning and multiple dislocations dictating the strain hardening mechanisms in austenite, which in the current study was induced by TiC nanoparticles during the thermal explosion. The TiC particles and the $Ni_3(Al,Ti)$ phase have enclosed the martensite laths restricting further deformation, hence making it difficult to cut the material. The precipitation of the faceted TiC and $Ni_3(Al,Ti)$ particles is in agreement with literature **[23]**.

UNIVERSITY of the
WESTERN CAPE

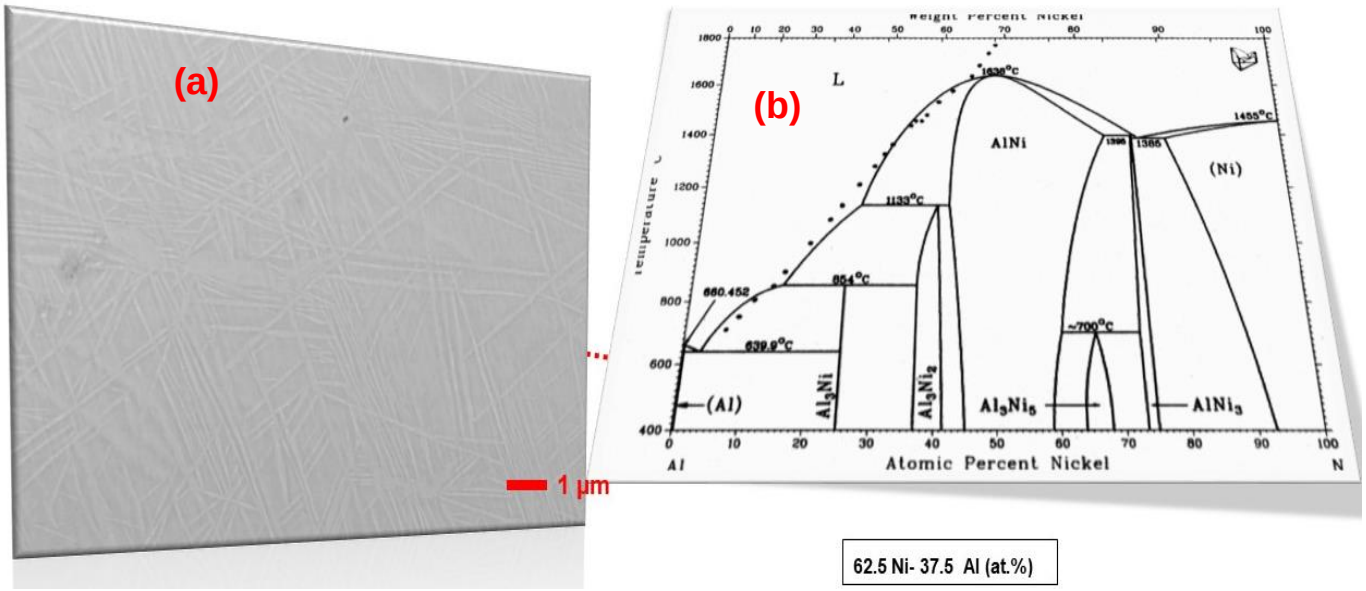


**Figure 5.5**: Formation mechanism of the $Ni_{62.5}Al_{37.5}TiC$ composite

**Fig. 5.6** shows the microhardness of the carbide free $Ni_{62.5}Al_{37.5}$ and $Ni_{62.5}Al_{37.5}TiC_{1.28}$ composite respectively. Addition of 1.28 Vol.% increased the hardness of the composite notably. All samples were sintered at 650 ºC for 6 hours. The $Ni_{62.5}Al_{37.5}TiC_{1.28}$ composite has an average hardness of 431 HV while the $Ni_{62.5}Al_{37.5}$ intermetallic alloy measured 396 HV. The hard $Al_3Ni$ intermetallic phase is less brittle compared to carbides. The Hall-Petch relationship shows that the hardness of the composite is dependant on the grain size according to Eq. (3) but also by the chemical composition and the interfacial pores present at interfaces **[24]**. The current hardness values were compared with some of the literature presented in **Table 4.1**. The $Ni_3Al$ phase is harder in comparison to the NiAl phase. It is evident that the hardness of TiC reinforced NiAl composite depends on the composition of the matrix as well as the TiC content **[25-27]**.

$$Hv = H_O + kD^{-1/2} \quad (3)$$

UNIVERSITY of the WESTERN CAPE

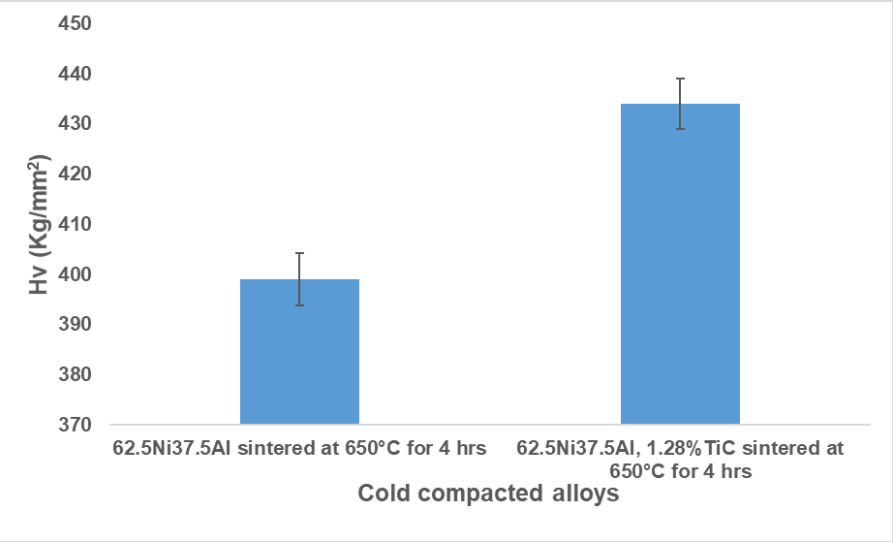


**Figure 5.6**: Microhardness of the $Ni_{62.5}Al_{37.5}$ and $Ni_{62.5}Al_{37.5}TiC_{1.28}$ composite.

**Table 5.1**: Hardness of the $Ni_{62.5}Al_{37.5}TiC_{1.28}$ composite compared with literature data.

| Alloy | Process | Hardness (HV) | Ref |
|---|---|---|---|
| NiAl | BM-vacuum hot pressing | 360±19 | **[19]** |
| $TiB_2$-NiAl | Vacuum arc melting | 670 | **[25]** |
| | As-cast | 55 | |
| | Heat treated | 361 | |
| NiAl | Cold Isostatic pressing | 244.7 | **[26]** |
| NiAl-86 vol.%TiC | | 1428 | **[26]** |
| Ni–25 at.%Al (Ni3Al) | vacuum arc melting furnace | 307±10 HV0.1 | **[27]** |
| Ni–25 at.%Al–7 wt.%TiC | vacuum arc melting furnace | 449±10 | **[27]** |
| Ni–25 at.%Al–10 wt.%TiC | vacuum arc melting furnace | 435±12 | **[27]** |
| NiAl | | 320 ± 19 | **[5]** |
| $Ni_3Al$ | Cold pressed and sintered 650 ºC | 396 ±14 | Current |
| $Ni_{62.5}Al_{37.5}TiC_{1.28}$ | Cold pressed and sintered 650 ºC | 431±11 | Current |

UNIVERSITY of the WESTERN CAPE

## 5.4 Conclusion

The $Ni_{62.5}Al_{37.5}TiC_{1.28}$ composite was developed by mixing of elemental Ni, Al and TiC, compaction and sintering at 650 ºC**.** The chemical reaction during sintering, showed that self-propagating high-temperature synthesis (SHS) occured during the synthesis of the composite. The cold pressing process reduced the activation/ignition temperature of the surface Ni/Al particle interaction, which propagated to the core of the compact. The resultant microstructure revealed martensitic NiAl plates surrounded by the hard $Ni_3Al$ and TiC particles. The formed composite resisted the diamond tool cutting attributable to the work hardening behaviour of the composite. The average hardness measured for the $Ni_{62.5}Al_{37.5}TiC_{1.28}$ composite was 431±11 HV whereas that of the $Ni_{62.5}Al_{37.5}TiC$ wass 396 ±14 HV.

## References

UNIVERSITY of the
WESTERN CAPE

5.1 O. Ozdemir, S. Zeytin, C. Bindal, Characterization of NiAl with cobalt produced by combustion synthesis, J. Alloys Compd. 508 (2010) 216–221.

5.2 K. Bochenek, M. Basista, Advances in processing of NiAl intermetallic alloys and composites for high temperature aerospace applications, Prog. Aero. Sci. 79 (2015)136–146.

5.3 A. Abraham, H. Nie, M. Schoenitz, A.B. Vorozhtsov, M. Lerner, A. Pervikov, N. Rodkevich, E.L. Dreizin, Bimetal Al–Ni nano-powders for energetic formulations Combust. Flame 173 (2016) 179–186.

http://etd.uwc.ac.za/

5.4 H.X. Dong, Y.H. He, J. Zou, N.P. Xu, B.Y. Huang, C.T. Liu, Effect of preheating treatment at 575°C of green compacts on porous NiAl, J. Alloy. Comp. 492 (2010) 219–225.

5.5 S.T. Camagu, N.M. Mathabathe, D.E. Motaung, T.F.G. Muller, C.J. Arendse, A.S. Bolokang, Investigation into the thermal behaviour of the B2–NiAl intermetallic alloy produced by compaction and sintering of the elemental Ni and Al powders, Vacuum 169 (2019) 108919.

5.6 A.S. Mukasyan, J.D.E. White, D. Kovalev, N. Kochetov, V. Ponomarev, S.F. Son, Dynamics of phase transformation during thermal explosion in the Al–Ni system: Influence of mechanical activation, Physica B 405 (2010) 778–784.

5.7 J.D.E. White, R.V. Reeves, S.F. Son, A.S. Mukasyan, J. Phys. Chem. A 113 (2009) 13541–13547.

5.8 A. Aydogdu, Y. Aydogdu, O. Adiguzel, Long-term ageing behaviour of martensite in shape memory Cu–Al–Ni alloys, J. Mater. Proc. Technol. 153–154 (2004) 164–169.

5.9 A. Eftifeeva, E. Panchenko, Y. Chumlyakov, E. Yanushonite, G. Gerstein, H. J. Maier, On the high cyclic stability of the tensile two-way shape memory effect in stress-induced martensite aged $Co_{35}Ni_{35}Al_{30}$ single crystals, Mater. Sci. Eng. A, 799 (2021) 140166.

5.10 Yu Chao, Kang Guozheng, Rao Wei, Song Di, Modelling the stress-induced multi-step martensite transformation of single crystal NiMnGa ferromagnetic shape memory alloys, Mech. Mater. 134 (2019) 204-218.

5.11 A.S. Bolokang, M.N. Mathabathe, S. Chikosha, D.E. Motaung, Investigating the heat resistant properties of the TiNi shape memory alloy on the B19′→B2 phase transformation using the alloy powder, Surf. Interf. 20 (2020) 100608.

5.12 A.S. Bolokang, M.J. Phasha, Solid-state transformation in ball milled nickel powder, Mater. Lett. 64 (2010) 1894–1897.

UNIVERSITY of the WESTERN CAPE

5.13 A.S. Bolokang, M.J. Phasha, Thermal analysis on the curie temperature of nanocrystalline Ni produced by ball milling, Adv. Pow. Technol. 22 (2011) 518–521.

5.14 A.S. Bolokang, M.J. Phasha, S.T. Camagu, D.E. Motaung, S. Bhero, Effect of thermal treatment on mechanically milled cobalt powder, Int. J. Refract. Met. Hard Mater. 31 (2012) 258–262.

5.15 AS Bolokang, MJ Phasha, DE Motaung, S Bhero, Effect of mechanical milling and cold pressing on co powder, Journal of Metallurgy, 2012 (2012) |Article ID 290873 | https://doi.org/10.1155/2012/290873

5.16 R. Xiong, H. Peng, S. Wang, H. Si, Y. Wen, Effect of stacking fault energy on work hardening behaviors in Fe–Mn–Si–C high manganese steels by varying silicon and carbon contents, Mater. Des. 85 (2015) 707–714.

5.17 Y. Li, C. Li, J. Wu, Y. Wu, Z. Ma, L. Yu, H. Li, Y. Liu, Formation of multiply twinned martensite plates in rapidly solidified $Ni_3Al$-based superalloys, Mater. Lett. 250 (2019) 147–150.

5.18 H. Zhao, F. Qiu, S. Jin, Q. Jiang, High room-temperature plastic and work-hardening effect of the NiAl-matrix composites reinforced by particulates, Intermetallics 19 20 11) 376-381.

5.19 H.L. Zhao, F. Qiu, S.B. Jin, Q.C. Jiang, High work-hardening effect of the pure NiAl intermetallic compound fabricated by the combustion synthesis and hot pressing technique, Mater. Lett. 65 (2011) 2604–2606.

5.20 M. Clancy, M.J. Pomeroy, C. Dickinson, Austenite and martensite microstructures in splat-cooled Ni-Al, J. Alloys Compd. 523 (2012) 11– 15.

5.21 Y.X. Cui, L. Zhen, D.Z. Yang, G.P. Bi, Q. Wang, Effect of quenching rate on microstructures of a NiAl alloy, Mater. Lett. 48 (2001) 121–126.

UNIVERSITY of the WESTERN CAPE

5.22 I.R. Souza Filho, M.J.R. Sandim, D. Ponge, H.R.Z. Sandim, D. Raabe, Strain hardening mechanisms during cold rolling of a high-Mn steel: interplay between submicron defects and microtexture, Mater. Sci. Eng. A 754 (2019) 636–649.

5.23 O.O. Marenych, A.G. Kostryzhev, Z. Pan, H. Li, S. van Duin, Comparative effect of Mn/Ti solute atoms and TiC/Ni3(Al,Ti) nano-particles on work hardening behaviour in NiCu alloys fabricated by wire arc additive manufacturing, Mater. Sci. Eng. 753 (2019) 262–275.

5.24 B.M. Moshtaghioun, D. Gomez-Garcia, A. Dominguez-Rodriguez, R.I. Todd, Grain size dependence of hardness and fracture toughness in pure near fully-dense boron carbide ceramics, J. Eur. Ceram. Soc. 36 (7) (2016) 1829–1834.

5.25 S¸. Talas¸, G. Oruç, Characterization of TiC and TiB2 reinforced Nickel Aluminide (NiAl) based metal matrix composites cast by *in situ* vacuum suction arc melting, Vacuum 172 (2020) 109066.

5.26 M.X. Gao, Y. Pan, F.J. Oliveira, J.L. Baptista, J.M. Vieira, Interpenetrating microstructure and fracture mechanism of NiAl/TiC composites by pressureless melt infiltration, Mater. Lett. 58 (2004) 1761– 1765.

5.27 A.E. Karantzalis, A. Lekatou, K. Tsirka, Solidification observations and sliding wear behavior of vacuum arc melting processed Ni–Al–TiC composites, Mater. Charact. 69 (2012) 97–107.

UNIVERSITY of the WESTERN CAPE

# CHAPTER SIX

## Microstructure and hardness of Steel/Ni–TiC composite produced by compaction and sintering

*Published in Materials Today: Proceedings*

**Abstract**

The Steel/Ni reinforced with 1.0–1.5 wt% TiC composite material was developed by compaction and sintering processes. Optical microscopy and Zeiss-Auriga field-emission scanning electron microscope (FESEM) revealed that the TiC particles segregated around the spherical Steel/Ni grains. Moreover, the 1.0 wt % TiC- Steel/Ni composite has the FCC Steel/Ni matrix while the 1.5 wt% TiC- Steel/Ni composite is comprised of the BCC Steel/Ni phase. The large TiC grains were found mostly on the 1.0 wt% TiC- Steel/Ni composite. Additionally, the 1.5 wt% TiC-Steel/Ni composite was composed of the ultrafine TiC grains that surrounded the FeNi spherical grains. The FCC Steel/Ni (1.0 wt% TiC)) composite has lower average hardness compared to the B2 Steel/Ni (1.5 wt% TiC) phase.

**Keywords:** Composite; Steel/Ni; TiC; Phase transformation; Interface

### 6.1 Introduction

Reinforced composite materials are different from cemented carbides. The cemented carbides are composite materials comprised of the brittle refractory carbide material i.e WC, TiC fused by a binder such as Co, Ni, Fe powders by means of cold pressing followed by sintering to provide good combination of high hardness, wear resistance, good

UNIVERSITY of the WESTERN CAPE

strength and adequate fracture toughness **[1–4]**. The carbide particles are added to a commonly ferromagnetic metallic binders (Co, Fe, Ni) **[5,6]**. The TiC is an abrasive resistance material with FCC crystal structure and properties such as high thermal resistance, good hardness, elastic modulus, low density, chemical stability, and excellent wear and oxidation resistance **[7]**. Combination of binder materials can be used in cemented carbide production. For example, the sintered TiC-Fe-Co-Ni-Cr-Mo cermets has hardness of 64 HRC to 68 HRC with the best corrosion resistance **[8]**. This multi-alloying of several metals are high entropy alloys. They provide better mechanical properties in TiC reinforced composites **[9]**. The expected phases could be FeTi which further decompose at high temperature providing the feasibility of Ti and C forming TiC **[9]**. High entropy alloys proved to refine grain size, promote high yield strength and high strain hardening **[10]**. Furthermore, the Ni/TiC composite layers has yielded a well distributed TiC particles through a matrix with average hardness of 1540 Vickers positioning a material as a good candidate for wear resistance applications **[11]**. On the other hand, composites are classified by the carbide particle reinforcements, whisker reinforcements, fiber reinforcements etc **[12]**. Other studies show that the Fe–Cr–Ni reinforced TiC matrix composite leads to creep resistance improvement **[13]**. The (Fe,Ni)–TiC MMC prepared by direct metal laser sintering led to FCC to BCC matrix phase transformation which resulted in the cracking of composite material. To avoid cracking of the material, the TiC addition was reduced although with challenges of porosity **[14]**. This is because the laser sintered materials are associated with rapid cooling that induce highly strained metastable phases **[15]**. This process may lead to high stresses that will lead to material cracking. Microstructure of Fe–TiC composite cladding resulted in martensitic structure with high hardness **[16]**. TiC-Fe composite has the high hardness and strength when free C is avoided in the microstructure. The strong interfacial bonding between the TiC particles and Fe alloy matrix contribute to the improved mechanical

UNIVERSITY of the WESTERN CAPE

properties. The interfaces of TiC and the matrix showed no reaction with the structure of the matrix changing from FCC structure to BCC and FCC bi-phase structure **[17]**. The presence of hard TiC particles in ferrous matrix promotes high hardness of the metal matrix composite which can be used as effective coating materials **[18]**. In this study, steel and Ni powders were mixed to form a matrix reinforced with ultrafine TiC particles. Since, Ni is an austenite stabilizer and a poor carbide former, an FCC (austenite) matrix reinforced with fine TiC hard particles was realized.

### 6.2 Experimental procedure

The steel powder is composed 0.68 wt.% Si, 1.78 wt.% Cr, 1.08 wt.% Mn and 0.29 wt.% C. The steel and nickel powders were mixed at 3:1 weight ratio and added to 1.0 and 1.5 wt.% nanosized TiC powder, respectively. The 3:1 powder ration in composition was chosen since Ni is an austenite stabilizer to induce ductility of the matrix. Addition if 1.0 and 1.5 wt.% nanosized TiC powder was added to improve the hardness of the composite material and produce a composite material with combination of hardness and ductility. Low content (1 to 5 wt.%) of nano particles within a composite is favoured as higher content results in agglomeration of the nano particles on the grain boundaries which leads to compromised mechanical properties. Powder mixtures were then cold pressed at 30 MPa enough pressure to produce compacts with minimum porosity, sintered in the argon flowing tube furnace at 1400 °C for 2 hours to avoid contamination such as $O_2$ and $N_2$ gases. Metallographic examinations were conducted on the as-sintered specimens, which were ground up-to 4000 SiC grit papers, with subsequent polishing in colloidal silica. The microstructures were observed by the scanning electron microscopy (SEM) which is equipped with energy dispersion spectroscopy (EDS) for micro-analyses. In addition to this, phase identification was performed using x-ray diffraction (XRD) technique with CuKα radiation λ=1.54062 Å and 2θ from 20°-90°. Micro-Vickers hardness

UNIVERSITY of the WESTERN CAPE

(HV) measurements were performed at applied load of 500 gf and dwelling time of 10s. Hardness profiles throughout the specimens were measured at average of at-least 10 measurements.

### 6.3 Results and Discussions

The optical microstructure of the 1.0 TiC- Steel/Ni composite is shown in Fig. 1a while the 1.5 wt. % TiC- Steel/Ni composites are illustrated in Fig. 1b-c. Three phase have emerged after sintering which were distinguished by the light, light-grey and dark-grey colours. The spherical light phase belongs to the FeNi matrix while the light-grey and dark-grey phases are TiC phase. The TiC grains were segregated and surrounded the spherical Steel/Ni grains. The TiC grains are very fine and expected to increase the hardness/strength of the composite. Some of the TiC ultrafine grains were dispersed on the surface of the Steel/Ni grains.

UNIVERSITY of the
WESTERN CAPE

http://etd.uwc.ac.za/

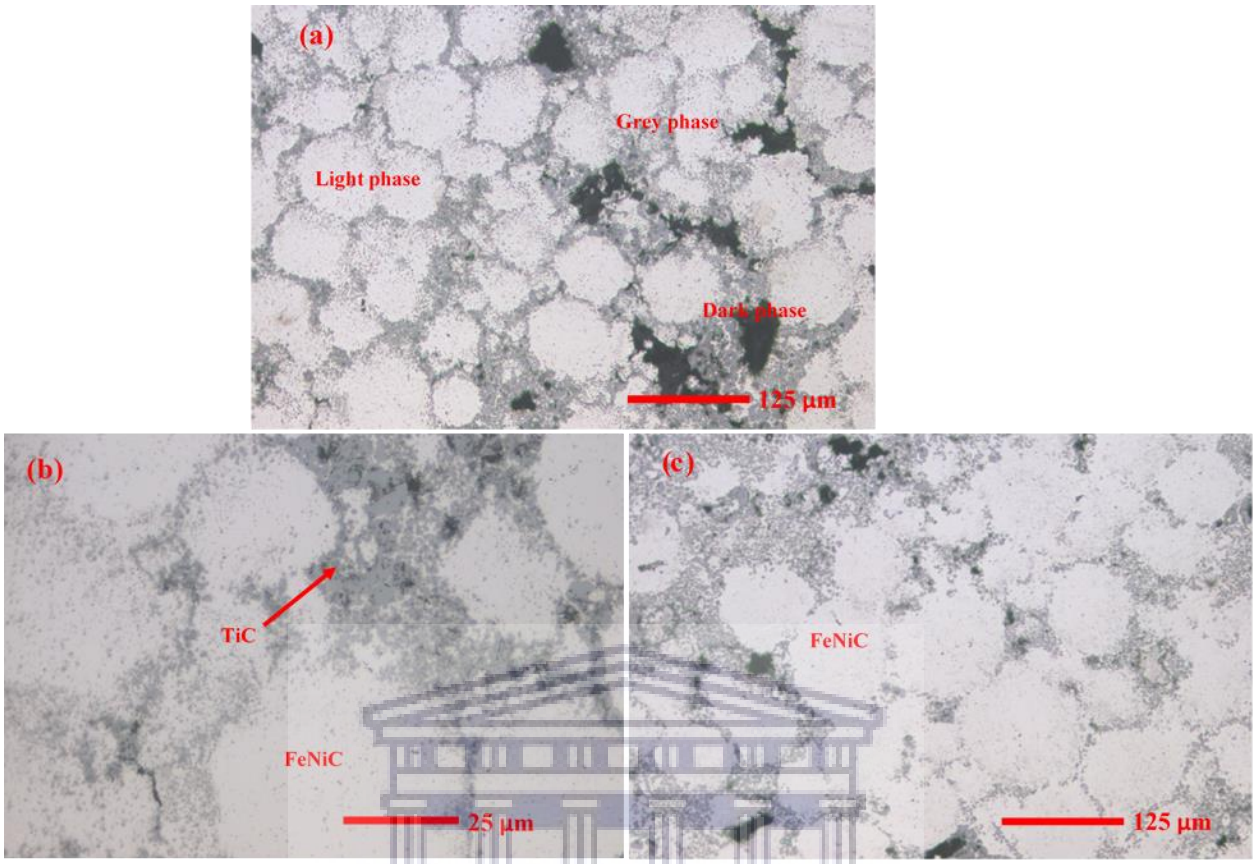


**Figure 6.1**: Optical microstructures of the (a) 1.0 wt% TiC- Steel/Ni and (b,c) 1.5 wt% TiC- Steel/Ni composite at different magnifications.

UNIVERSITY of the
WESTERN CAPE

Fig. 6.2a shows a corresponding SEM image of the 1.0 wt. % TiC- Steel/Ni composite. The light and dark grey TiC grains were evident. Moreover, the surface porosity on the 1.0 wt. % TiC-FeNi microstructure was revealed. Figs.6.2b, c shows the two SEM images of the 1.5 wt.% TiC-FeNi composites. The TiC grains formed a network around the FeNi grains. The distribution of the TiC grains reveals a mixture of large and ultrafine grains with different grain distribution than those of the 1.0 wt. % TiC-FeNi composite. In general, the SEM images compliment the optical microstructures shown in Fig. 1a-c. Table 6.1 displays the EDS results revealing the presence of Ni, Fe, Cr, Si, Ti and C. The 1.0 wt.% TiC reinforced material has the low carbon content of 5.61 wt.% while the 1.5 wt.% TiC composite is composed of 8.91 wt.% C. The Fe:Ni ratios are 64.59: 25.56 and 57.44: 27.56 for 1.0 and 1.5 wt.% TiC, respectively. The EDS analysis confirmed the

http://etd.uwc.ac.za/

absence of Ni content on the TiC phase for both the 1.0 wt. % and 1.5 wt. % TiC composite. However, no oxygen content was detected by the EDS implying the oxidation was minimal.

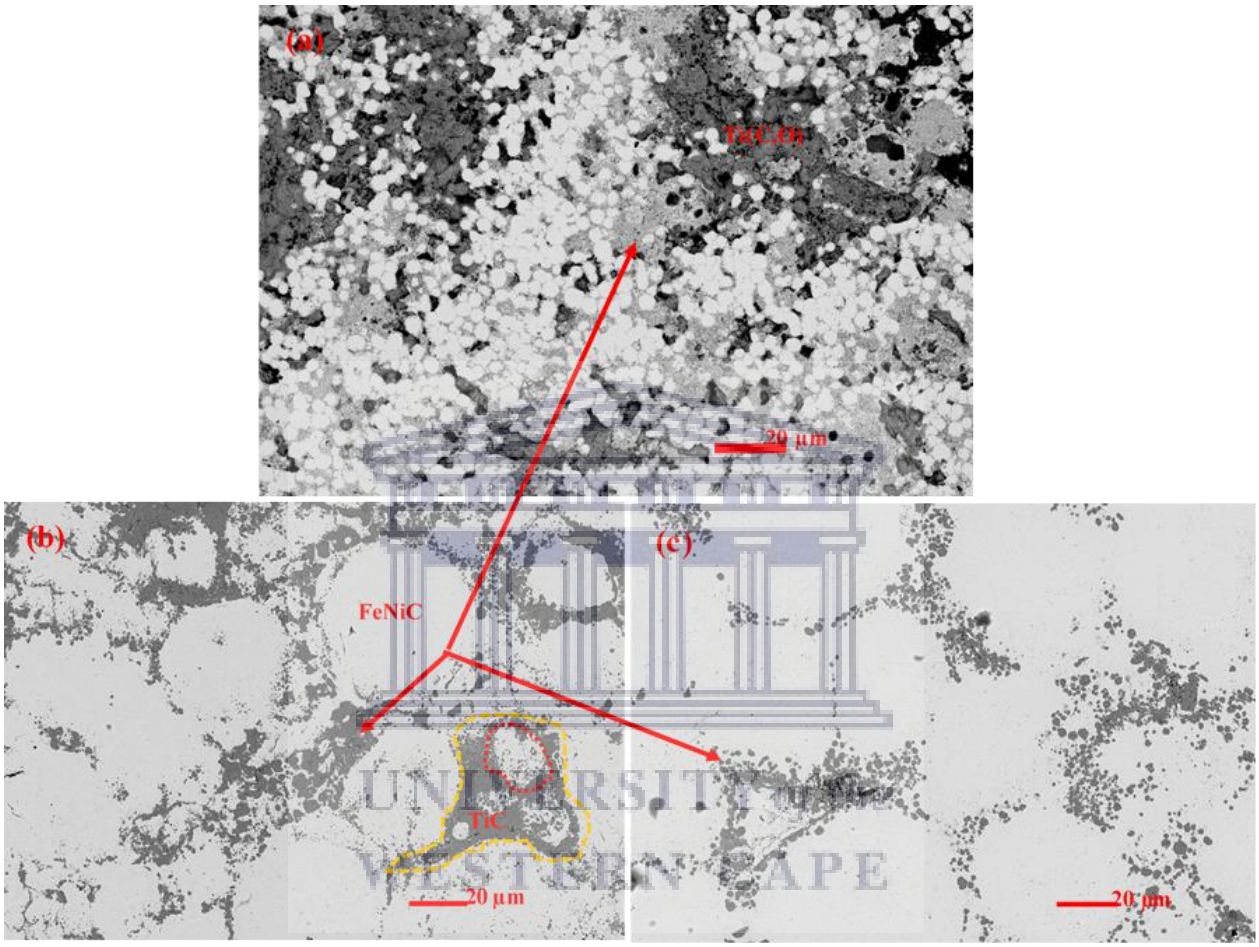


**Figure 6.2**: SEM images of the (a) 1.0 wt.% TiC-FeNi and (b,c) 1.5 wt.% TiC- Steel/Ni composite.

UNIVERSITY of the WESTERN CAPE

**Table 6.1**: EDS analysis of the Steel/Ni phase in the 1.0 and 1.5 wt.% TiC composites

| Elements | 1.0 wt.%TiC FeNi | 1.5 wt.%TiC FeNi |
|---|---|---|
| C | 5.61 | 8.91 |
| Si | 0.008 | 0.12 |
| Cr | 1.44 | 1.50 |
| Fe | 64.59 | 57.44 |
| Ni | 25.56 | 27.56 |
| Ti | 2.72 | 4.29 |
| O | – | – |

XRD analysis of TiC, 1.0 wt% TiC- Steel/Ni and 1.5 wt% TiC-Steel/Ni composites is shown in Fig. 6.3a-c. The crystal structure of the steel powder, not shown in the current XRD pattern, is comprised of BCC (ferrite) with lattice parameter a=2.86 Å and Im-3m # 229 space group and number. The XRD analysis of TiC powder in Fig. 6.3a revealed an FCC crystal structure with lattice parameter a=4.303 Å and Fm-3m # 225 space group. After sintering, the 1.0 wt% TiC-Steel/Ni mixture (Fig. 6.3b) reveals two FCC phases with different lattice parameters. The FCC Steel/Ni matrix with lattice parameter a=3.610 Å was detected. It implies that the BCC steel phase has transformed to FCC austenite due to the presence of Ni. On the other hand, the XRD pattern of 1.5 wt.% TiC-Steel/Ni composite (Fig. 6.3c) was composed of B2 Steel/Ni crystal structure with lattice parameter a=3.59 Å of Pm-3m # 221 space group. This crystal orientation is attributed higher C content on the Steel/Ni phase. TiC grains were located at the interface of the spherical FeNi grains, much finer, homogenous when compared to those of the 1.0 wt. % TiC sample as shown in Fig. 6.1 and Fig. 6.2. It is evident that Nickel has induced the FCC (austenite) matrix reinforced with ultrafine TiC hard particles.

UNIVERSITY of the WESTERN CAPE

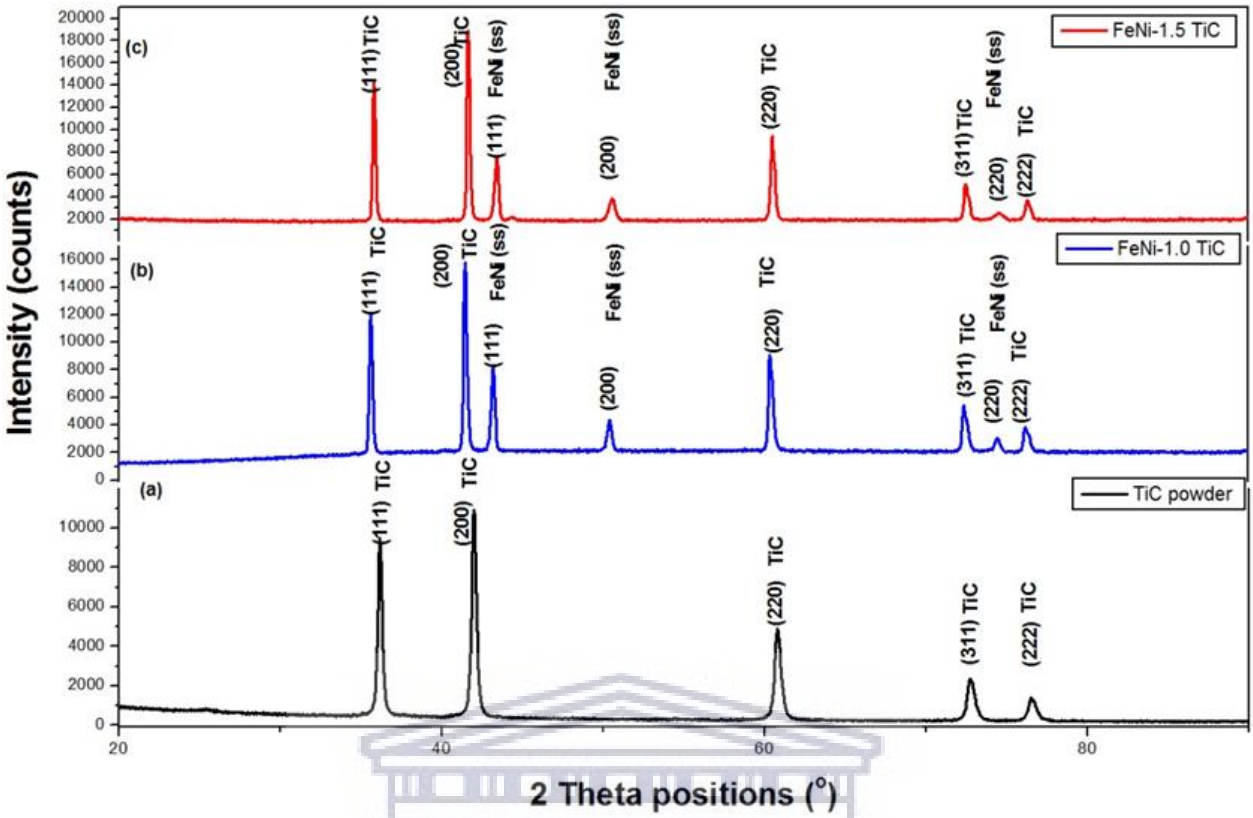


**Figure 6.3**: XRD analysis of the TiC- Steel/Ni composite containing 1.0 wt% and 1.5 wt% TiC.

The microhardness of the 1.0 wt% TiC-Steel/Ni composite is shown in Fig. 6.4. On average, the FCC Steel/Ni matrix is composed of 308 Hv while TiC-rich area has the average hardness of 495 HV. The low hardness on the TiC-rich phase attest to the soft austenitic matrix. However, there are areas where extreme hardness values of ~650 HV were measured. Fig. 6.4 shows the microhardness measurements of the 1.5 TiC-Steel/Ni composite. For this composite material, the average hardness for the Steel/Ni BCC matrix was 411 HV, slightly higher due to high C content found on the Steel/Ni matrix. The TiC-rich phase has 536 HV average hardness, an increase due more ultrafine TiC grains. As displayed in Table 6.1, the C content of the 1.5 wt% TiC-Steel/Ni is higher than that of 1.0 wt% TiC- Steel/Ni composite. Moreover, the SEM analysis confirmed high ultrafine grains in the 1.5 wt. % TiC- Steel/Ni than in the 1.0 wt% TiC- Steel/Ni composite. The results

UNIVERSITY of the WESTERN CAPE

show that the average hardness of the matrix steel/Ni matrixes was improved by the TiC reinforcement.

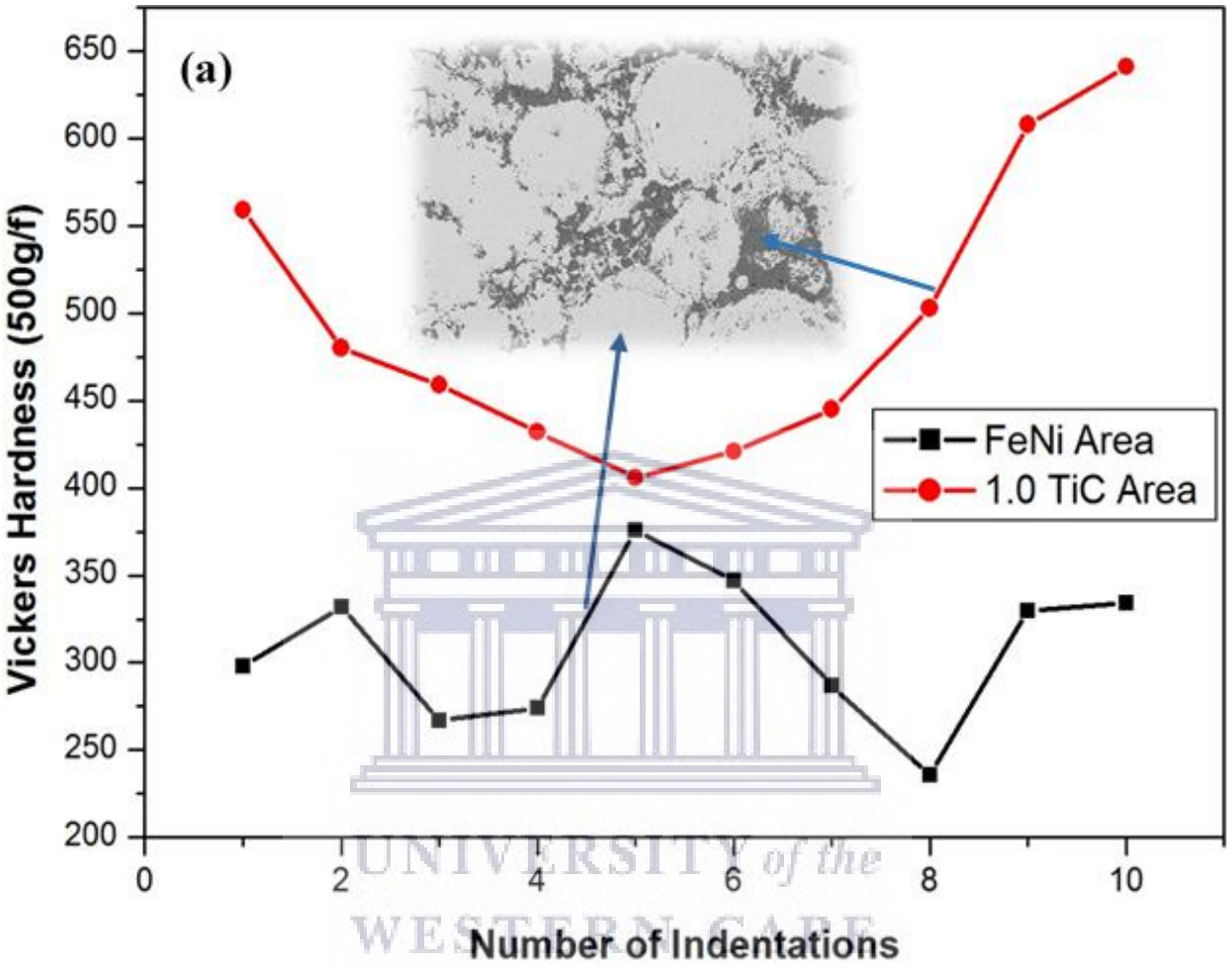


**Figure 6.4**: Microhardness of the 1.0 wt% TiC-1.5 wt.% TiC-1.5 wt.% TiC- Steel/Ni composite.

### 6.4 Conclusions

The Steel/Ni reinforced with 1.0 -1.5 wt.% ultrafine TiC composites were developed through powder metallurgical compaction and sintering processes. TiC particles segregated around the spherical FeNi grains on the 1.0 wt.% and 1.5 wt.% TiC composite materials. The structural analysis revealed that the 1.0 wt.% TiC-Steel/Ni was composed of the FCC matrix while the 1.5 wt.% TiC-Steel/Ni composite had B2 (BCC) crystal

UNIVERSITY of the WESTERN CAPE

structure. Larger TiC grains were found on the 1.0 wt.% TiC-Steel/Ni composite. On the 1.5 wt.% TiC-Steel/Ni composite, the spherical Steel/Ni matrix was surrounded by the ultrafine TiC grains. The 1.0 wt.% TiC-Steel/Ni composite was composed of lower average hardness when compared to the 1.5 wt.% TiC-FeNi composite.

**References**

6.1 S. Fang, L. Llanes, Mater. Charact. 159 (2020) 110061

6.2 I. Konyashin, L.I. Klyachko, Int. J. Refract. Met. Hard Mater. 49 (9–26) (2015).

6.3 Q. Ding, Y. Zheng, Z. Ke, G. T. Zhang, H. Wu, X.Y. Xu, X. Lu, X. Zhu, Int. J. Refract. Met. Hard Mater. 87 (2020) 105166

6.4 A.S. Bolokang, M.J. Phasha, C. Oliphant, D. Motaung, Int. J. Refract. Met. Hard Mater. 29 (2011) 108–111.

6.5 A.S. Bolokang, M. J. Phasha, D. E.Motaung, and S. Bhero, J. Metallurgy, 2012 (2012) 1-7, Article ID 290873.

6.6 A.S. Bolokang, M.J. Phasha, Adv. Pow. Metallurg. 22 (2011) 518-521.

6.7 Y. Tan, H. Cai, X. Cheng, Z. Ma, Z. Xu, Z. Zhou, Mater. Lett. 228 (2018) 1–4.

6.8 Q. Zhuang, N. Lin, Y. He, X. Kang, Ceram. Int. 43 (2017) 15992–15998.

6.9 X. Sun, H. Zhu, J. Li, J. Huang, Z. Xie, Mater. Sci. Eng. A 743 (2019) 540–545.

6.10 D. Yim, P. Sathiyamoorthi, S-J. Hong, H. S. Kim, J. Alloys Compd. 781 (2019) 389-396.

6.11 M.R. Gorjia, C. Edtmaier, S. Sanjabi, Mater. Des. 125 (2017) 167–179.

6.12 L.J. Huang, L. Geng, H.X. Peng, Prog. Mater. Sci. 71 (2015)

6.13 X.D. Hui, Y.S. Yang, Z.F. Wang, G.Q. Yuan, X.C. Chen, Mater. Sci. Eng. A 282 (2000) 187–192.

6.14 A. Gäärd, P. Krakhmalev, J. Bergström, J. Alloys Compd. 421 (2006) 166–171.

6.15 A. Botes, A.S. Bolokang, I. Kortidisc, V. Matjeke, Surf. Interf. 14 (2019) 296–304.

UNIVERSITY of the WESTERN CAPE

6.16 H. Zeinali Moghaddam, M. Sharifitabar, G. Roudini, Surf. Coat. Technol. 361 (2019) 91–101.

6.17 J. Lee, D. Lee, M. H. Song, W. Rheed, H. J. Ryu, S. H. Hong, J. Mater. Sci. Technol. 34 (2018) 1397–1404.

6.18 J. Zhua, L. Zhonga, Y. Xua, X. Cai, F. Bai, Y. Ding, Z. Lu, H. Wu. Vacuum 155 (2018) 631–636.



UNIVERSITY of the
WESTERN CAPE

http://etd.uwc.ac.za/

# CHAPTER SEVEN

## Surface characterization and formation mechanism of the ceramic $TiO_{2-x}N_x$ spherical powder induced by annealing in air

*Published in Powder Technology Journal*


### Abstract

Mechanism for the formation of titanium oxynitride ($TiO_{2-x}N_x$) on the surfaces of spherical Ti powder particles upon heat treatment in air at 500, 600, 700 and 800 °C was investigated. The results showed that the first at 500 °C a hexagonal closed packed (HCP) $TiO_x$ film was formed while a $TiO_2$ film was observed after annealing at 600 °C and eventually a $TiO_{2-x}N_x$ layer coated the spherical Ti particles at 700 and 800 °C due to N diffusion within the $TiO_2$ crystal lattice. The resulting surface structure was studied by means of x-ray diffraction (XRD) while the surface morphology of the powders was characterized using the scanning electron microscope (SEM) attached with energy dispersive x-ray spectroscopy (EDS) detector. The AFM images confirmed that when the N content increases (800 °C-heat treated sample) the powder loses its triangular grains (700 °C-annealed sample) to irregular shaped grains.


**Keywords:** Titanium; $TiO_{2-x}N_x$; Oxidation; Characterization, Thermal analysis

### 7.1 Introduction

Titania ($TiO_2$) is widely used in the electronics, ceramics, medicine, chemical, energy (solar), environmental applications and pigment industries **[1-4]**. $TiO_2$ is a well-known mineral that occurs in three phases: rutile, anatase, and brookite, each having different crystal structures. By contrast, titanium nitride (TiN), is coating material wits excellent

UNIVERSITY of the WESTERN CAPE

chemical stability and excellent tribological properties which can be produced by combustion of powder in air **[5]**. At high temperatures both $TiO_2$ and TiN accept N and O atoms, respectively, to occupy interstitial sites and form titanium oxynitride ($TiO_xN_y$) another class of important composite materials. The $TiO_xN_y$ films rich in oxygen are used as thin film resistors **[6]**, solar selective collectors **[7, 8]** while the nitrogen rich $TiO_xN_y$ films are used as anti-reflective coatings **[9]** and biomaterials coated stents with a better clinical performance compared to uncoated stainless steel stents **[10,11]**. This class of materials is known to possess excellent electronic and optical properties **[1].** Furthermore, titanium oxynitrides have recently been explored as possible gas sensing materials with promising performance **[12, 13]**. Photocatalytic properties of titanium oxynitride can be used in super hydrophilic windows, air purification devices, and for degradation of organic molecules on titanium oxynitride surfaces **[14]**. Formation of oxynitrides on titanium alloys is achieved by different techniques including gas diffusion treatment during annealing **[15, 16]**, chemical process **[17]** and radio frequency magnetron sputtering deposition **[18]**. The feasibility of mixed metal titanium oxynitride has been extensively explored for various applications **[18-20]**. The binder system is a common way of producing ceramic nitrides and oxynitrides. Combination of Al-Ni binder for cBN-based composites produced outstanding mechanical properties with acceptable flexural strength, fracture toughness, hardness, and abrasive **[21]**. Similarly, as aluminium metal matrix composite such as Al-Si alloys with improved their wear resistance are developed from the oxides or mixed-metal oxides **[22]**. These materials can be used in defence, aerospace, automobile, and other structural applications as fuel efficient advanced materials for different tribological applications **[23]**. The oxide/nitride layer formation on Ti surface involves a solid-state diffusion process when Ti is exposed in oxygen or air. Some of the manufacturing processes such as laser cladding prefer spherical particles for 3D printing **[24]** hence the study on the formation of the oxidised spherical particles is necessary. The formation of

UNIVERSITY of the WESTERN CAPE

the nitride layer on spherical Ti particle and their thermal stability revealed structural change and phase transformation depending on the annealing temperature **[25]**. It has been acknowledged that metal oxides are of great importance and has impact in the current environmental challenges as well as electronics due to their capability to generate charge carriers when they are energised. They are also potential photocatalyst, hence these materials should be considered necessary. The current study illustrates the stages of oxide layer deposited on the spherical Ti particle using annealing process in air.

### 7.2 Experimental Details

Atomised commerically pure (CP) Ti (99.8%) powder was used in the current investigation. Samples of CP Ti powder were annealed in a muffle furnace for 2 h in air at 500, 600, 700, 800 °C, respectively followed by furnace-cooling. Another sample of CP Ti powder was annealed at 800 °C followed by air-cooling. The density of the powders was measured by Micromeritics AccuPyc II 1340 Gas Pycnometer. Powder morphology analysis was conducted using a high-resolution scanning electron microscope (HR-SEM, Auriga ZEISS) coupled with a Robinson Backscatter Electron Detector and an Oxford Link Pentafet energy dispersive x-ray spectroscopy (EDS) detector. Phase evolution was determined with the use of a PANalytical X'pert PRO PW 3040/60 X-ray diffraction (XRD) machine, using Cu $K_\alpha$ radiation as source. The topography of the spherical Ti powder particles was analysed using atomic force microscopy (AFM, Veeco, Digital Instruments). Thermal analysis was carried out using Differential Scanning Calorimetry (DSC) and Thermo Gravinometry (TG) incorporated in NETZSCH STA. Powder samples were heated up to 1200 °C and cooled to room temperature using $Al_2O_3$ as a baseline during the thermal analysis. A heating rate of 20 °C $min^{-1}$ under argon gas with 20 ml/L standard flow rate was used.

UNIVERSITY of the WESTERN CAPE

## 7.3 Results and Discussion

*7.3.1 Powder Characterization*

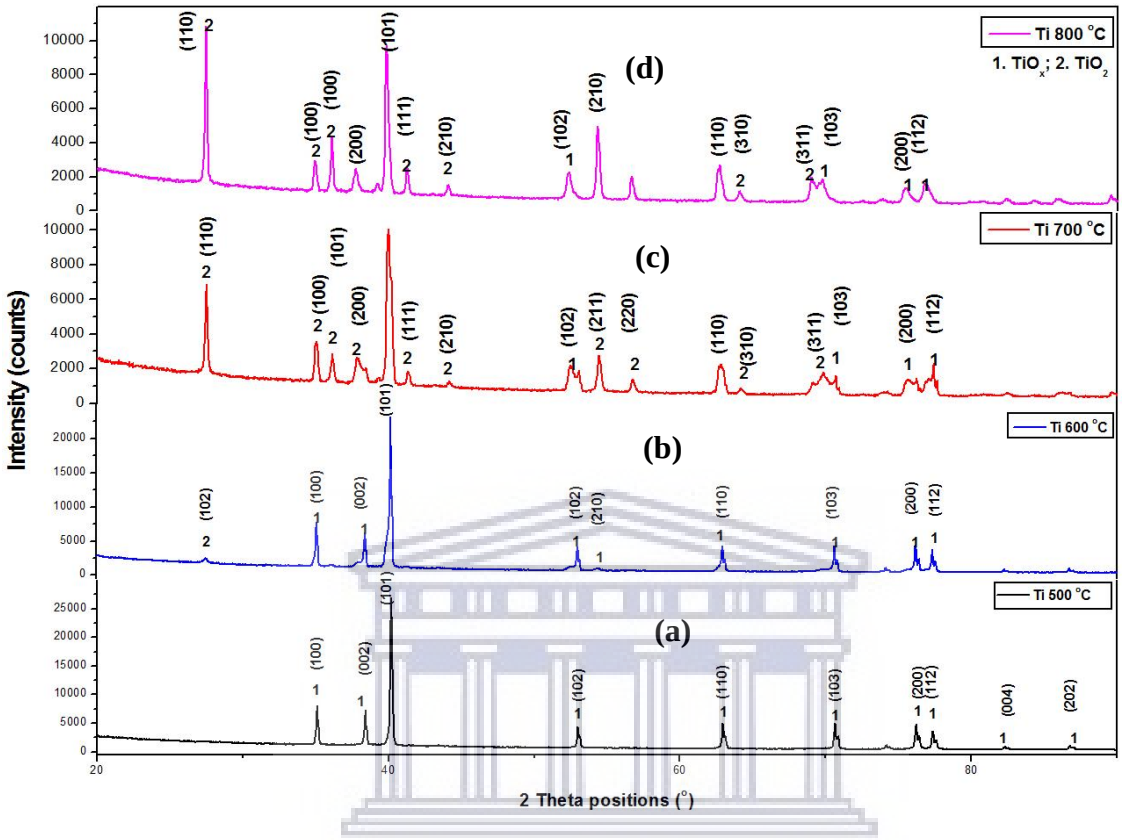


**Figure 7.1**: XRD pattern of the Ti powder oxidised at (a) 500, (b) 600, (c) 700 and (d) 800 °C.

UNIVERSITY of the
WESTERN CAPE

Fig. 7.1. shows XRD pattern of the CP Ti powder after annealing at (a) 500, (b) 600, (c) 700 and (d) 800 °C in air. Pure Ti has an HCP crystal structure with lattice parameters *a*=2.951; *c*=4.684 and *c/a*=1.587**.** Upon annealing at 500 °C, the Ti powder, the lattice parameters of the HCP phase have changed to *a*= 5,140 Å; *c*= 9.480 Å with *c/a*=1.844 which is attributable to HCP $TiO_x$ phase (**Fig. 7.1a)**. Minor peaks belonging to tetragonal rutile $TiO_2$ phase co-existing with the HCP $TiO_x$ have started to emerge upon annealing at 600 °C as shown in **Fig. 7.1b**. These tetragonal XRD peaks increased in intensity at 700 and 800 °C powder samples, respectively **(Fig. 7.1c-d)**. The rutile-type phase has

the lattice parameters of *a*= 4.591 Å; *c*=2.958 Å and *c/a*=0.644 attributable to titanium oxynitride formation. The current findings agree with those of Kikuchi et al., **[26]** whereby nitrogen diffusion on commercially pure (CP) Ti was found to occur above 600 °C. However, in the current study, nitrogen diffusion seems to prefer the intergranular penetration on the spherical particle. Kikuchi et al., **[26]** conducted investigation on material annealed in nitrogen environment while for the current study; the annealing was done in air, hence the different diffusion mechanism.

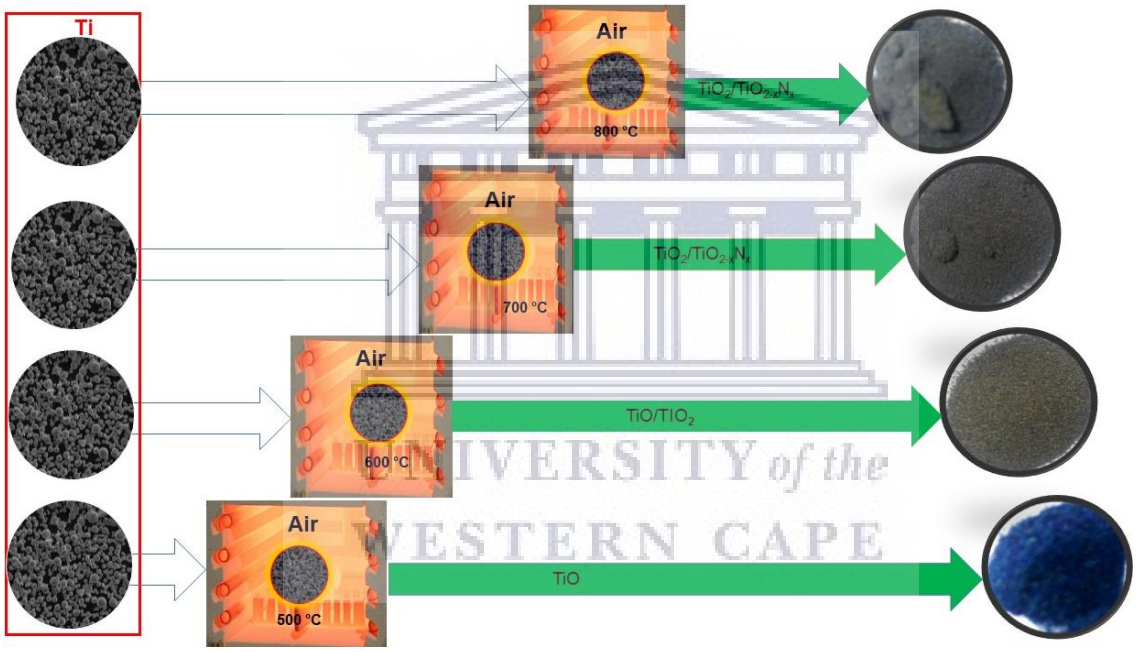


**Figure 7.2**: Change in the colours of the powders associated with phase transformation upon annealing.

As shown in **Fig. 7.1**, the XRD analysis confirmed transformation in pure Ti during annealing in air as follows; Ti (HCP) → $TiO_x$ (HCP) → $TiO_2$/ $TiO_{2-x}N_x$. Due to the strong affinity of O for Ti when compared to N, a rapid formation of the blue $TiO_x$ film forms on the particle surfaces at 500 °C as shown in **Fig. 7.2**. The chemical reactions with their free energy formations are presented in **Eq. 1-3**. This implies that the formation of $TiO_x$

http://etd.uwc.ac.za/

is favourable to form first followed by $TiO_2$. Once the $TiO_2$ has formed at high temperatures (700 to 800 °C), the N atoms diffuses into rutile. These crystal structure changes also yield physical changes as shown in **Fig. 7.2**. The powder changes from grey (Ti) to blue ($TiO_x$). The sample annealed at 600 °C displays a mixture of grey and yellow colours. Upon annealing at 700 and 800 °C the yellow colour became more conspicuous. These observations are in agreement with the structural development identified by the XRD analysis as the powder comprises a mixture of phases.

$2Ti + O \rightarrow 2TiO$ $\Delta G^\circ_{1200^\circ C} = -827$ kJ/ mol (1)

$Ti + O_2 \rightarrow TiO_2$ $\Delta G^\circ_{1200^\circ C} = -711$ kJ/ mol (2)

$Ti + 1/2N_2 \rightarrow TiN$ $\Delta G^\circ_{1200^\circ C} = -418$ kJ/ mol (3)

UNIVERSITY of the
WESTERN CAPE

http://etd.uwc.ac.za/

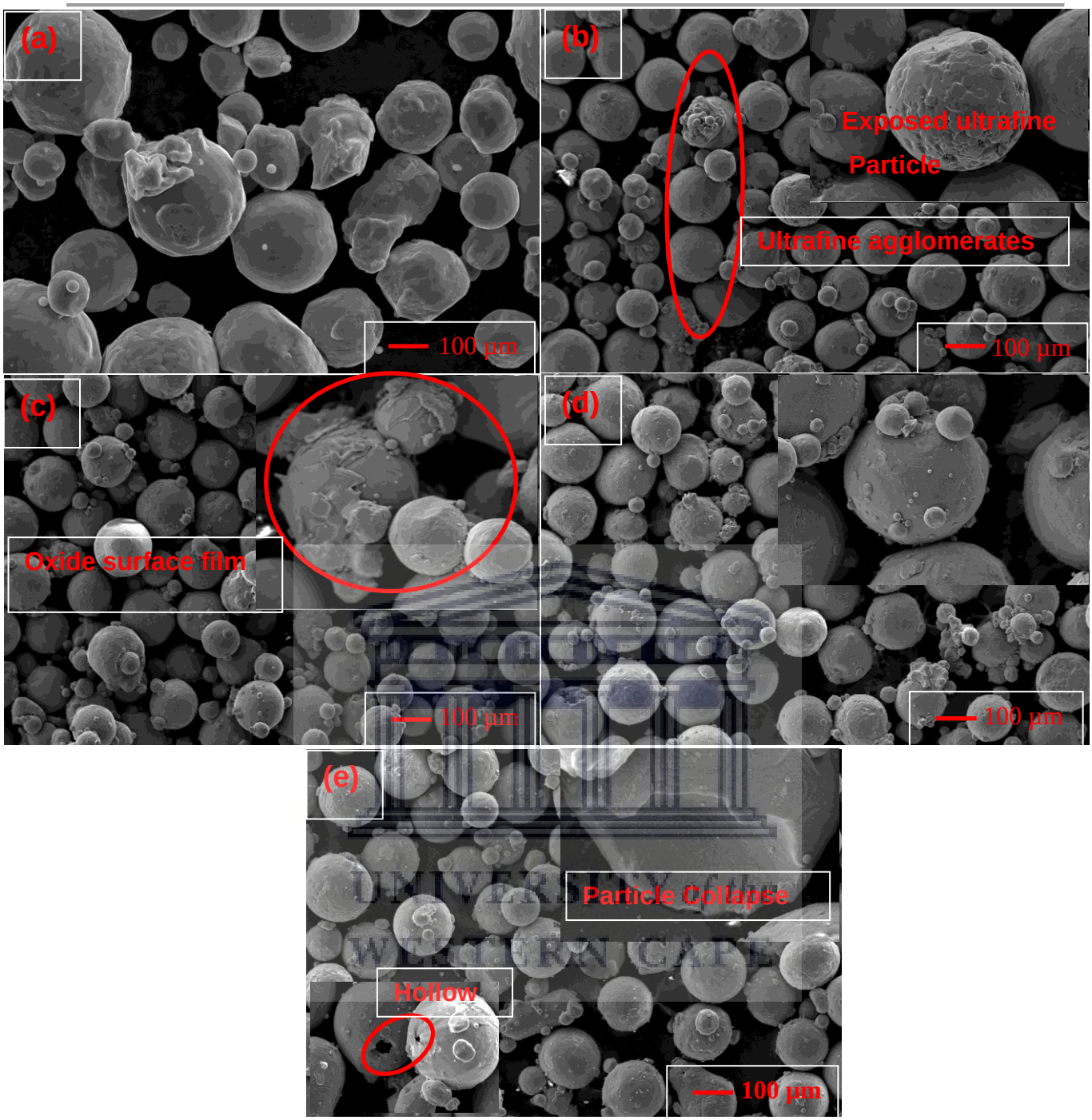


**Figure 7.3**: SEM images of the furnace-cooled (a) CP Ti, (b) 500, (c) 600, (d) 700, (e) and 800 °C powder annealed in air

Powder of varying particle sizes can be seen. Upon annealing at 500 °C, the smaller and the larger particles fused forming satellites (**Fig. 7.3b)**. Furthermore, the spherical particles revealed porous and rough surfaces. Porosity layer on the particle surfaces

provide for an easy transportation of gas during annealing since the particle surface is the first point of contact during diffusion. **Fig. 7.3c** shows evidence of the oxide film that has developed on the surface of the spherical particles at 600 °C. Upon annealing at 700 °C, the ultrafine particles form agglomerates as shown in **Fig. 7.3d**. It is evident that upon annealing at 800 °C, few particles collapsed as the porosity increased due to gas diffusing through the internal structure of the particle (**Fig. 7.3e)**. The predictions of such interaction of oxygen and nitrogen molecules with hexagonal close packed Ti (001) surfaces revealed that oxygen is adsorbed on the surface with increasing concentration and tend to migrate to interior layer after surface saturation **[27]**. On the contrary, nitrogen prefers to migrate into the interior layers favourably in the octahedral interstitial site for both oxygen and nitrogen **[27]**. This study further confirms that Ti has a stronger affinity to oxygen than nitrogen and their diversity in reactivity. By means of comparison to the heat treated and furnace cooled samples, a sample was heat treated at 800 °C followed by air cooling. The morphology and surface analysis of the powder with corresponding EDS results are shown in **Fig. 7.4** and **Fig. 7.5.**

UNIVERSITY of the
WESTERN CAPE

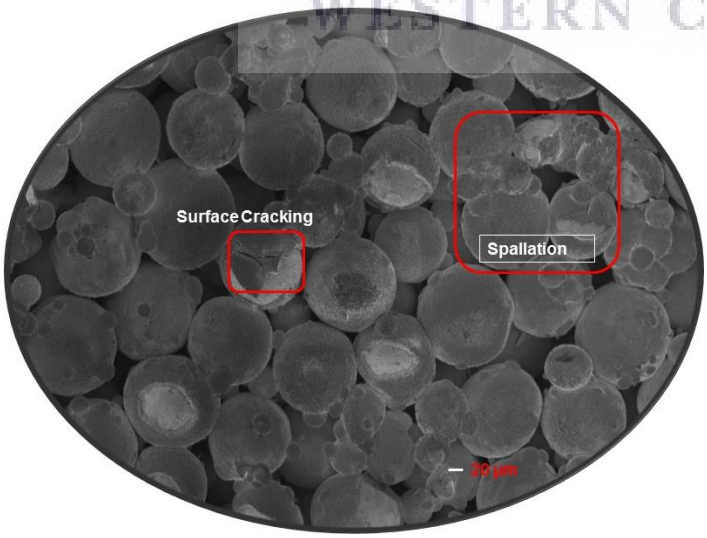


**Figure 7.4**: SEM images of CP Ti powder annealed at 800 °C in air followed by air-cooling.

Surface cracking and spallation (**Fig. 7.4)** due to thermal stresses is observed on the air quenched powder. This behaviour is attributed to a mismatch in thermal expansion between surface layers ($Ti/TiO_x/TiO_2/TiO_{2-x}N_x$) **[28-30]**. This linear coefficient of thermal expansion for different layers can be explained by **Eq 4**.

$$\alpha_L = \frac{1}{L_0}\frac{\Delta L}{\Delta T} \qquad (4)$$

Where $\alpha_L$ is the coefficient of thermal expansion (CTE), $L_0$ and the lineal expansion of the material with respect to the temperature $\Delta L/\Delta T$. The mismatch in thermal expansion between $TiO_{2-x}N_x$, $TiO_2$ and $TiO_x$ increase and decrease at higher and lower temperatures **[28]**. Due to high cooling rates, the $TiO_{2-x}N_x$ film experienced higher stresses than the core structure underneath. A model for such hard films developed by Limarga and Wilkinson revealed a large residual stress induced in the nitride scale due to the mismatch of creep rates **[31].**

UNIVERSITY of the
WESTERN CAPE

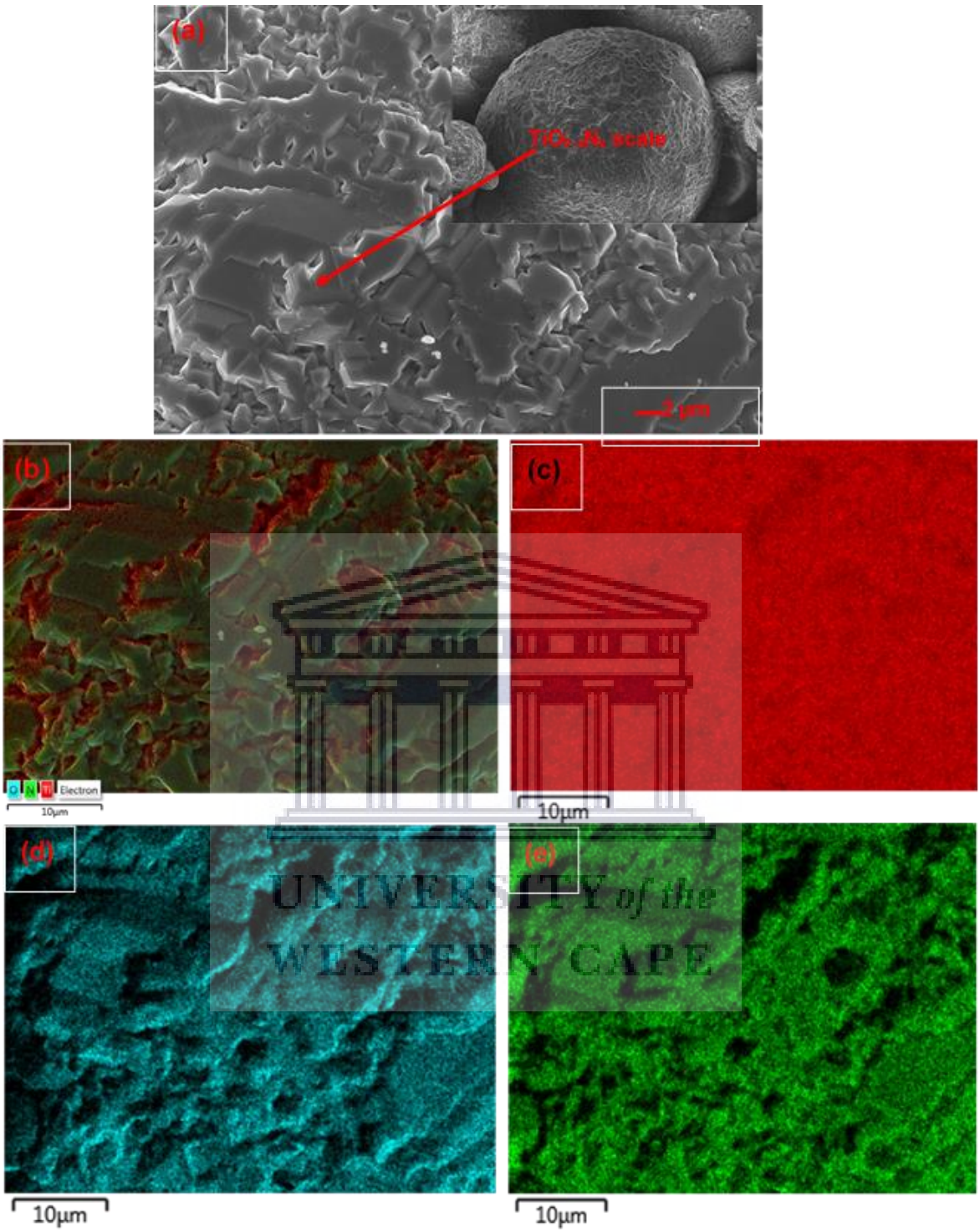


**Figure 7.5**: SEM and EDS images of the powder particles upon annealing at 800 °C followed by air cooling.

The SEM images of the powder particle oxynitride film **(Fig. 7.5a)** shows multiple-layered triangular grain patterns with varying N and O concentrations. EDS mapping confirmed

UNIVERSITY of the WESTERN CAPE

the presence of N and O on the surfaces of the spherical particles. The oxygen-rich $TiO_{2-x}N_x$ was determined from the EDS data to be $TiO_{1.5}N_{0.5}$.

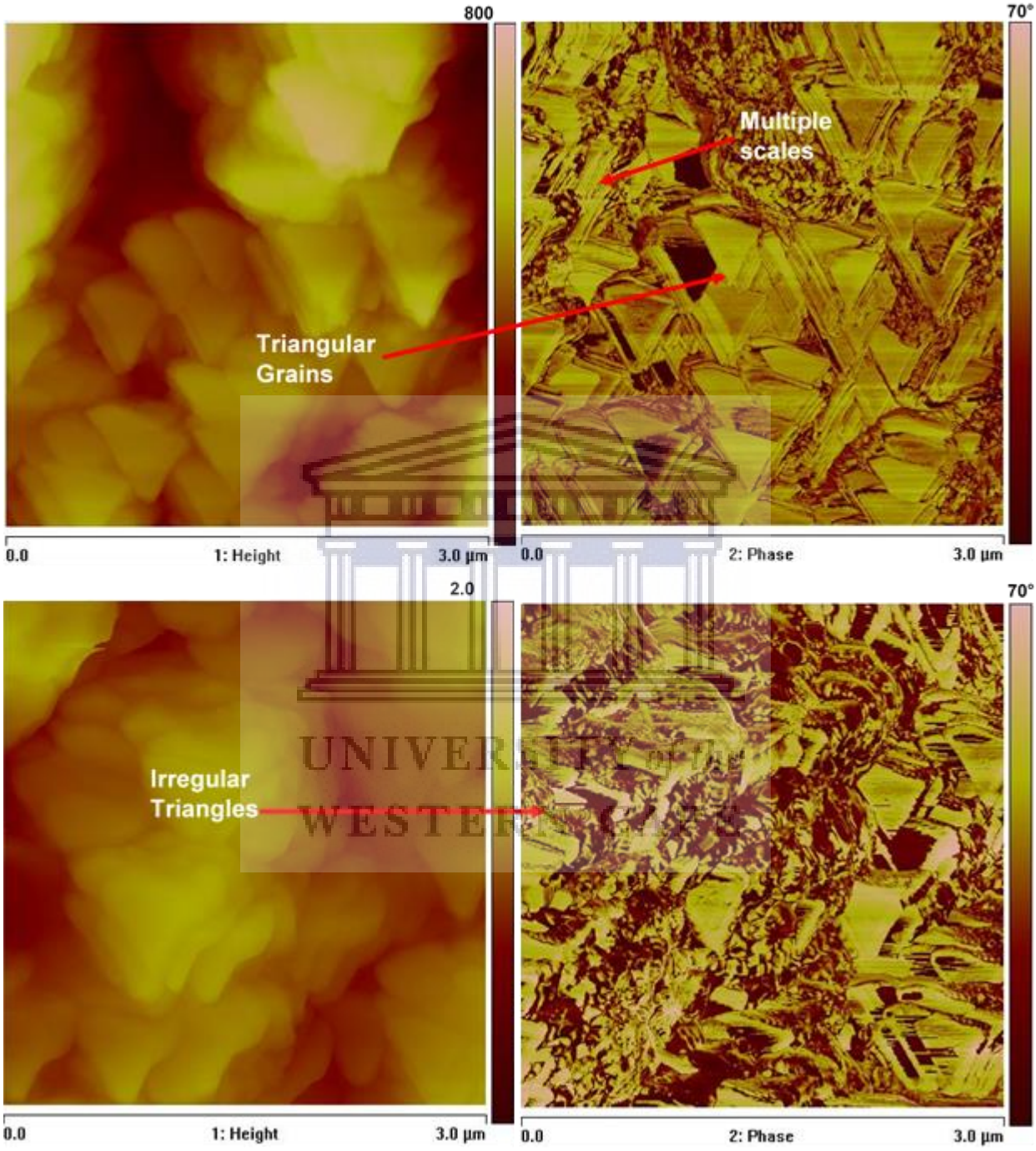


**Figure 7.6**: AFM topographical images of the (a-b) 700 and (c-d) air cooled 800 °C-annealed powders.

http://etd.uwc.ac.za/

The prismatic triangular $TiO_{2-x}N_x$ grains developed upon annealing at 700 °C are shown in **Fig. 7.6a-b**. These grains are stacked in a multiple layered structure **(Fig. 7.6a)**. In **Fig. 7.6b,** the two-phase structure displays ultrafine particles located between the triangular grains. The AFM images of the air cooled 800 °C-annealed Ti powder in **Fig. 7.6c-d** revealed that the multi-layered grains have lost the original triangular shape. These AFM images agree with the SEM analysis of the oxide film in **Fig. 7.5a**. The surface film lost its triangular shape due to increased annealing temperature that resulted in higher concentration of nitrogen content in the $TiO_{2-x}N_x$ phase. The oxynitriding is intensive at 800 °C leading to formation of surface layer based on rutile $TiO_2$ phase, however the oxynitriding temperature in Ti alloys might be higher than that of CP Ti **[32]**. In pure Ti powder, 700 and 800 °C is sufficient to induce similar surface oxynitride layer. Annealing at high temperatures such as 700 and 800 °C reduces the $TiO_2$ (110) surface while creating point defects in the rows of bridging O atoms leading to O vacancies which get occupied by N atoms **[33]**. Even if the stable rutile $TiO_2$ and FCC TiN forms or $TiO_2$−TiN interface during annealing, there will be an exchange of N and O in the interface region to promote titanium oxynitride **[34]**.

UNIVERSITY of the
WESTERN CAPE

**Table 7.1**: Density and lattice parameters.

| Material | Density (g/cm$^3$) | Current Density (g/cm$^3$) |
|---|---|---|
| **TiN** | 5.4 **[28]**<br>5.39 **[29]**<br>5.25 **[30]**<br>5.00 **[31]**<br>5.24 **[32]** | -<br>-<br>-<br>-<br>- |
| **$TiO_{2-x}N_x$ (Rutile-type)** | 4.27 **[28]**<br>4.26 **[26]**<br>4.25 **[33]** | 4.57 ± 0.082 (600 °C),<br>4.58 ± 0.082 (700 °C),<br>4.59 ± 0.082 (800 °C) |
| **TiO** | 4.95 **[26]** | 4.92 ± 0.082 (500 °C) |

UNIVERSITY of the
WESTERN CAPE

**Table 7.1** compares the data reported in literature with the one obtained from the current study. The density for CP Ti was measured at 4.48 g/cm$^3$ which increased to 4.92 ± 0.089 g/cm$^3$ upon annealing at 500 °C. According to literature, the density obtained for the 500 °C-annealed sample corresponds with the density of the $TiO_x$ compound **[35].** A decrease in the density from 4.92 ± 0.089 (500 °C) to 4.57 ± 0.082 g/cm$^3$ was recorded on the 600 °C-annealed sample attributable to phase transformation in the powder particles. After annealing at 700 and 800 °C, the powder densities remained relatively constant at 4.58 ± 0.072 g/cm$^3$ and 4.59 ± 0.085 g/cm$^3$. These density measurements ruled out the possibility of TiN formation since the density of TiN should be ~ 5.0 to 5.4 g/cm$^3$ as confirmed in **Table 7.1**. Based on the EDS analysis, it seems N atoms occupied some O interstitial vacancies taking advantage of atomic vibrations during high temperature diffusion defined by the Fick's law in **Eq 5**.

$$J = -D\frac{\Delta c}{\Delta x} \quad (5)$$

http://etd.uwc.ac.za/

*J* is the flux of atoms, D is the diffusion coefficient, Δc/Δx is the concentration gradient **[27]**. An increase in the annealing temperature provide energy for N to occupy some O interstitial sites thus forming $TiO_{2x}N_x$.

*Thermal analysis of the powders*

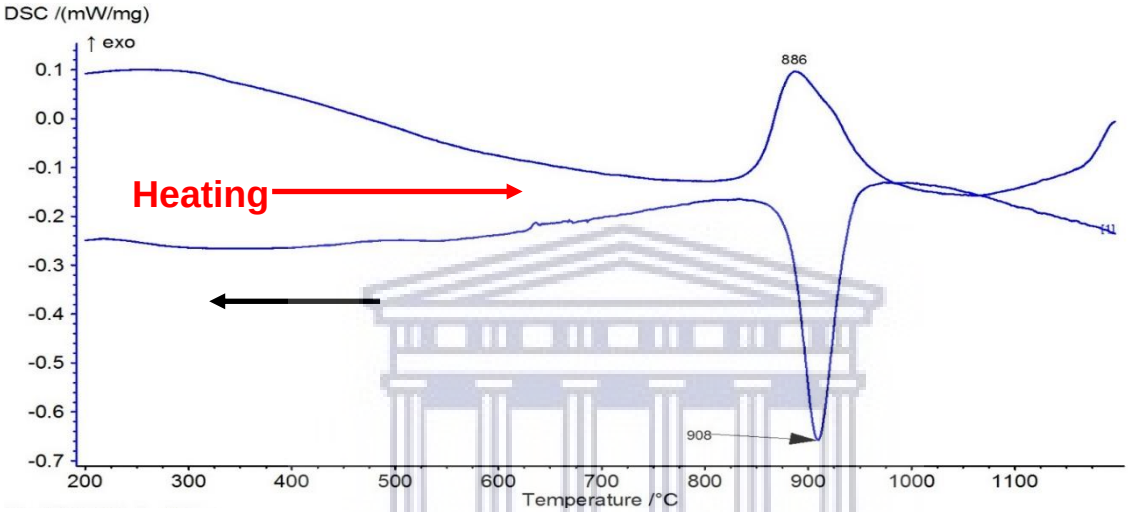


**Figure 7.7**: DSC analysis of the CP Ti powder

UNIVERSITY of the
WESTERN CAPE

Pure HCP Ti (α) structure undergoes a phase transformation at ~882 °C to BCC (β) crystal structure. The DSC curve in **Fig. 7.7** illustrates a reversible α↔β phase transformation in pure Ti powder. Upon heating Ti with HCP structure, an endothermic peak associated with the phase transformation (α to β) emerges at ~883 °C and reaches its maximum at 908 °C. This β-phase reverts to α-phase when cooled down from high temperature past the β transus temperature. A shallow peak like in previous studies **[25]** confirms the reversibility.

http://etd.uwc.ac.za/

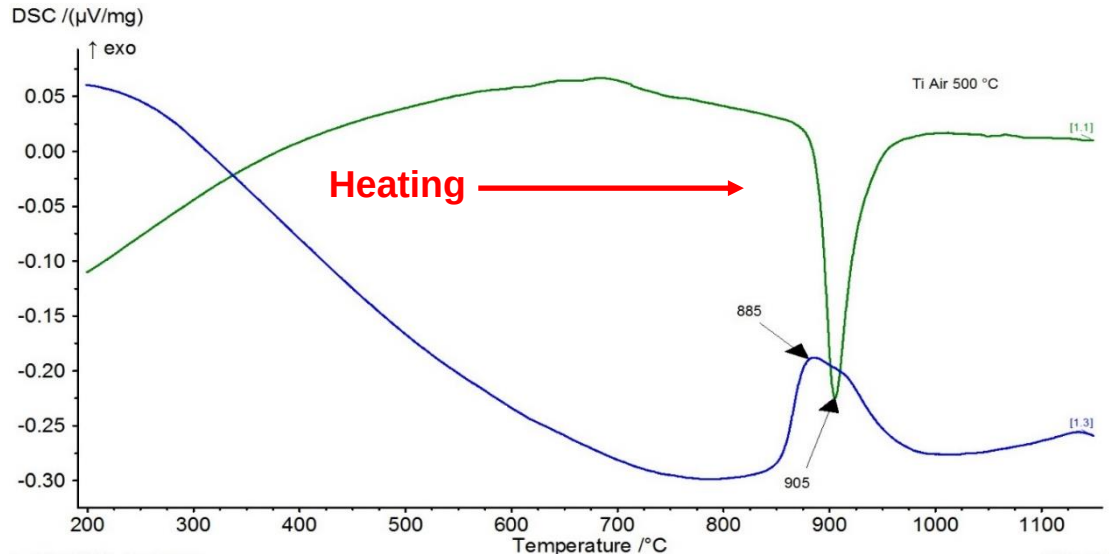


**Figure 7.8**: DSC analysis of CP Ti powder annealed at 500 °C for 2 hours.

Diffusion of oxygen/nitrogen molecules promotes the exothermic reaction denoted by the peak when exposed to high temperature **[25]**. The DSC curve of the 500 °C oxidised powder in **(Fig. 7.8)** shows the $\alpha \leftrightarrow \beta$ reversible phase transformation. This $TiO_x$ (blue) powder revealed a sharp endothermic peak on heating and a broader exothermic peak during cooling. The peaks have slightly shifted to the lower temperature. A low intensity pick is also observed at ~ 700 °C due to the exchange of oxygen atoms between pure Ti and $TiO_x$ particles. This implies that pure Ti is mixed with $TiO_x$ ($Ti/TiO_x$).

UNIVERSITY of the WESTERN CAPE

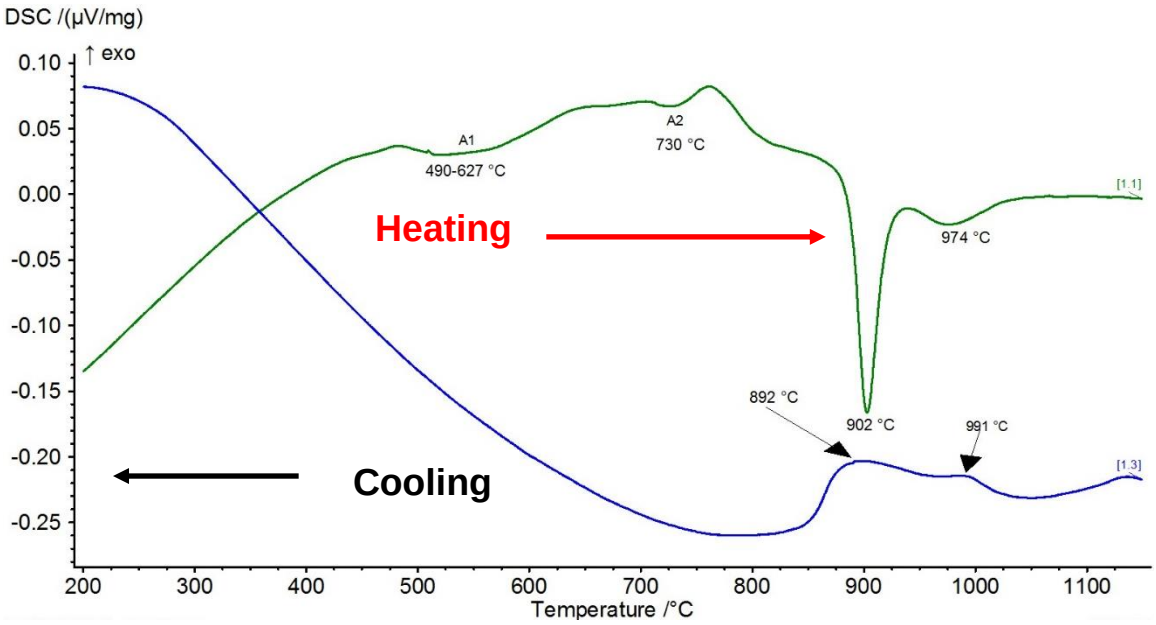


**Figure 7.9**: DSC analysis of the CP Ti powder annealed at 600 °C for 2 hours.

There are two reactions that were observed upon heating: A1 (490-627 °C) and A2 (~730 °C) displaying small endothermic peaks **(Fig. 7.9)**. This behaviour is attributed to $TiO_x$ ($x \leq 2$) and $TiO_2$ particles as detected by the XRD analysis. The behaviour represents the $Ti/TiO_x/TiO_2$ exchange in oxygen atoms. The exchange in oxygen atoms between Ti and $TiO_2$ has been studied **[35, 42]**. At 902 °C, $\alpha \rightarrow \beta$ endothermic peak emerged which was reversible upon cooling at ~892 °C. Another endothermic peak at 974 °C as well as an exothermic peak at 991 °C are due to small nitrogen content. It has been shown that $TiO_x$ phase can take different crystal structure depending on the processing. This phase can stabilize as FCC **[43]**, monoclinic **[35]** or HCP phase obtained in the current investigation.

UNIVERSITY of the WESTERN CAPE

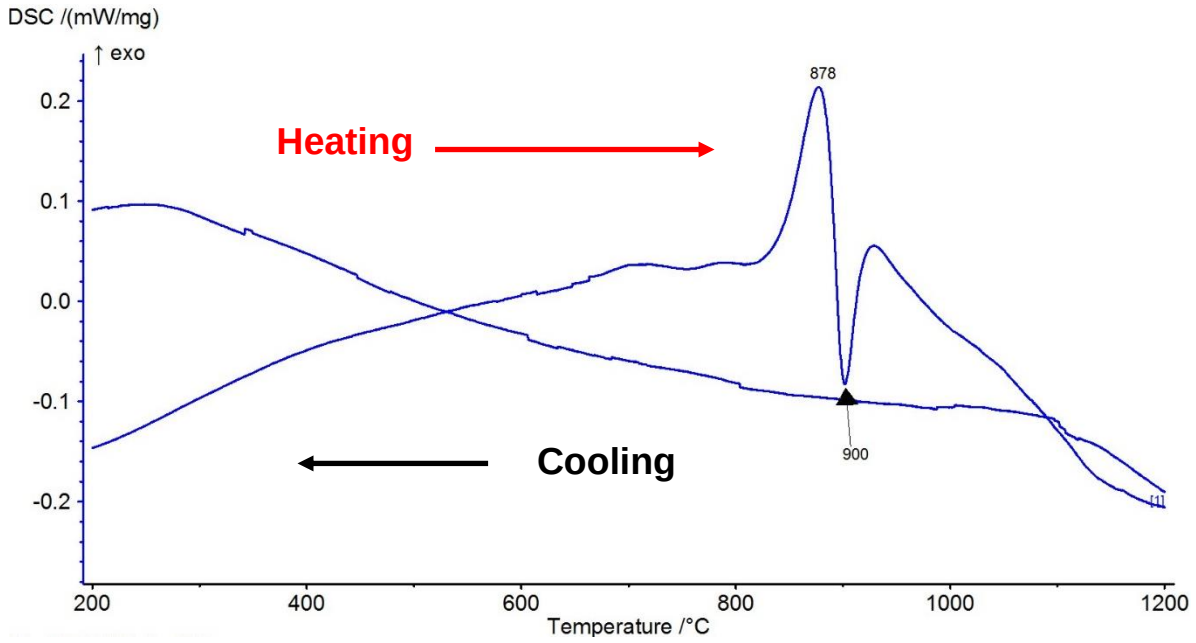


**Figure 7.10**: DSC analysis of CP Ti powder annealed at 700 °C for 2 hours.

According to the XRD analysis **(Fig. 7.1)**, the rutile-type oxynitride phase ($TiO_{2-x}N_x$) phase was detected upon annealing at 700 °C with few $TiO_x$ XRD peaks. **Fig. 7.10** reveals an exothermic peak at 878 °C instead of endothermic peak due to decomposition of the non-stoichiometric $TiO_{2-x}N_x$ overlapping with the endothermic peak at 900 °C. The endothermic peak is due to ionic reactions between the $TiO_x/TiO_2$ and $TiO_{2-x}N_x$ phases. This powder does not show a reversible phase transformation upon cooling signifying the conversion of pure Ti into ceramic powder.

UNIVERSITY of the WESTERN CAPE

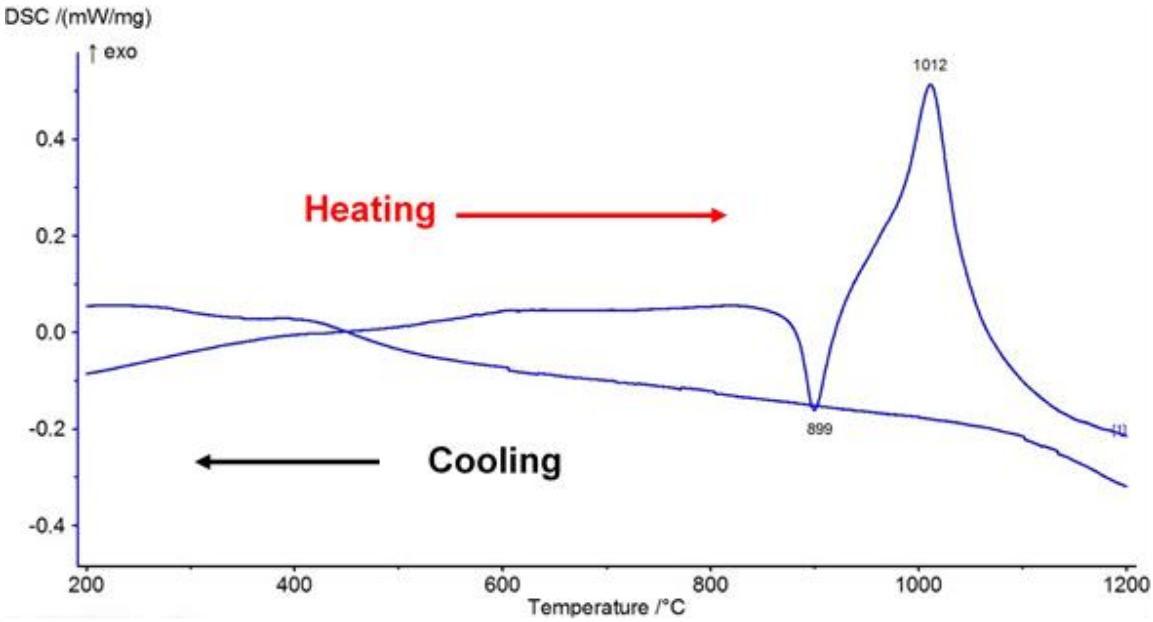


**Figure 7.11**: DSC analysis of CP Ti powder annealed at 800 °C for 2 hours.

The 800 °C-annealed sample shows overlapping DSC peaks. However, the endothermic transformation peak was the first to emerge at 899 °C followed by the exothermic decomposition peak at 1012 °C. This behaviour confirm that the oxygen atomic exchange depends on the concentrations of $TiO_{2-x}N_x$ and $TiO_x$ phases (**Fig. 7.10** and **Fig. 7.11)**. This behaviour might be due to higher amount of N content compared to the 700 C annealed powder which led to better structural stability of the $TiO_{2-x}N_x$ phase.

UNIVERSITY of the WESTERN CAPE

## 7.4 Conclusion

Oxidation of the spherical Ti particles conducted in air was investigated at 500, 600, 700 and 800 °C. Hexagonal closed packed (HCP) $TiO_x$ film has developed after annealing at 500 °C while $TiO_2$ transformation started to emerge at 600 °C. The density of the powder was measured 4.91 g/cm$^3$ for 500 °C-annealed sample which corresponded with the density of the HCP $TiO_x$ phase. For 700 and 800 °C samples, the $TiO_2$/$TiO_{2-x}N_x$ phases

were formed. Despite the formation of the oxide layers on the 500 and 600 °C annealed Ti samples, the powder showed $\alpha \leftrightarrow \beta$ phase transformation. On contrary, the 700 and 800 °C-annealed powders revealed an exothermic peak overlapping with the endothermic peak and the endothermic peak overlapping with exothermic peak, respectively. The powder did not yield a reversible phase transition. This behaviour was due to the exchange in oxygen atoms between the non-stoichiometric $TiO_x$ and $TiO_{2-x}N_x$ phases and determined by the N/O contents. The AFM images illustrated that when the N content increases (800 °C-annealed sample) the powder lost its triangular grains (700 °C-annealed sample) and became irregular shaped grains.

**References**

7.1 D. Švadlák, J. Shánˇelová, J. Málek, L.A. Pérez-Maqueda, J.M. Criado, T. Mitsuhashi, Nanocrystallization of anatase in amorphous $TiO_2$. Thermochimica Acta, 414 (2004)137–143.

UNIVERSITY of the
WESTERN CAPE

7.2 M. Wagemaker, W. J. H. Borghols, F. M. Mulder, Large Impact of Particle Size on Insertion Reactions. A Case for Anatase $Li_xTiO_2$. J. American Cheml Soc, 129 (2007) 4323−4327.

7.3 X. Chen, S.S. Mao, Titanium dioxide nanomaterials: Synthesis, properties, modifications and applications. Chem Rev. 107 (2007) 2891–2959.

7.4 X. Su, Q. Wu, X.Zhan, J. Wu, S. Wei, Z. Guo, Advanced titania nano-structures and composites for lithium ion battery. J. Mater Sci, 47 (2012) 2519–2534.

7.5 X. Song, D. Gopireddy, C.G. Takoudis, Characterization of titanium oxynitride films deposited by low pressure chemical vapor deposition using amide Ti precursor, Thin Solid Films 516 (2008) 6330–6335.

http://etd.uwc.ac.za/

7.6 N.D. Cuong, D.-J. Kim, B.-D. Kang, C.S. Kim, S.-G. Yoon, Analysis of nitrogen species in titanium oxynitride ALD films, Microelectron. Reliab.47 (2007) 752–754.

7.7 C. Nunes, V. Teixeira, M.L. Prates, N.P. Barradas, A.D. Sequeira, Graded selective coatings based on chromium and titanium oxynitride, Thin Solid Films 442 (2003) 173–178.

7.8 R. Escobar-Galindoa, E. Guillénb, I. Herasc, G. Rincón-Llorented, M. Alcón-Camase, F. Lungwitzf, F. Munnikf, E. Schumannf, I. Azkonag, M. Krausef, Design of high-temperature solar-selective coatings based on aluminium titanium oxynitrides $Al_yTi_{1-y}(O_xN_{1-x})$. Part 2: Experimental validation and durability tests at high temperature, Solar Energy Mater Solar Cells 185 (2018) 183–191.

7.9 F. Maury, F.-D. Duminica, TiOxNy coatings grown by atmospheric pressure metal organic chemical vapor deposition, Surf. Coat. Technol. 205 (2010) 1287–1293.

7.10 J. Koerner, L.A. Butterworth, I.V. Mayer, R. Dasbach, H.J. Busscher, Bacterial adhesion to titanium-oxy-nitride (TiNOX) coatings with different resistivities: a novel approach for the development of biomaterials, Biomater. 23 (2002) 2835–2840.

7.11 J.M. Chappé, N. Martin, G. Terwagne, J. Lintymer, J. Gavoille, J. Takadoum, Water as reactive gas to prepare titanium oxynitride thin films by reactive sputtering. Thin Solid Films, 440 (2003) 66–73.

7.12 R. Asahi, T. Morikawa, T. Ohwaki, K. Aoki, Y. Taga, Visible-light photocatalysis in nitrogen- doped titanium oxides. Science, 293 (2001) 269–271.

7.13 S. Piscanec, L.C. Ciacchi, E. Vesselli, G. Comelli, O. Sbaizero, S. Meriani, A. De Vita, Bioactivity of TiN-coated titanium implants, Acta Mater. 52 (2004) 1237-1245.

UNIVERSITY of the WESTERN CAPE

7.14 I. Seki, S. Yamaura, Reduction of Titanium Dioxide to Metallic Titanium by Nitridization and Thermal Decomposition. Mater. Trans. 58 (3) (2017) 361-363.

7.15 O.I. Yaskiv, I.M. Pohrelyuk, V.M. Fedirko, D.B. Lee, O.V. Tkachuk, Formation of oxynitrides on titanium alloys by gas diffusion treatment, Thin Solid Films 519 (2011) 6508–6514.

7.16 A.S. Bolokang, Z.P. Tshabalala, G.F. Malgas, I. Kortidis, H.C. Swart, D.E. Motaung, Room temperature ferromagnetism and $CH_4$ gas sensing of titanium oxynitride induced by milling and annealing, Mater. Chem. Phys. 193 (2017) 512-523.

7.17 M. Arunachalam, G. Yun, K-S. Ahn, W-S. Seo, D.S. Jung, S. H. Kang, Unique photoelectrochemical behavior of TiO2 nanorods wrapped with novel titanium Oxy-Nitride (TiOxNy) nanoparticles, Int. J. hydro. energy 43 (2018) 16458-16467.

7.18 Z. Yu, H. Xua, G. Zhu, D. Yan, A. Yu, Lithium titanium oxynitride thin film with enhanced lithium storage and rate capability, Appl. Surf. Sci. 368 (2016) 173–176.

7.19 A.S. Bolokang, D.E. Motaung, C.J. Arendse, T.F.G. Muller, Production of titanium–tin alloy powder by ball milling: Formation of titanium–tin oxynitride composite powder produced by annealing in air, J. Alloys Compd. 622 (2015) 824–830.

7.20 R. L. Porto, R. Frappiera, J.B. Ducrosa, C. Auchera, H. Mosqueda, S. Chenu, B. Chavillon, F. Tessier, F. Chevire, T. Brousse, Titanium and vanadium oxynitride powders as pseudo-capacitive materials for electrochemical capacitors, Electrochimica Acta 82 (2012) 257– 262.

7.21 L. Li, Y. Zhao, K. Sun, H. Ji, D. Feng, Z. Li, Composition, microstructure and mechanical properties of cBN-based composites sintered with AlN-Al-Ni binder, Ceram. Int. 44 (2018) 16915–16922.

UNIVERSITY of the WESTERN CAPE

7.22 S. Sharma, T. Nanda, O.P. Pandey, Effect of particle size on dry sliding wear behaviour of sillimanite reinforced aluminium matrix composites, Ceram. Int. 44 (2018) 104–114.

7.23 E. Ghasali, A. Pakseresht, A. Rahbari, H. Eslami-shahed, M. Alizadeh, T. Ebadzadeh, Mechanical properties and microstructure characterization of spark plasma and conventional sintering of Al-SiC-TiC composites, J. Alloy. Compd. 666 (2016) 366–371,

7.24 H.H. Nersisyan, B.U. Yoo, Y.M. Kim, H.T. Son, K.Y. Lee, J.H. Lee, Gas-phase supported rapid manufacturing of Ti-6Al-4V alloy spherical particles for 3D printing, Chem. Eng. J. 304 (2016) 232–240.

7.25 A.S. Bolokang, M.J. Phasha, Formation of titanium nitride produced from nanocrystalline titanium powder under nitrogen atmosphere, Int. J. Refract. Met. Hard. Mater. 28 (2010) 610–615.

7.26 A.S. Bolokang, D.E. Motaung, C.J. Arendse, T.F.G. Muller, Morphology and structural development of reduced anatase-$TiO_2$ by pure Ti powder upon annealing and nitridation: Synthesis of $TiO_x$ and $TiO_xN_y$ powders. Mater. Charact. 100 (2015) 41–49.

7.27 D.R. Askeland, The Science and Engineering of Materials, Third S.I. Edition, Stanley Thornes Publishers Ltd, United Kingdom, pp. 111-133.

7.28 D. Choi, P.N. Kumta, Nanocrystalline TiN Derived by a Two-Step Halide Approach for Electrochemical Capacitors. J. Electrochem Soc, 153 (2006) A2298-A2303.

7.29 B.M. Moshtaghioun, D. Gómez-García, A. Domínguez-Rodríguez, Spark plasma sintering of titanium nitride in nitrogen: Does it affect the sinterability and the mechanical properties? J. Euro. Ceram. Soc. 38 (2018) 1190–1196.

UNIVERSITY of the WESTERN CAPE

7.30 M. Drygas´, C. Czosnek, R.T. Paine, J.F. Janik, Two-Stage Aerosol Synthesis of Titanium Nitride TiN and Titanium Oxynitride $TiO_xN_y$ Nanopowders of Spherical Particle Morphology. Chem. Mater. 18 (2006)3122-3129.

7.31 C. Marinescu, A. Sofronia, C. Rusti, R. Piticescu, V. Badilita, E. Vasile, R. Baies, S.Tanasescu, DSC investigation of nanocrystalline $TiO_2$ powder. J. Therm. Anal Calorimetry, 103 (2011) 49–57.

7.32 X. Yang, C. Li, B. Yang, W. Wang, Y. Qian, Optical properties of titanium oxynitride nanocrystals synthesized via a thermal liquid–solid metathesis reaction. Chem. Phys. Lett. 383 (2004) 502–506.

7.33 A.S. Bolokang, D.E. Motaung, C.J. Arendse, T.F.G. Muller, Formation of face-centered cubic and tetragonal titanium oxynitride by low temperature annealing of ball milled titanium powder in air. Adv. Pow. Technol. 26 (2015) 169–174.

7.34 Y. Lin, D. Zou, X. Chen, M. Qiu, H. Kameyama, Y. Fan, Low temperature sintering preparation of high-permeability $TiO_2$/Ti composite membrane via facile coating method, Appl. Surf. Sci. 349 (2015) 8–16.

7.35 L. Zhu, Y. Zhang, T. Hu, P. Leicht, Y. Liu, Oxidation resistance and thermal stability of Ti(C,N) and Ti(C,N,O) coatings deposited by chemical vapor deposition, Int. J. Refract. Met. Hard Mater. 54 (2016) 295–303

7.36 M. Jamesh, T.S.N. Sankara Narayanan, P.K. Chu, Thermal oxidation of titanium: Evaluation of corrosion resistance as a function of cooling rate, Mater. Chem. Phys. 138 (2013) 565-572.

7.37 A.M. Limarga, D.S. Wilkinson, A model for the effect of creep deformation and intrinsic growth stress on oxide/nitride scale growth rates with application to the nitridation of γ-TiAl, Mater. Sci. Eng. A 415 (2006) 94–103.

UNIVERSITY of the WESTERN CAPE

http://etd.uwc.ac.za/

7.38 R. German, Powder Metallurgy Science. Princeton, New Jersey, USA: Metal Powder Industry Federation; 1994. p. 451–5.

7.39 B. Avar, S. Ozcan, Structural evolutions in Ti and $TiO_2$ powders by ball milling and subsequent heat treatments, Ceram. Int. 40 (2014) 11123–11130.

7.40 A.S. Bolokang, D.E.Motaung, C.J. Arendse, T.F.G. Muller, Morphology and structural development of reduced anatase-$TiO_2$ by pure Ti powder upon annealing and nitridation: Synthesis of $TiO_x$ and $TiO_xN_y$ powders, Materials Characterization 100 (2015) 41–49.

UNIVERSITY of the
WESTERN CAPE

http://etd.uwc.ac.za/

# CHAPTER EIGHT

## The A356-1Sn-5Ni-($TiO_{2-x}N_x$) ceramic composite developed at low temperatures

*Paper submitted for peer review*


### Abstract

A ceramic composite material of A356-1Sn-5Ni-($TiO_{2-x}$-$N_x$) composition was developed. The $TiO_{2-x}$-$N_x$ ceramic particles were bonded without forming any intermetallic particles such as $Al_3Ti$ with Ti. The structural analysis showed that a tetragonal $TiO_{2-x}N_x$ with lattice parameters a=4.585 Å; c=2.960 Å, HCP $TiO_x$ phase with lattice parameters a=5.140 Å c=9.480 Å and FCC phase with lattice parameter a=5.572 Å were formed.


**Keywords**; A356-Sn-Ni; $TiO_{2-x}$-$N_x$; Ceramic particles; Binder.

UNIVERSITY of the
WESTERN CAPE

### 8.1 Introduction

Titania ($TiO_2$) is a well-known mineral that occurs in three phases: rutile, anatase, and brookite, each having different crystal structures. It is widely used in the electronics, ceramics, medicine, chemical, energy (solar), environmental applications and pigment industries **[1, 2]**. Titanium nitride (TiN) on the other hand is a technological strategic coating material due to its excellent chemical stability and excellent tribological properties **[3]**. $TiO_2$ and TiN accept N and O atoms, respectively, occupying interstitial positions at high temperatures to form titanium oxynitride, ($TiO_xN_y$), another important class of material. The oxygen rich $TiO_xN_y$ films are used as thin film resistors **[3]** and solar

http://etd.uwc.ac.za/

selective collectors **[4]** while the nitrogen-rich $TiO_xN_y$ films are used as anti-reflective coatings **[5]** and biomaterials coated stents with a better clinical performance compared to uncoated stainless steel stents **[6]**. As stated previously, Titanium oxynitrides is an important class of materials. Formation of oxynitrides on titanium alloys is achieved by different techniques, which include gas diffusion treatment during annealing **[7]**, chemical process **[8]** and radio frequency magnetron sputtering deposition **[9]**. The feasibility of mixed metal titanium oxynitride has been extensively explored for various applications **[9]**. The binder system is a common way of producing ceramic nitrides and/or oxynitrides. Sintering of cBN-based composites with AlN-Al-Ni as a binder produced outstanding mechanical properties with acceptable flexural strength, fracture toughness, hardness, and abrasiveness **[10]**. Ni is also a binder that is ferromagnetic and capable of transforming at high temperatures or under mechanical deformations **[11]**. The rate of oxide and subsequently oxynitride layer deposition is determined by the metal's affinity to O or N atoms at a particular temperature. In our recent publication, we reported on thermal analysis of the spherical Ti particles before and after surface contamination **[12]**. In the current investigation, a low melting temperature binder composed of A356-1Sn-5Ni was mixed with $TiO_{2-x}$-$N_x$ ceramic particles to develop a composite material.

UNIVERSITY of the
WESTERN CAPE

### 8.2 Experimental Details

The pre-synthesized (chapter seven) $TiO_{2-x}$-$N_x$ powders were mixed with A356, Sn and Ni powders followed by compaction at 200 MPa. The compacts were sintered at 700 and 800 ºC, respectively for 6 hours. The microstructure of the polished A356-1Sn-5Ni-($TiO_{2-x}$-$N_x$) ceramic composite was investigated using a high-resolution scanning electron microscope (HR-SEM, Auriga ZEISS) coupled with a Robinson Backscatter Electron Detector and an Oxford Link Pentafet energy dispersive x-ray spectroscopy (EDS)

http://etd.uwc.ac.za/

detector. Phase evolution was determined with the use of a PANalytical X'pert PRO PW 3040/60 X-ray diffraction (XRD) machine, using Cu $K_\alpha$ radiation as source.

### 8.3 Results and Discussion

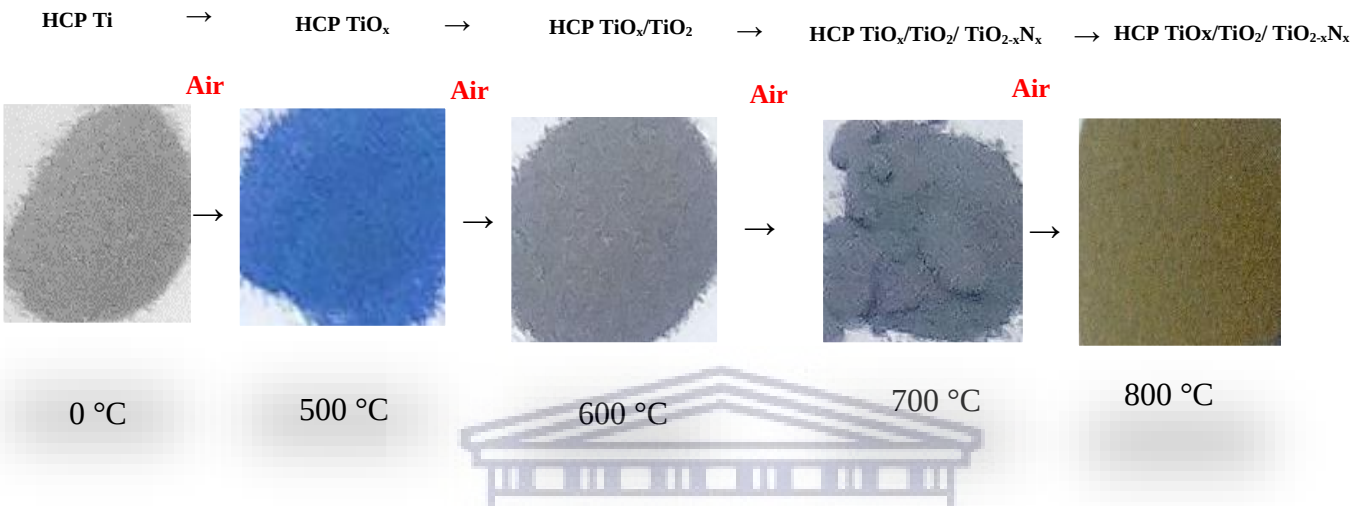


**Figure 8.1**: Oxynitride formation progression during annealing of spherical Ti powder

Fig. 8.1 shows images of Ti powders annealed at different temperatures in air. Ti has high affinity for interstitial O, N, H and C. More than one interstitial element such as O and N react with Ti powder to form oxynitride. The process to produce oxynitride powders was explored in the previous study which showed $TiO_{2-x}N_x$ layer on the spherical Ti particles surfaces at 700 and 800 °C **[12]**. These powders are potential reinforcements for manufacturing of metal matrix composites (MMCs) whereby a ductile or low melting temperature matrix binds the ceramic particles. The 700 and 800 °C annealed $TiO_{2-x}N_x$ powders were added to A356-Sn-Ni binder to produce A356-Sn-Ni ($TiO_{2-x}N_x$) composites.

UNIVERSITY of the WESTERN CAPE

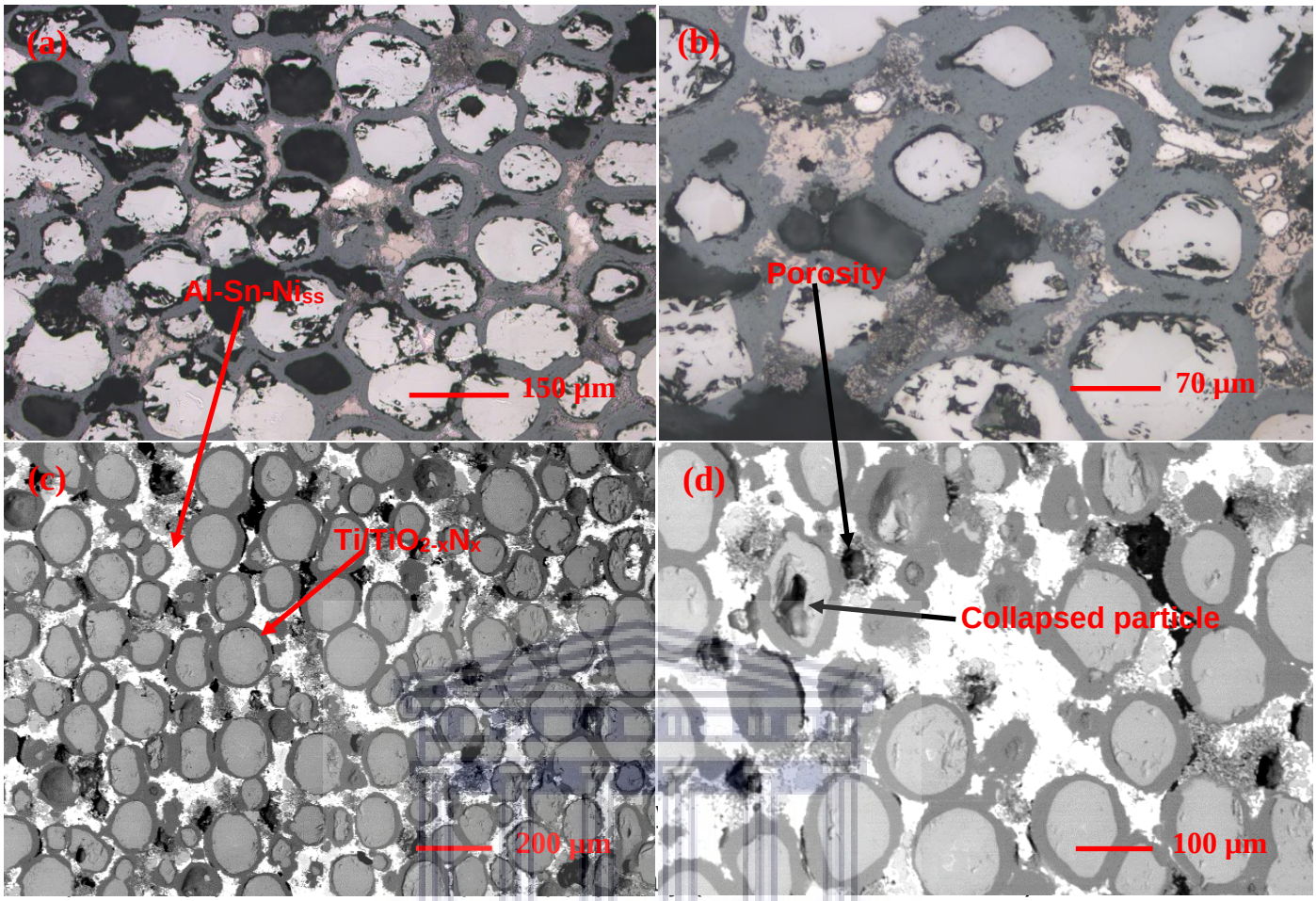


**Figure 8.2**: Optical and SEM images of the (a & c) 700 °C (b & d) 800 °C sintered A356-1Sn-5Ni-($TiO_{2-x}N_x$) composites.

UNIVERSITY of the
WESTERN CAPE

Fig. 8.2 shows A356-1Sn-5Ni-($TiO_{2-x}N_x$) composite after sintering at 700 and 800 °C respectively. The hard spherical Ti particles coated with a $TiO_{2-x}N_x$ layer are evident in the microstructure as a distinguished dark coating attributed to the reaction with O and N. The 700 ºC samples are shown in Fig. 8.2a and c while the 800 ºC is shown in Fig. 8.2b and d. Some particles were exposed to severe oxidation leading particle collapse. These particles become initiation point of porosity. It is evident that the binder completely wet the spherical particles due to the low melting temperature of Sn and Al. Due to immiscibility between A356 and Sn, the Sn melts and become and the increased diffusion

of the metal improves the kinetics of the reaction. The A356 Al alloy used contained 7% Si, 0.3% Mg, 0.2% Fe (max) and 0.1% Zn (max) as alloying elements. The sintering temperature leads to melting of Sn followed by the A356 alloy and might result in the loss of Mg due to its low vaporization. The optical and SEM microstructures of the A356-1Sn-5Ni-(700°C-$TiO_{2-x}N_x$) composite are presented in Fig. 8.2a and c, while A356-1Sn-5Ni-(800°C-$TiO_{2-x}N_x$) are presented in Fig.8.2b and d. The spherical Ti particles enclosed by the $TiO_{2-x}N_x$ layer are bonded by A356-1Sn-5Ni matrix. The $TiO_{2-x}N_x$ coated particles in Fig. 8.2a and c (700°C) appears less damaged compared to the 800 °C-annealed samples. More collapsed particles are evident in Fig. 8.2d attributed to more content of N and O on the surface layer due to high temperature oxidation. The A356-1Sn-5Ni alloy successfully bonded the ceramic $TiO_{2-x}N_x$ particles through liquid-phase sintering mechanism.

UNIVERSITY of the
WESTERN CAPE

http://etd.uwc.ac.za/

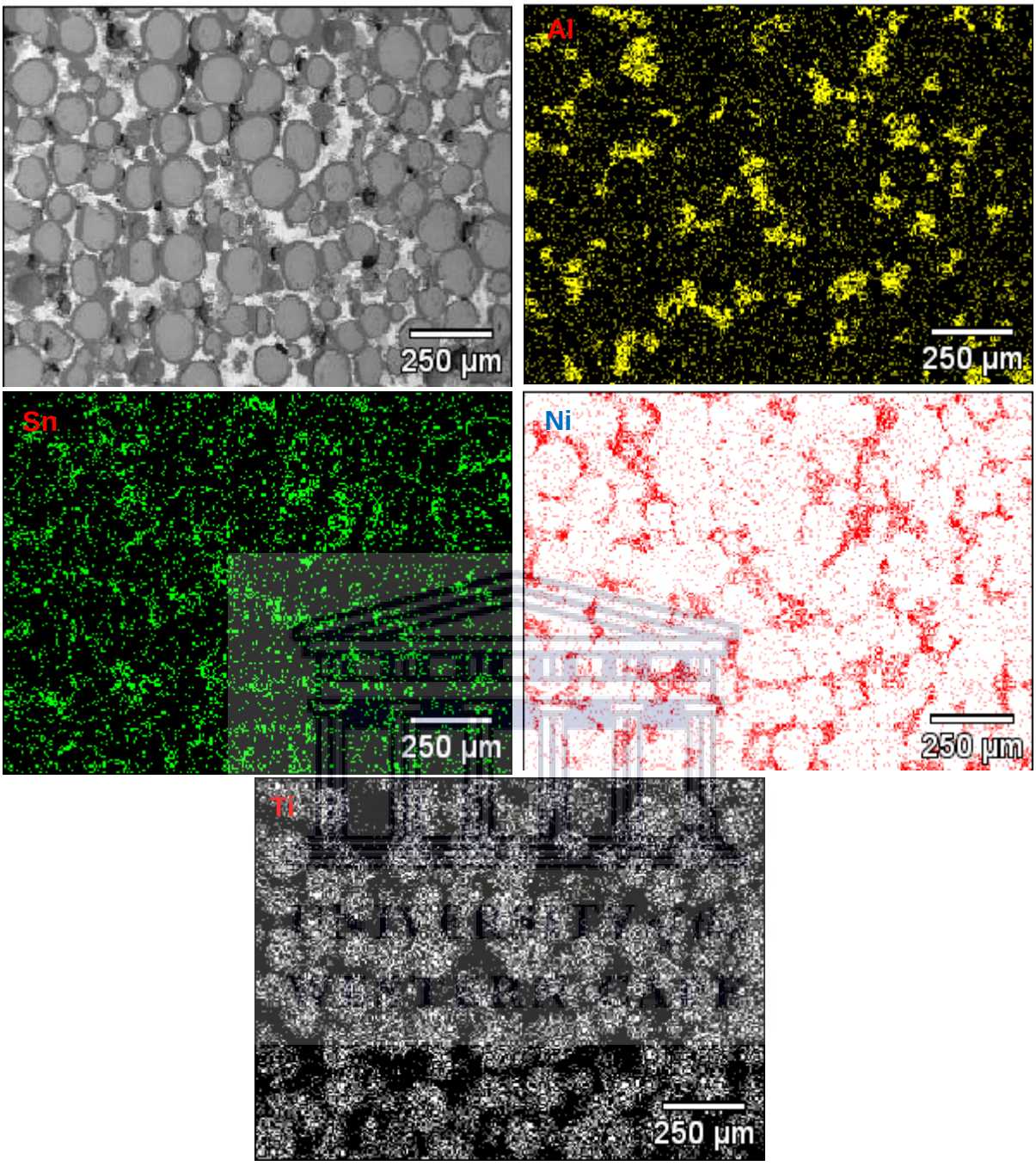


**Figure 8.3**: EDS mapping revealing Al, Ni, Sn and Ti elements.

Fig. 8.3 represents the EDS elemental mapping confirming the presence of Al, Sn, Ti and Ni. The spherical solid particles are Ti. The analysis of O and N was reported in the previous work to produce the $TiO_{2-x}N_x$ coating around the Ti spherical particles **[12]** and can form by simultaneous O and N diffusion during annealing in air **[13]**.

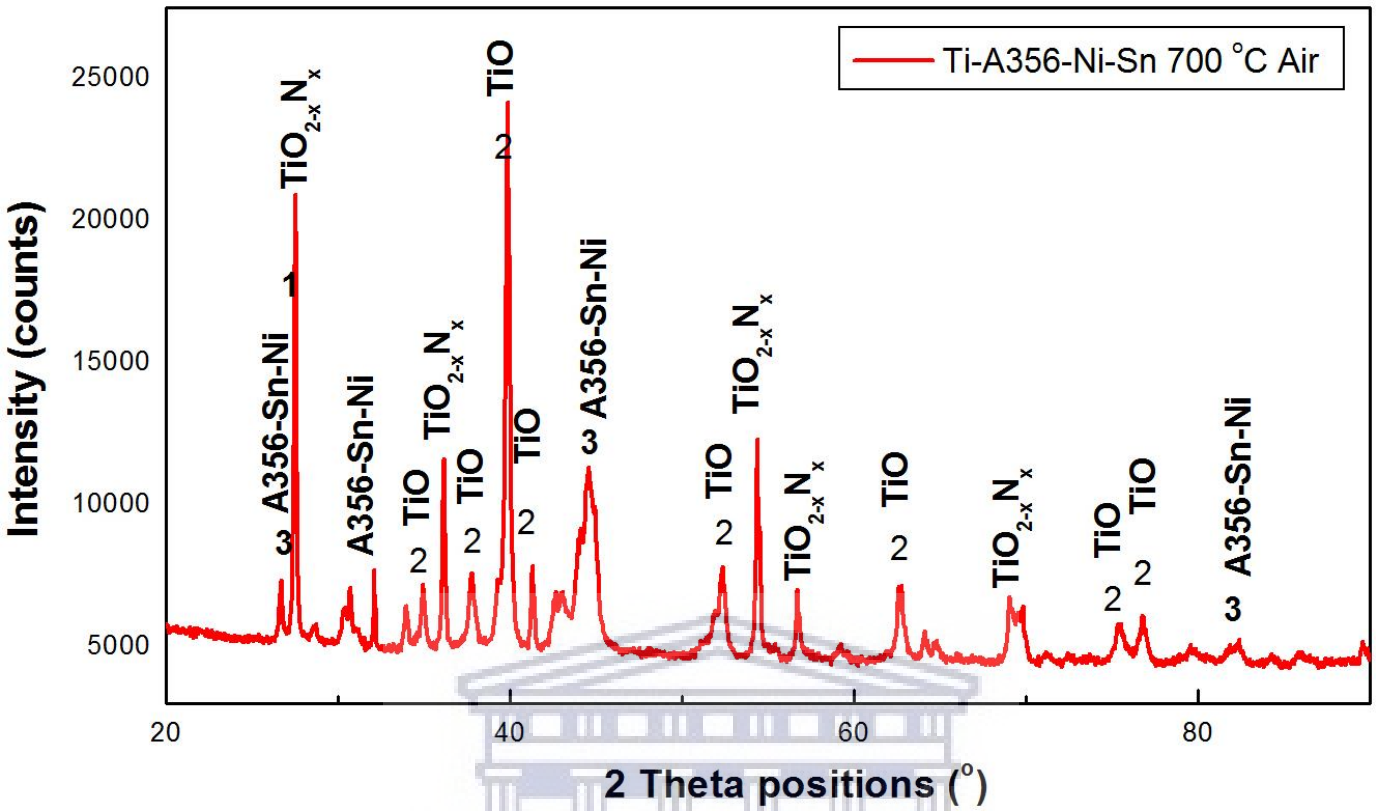


**Figure 8.4**: XRD pattern of the A356-Ni-Si-Ti composite

UNIVERSITY of the
WESTERN CAPE

The microstructure of the ceramic A356-1Sn-5Ni-(800 °C-$TiO_{2-x}N_x$) composite revealed three-phase structure; a tetragonal, HCP and FCC. Tetragonal $TiO_{2-x}N_x$ phase was detected with lattice parameters a=4.585 Å; c=2.960 Å. This crystal structure is similar to those obtained after powder annealing attesting to the structural stability of the ceramic layer on the Ti powder particle after annealing. The binder is comprised of the FCC phase with lattice parameter a=5.572 Å. Moreover, minor peaks of HCP $TiO_x$ phase was detected with lattice parameters a=5.140 Å c=9.480 Å. Normal thermodynamic reaction of Al-rich and Ni alloys results in the formation of an orthorhombic $Al_3Ni$ intermetallic phase also confirmed by microstructures **[14]**. In the current reaction, no $Al_3Ni$ intermetallic phase was detected which implies that the $TiO_{2-x}N_x$ coating inhibited the

reaction to occur. Therefore, Al matrix wets the ceramic $TiO_{2-x}N_x$ particles to form a composite.

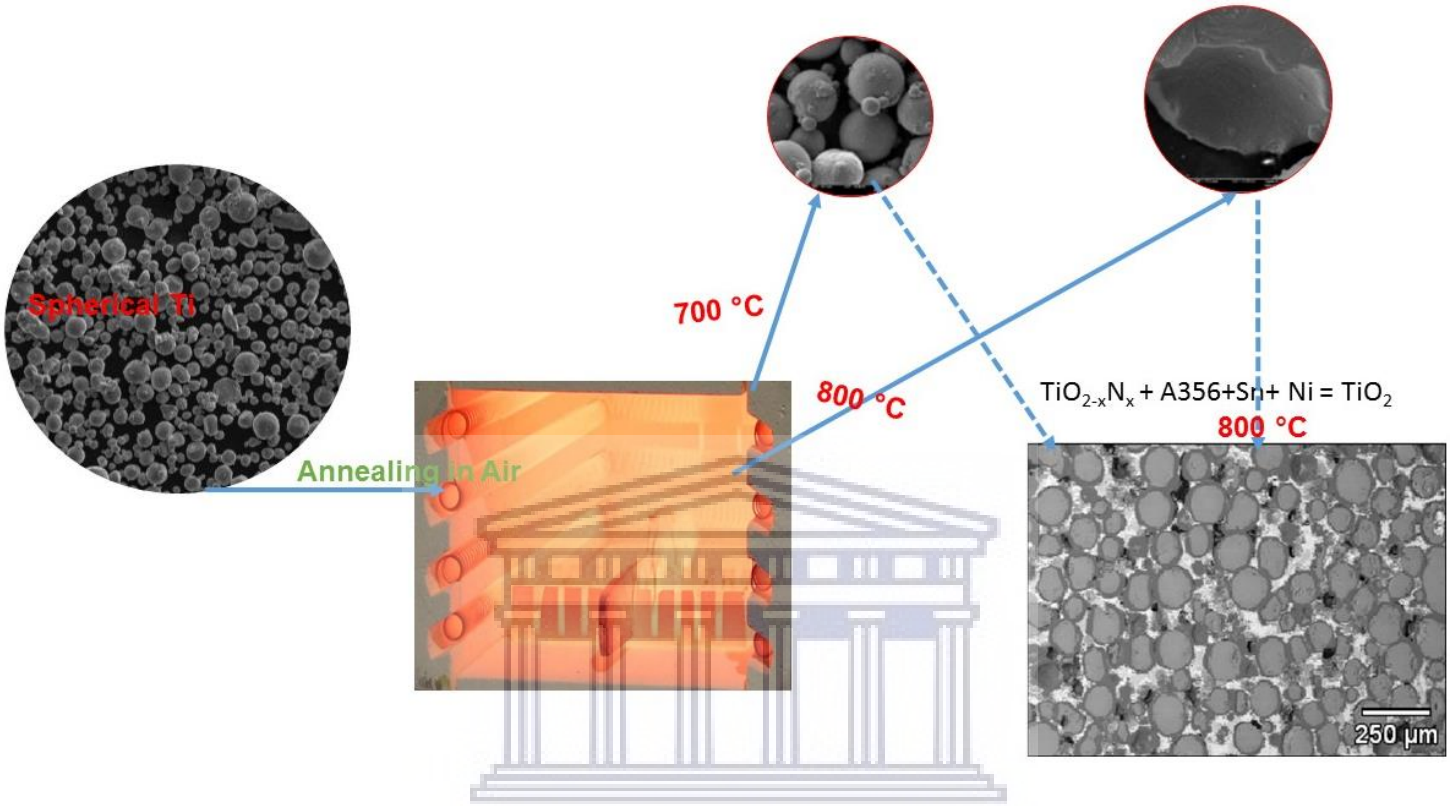


**Figure 8.5**: Formation mechanism of the A356-Sn-Ni-Ti composite

UNIVERSITY of the
WESTERN CAPE

At 700 and 800 °C, the $TiO_{2-x}N_x$ formed by diffusion of N atoms into interstitial positions of Ti particle surfaces. The two $TiO_{2-x}N_x$ products upon annealing at 700°C and 800 °C, were mixed with A356-1Sn-5Ni which acts as a binder to provide liquid transport for wetting of the solid $TiO_{2-x}N_x$ spherical particles. It also provides a surface tension force assisting in densification of the material. A wetting liquid A356-1Sn-5Ni metal makes a small contact angle with solid $TiO_{2-x}N_x$ particles defined by Eq.1 and illustrated in Fig. 8.6.

$$\gamma_{SV} = \gamma_{SL} + \gamma_{LV} Cos\ \theta \qquad (1)$$

Where $\gamma_{sv}$ represents solid-vapour surface energy, $\gamma_{SL}$ is solid-liquid surface energy and θ indicates that liquid will cover the solid particle **[15]**.

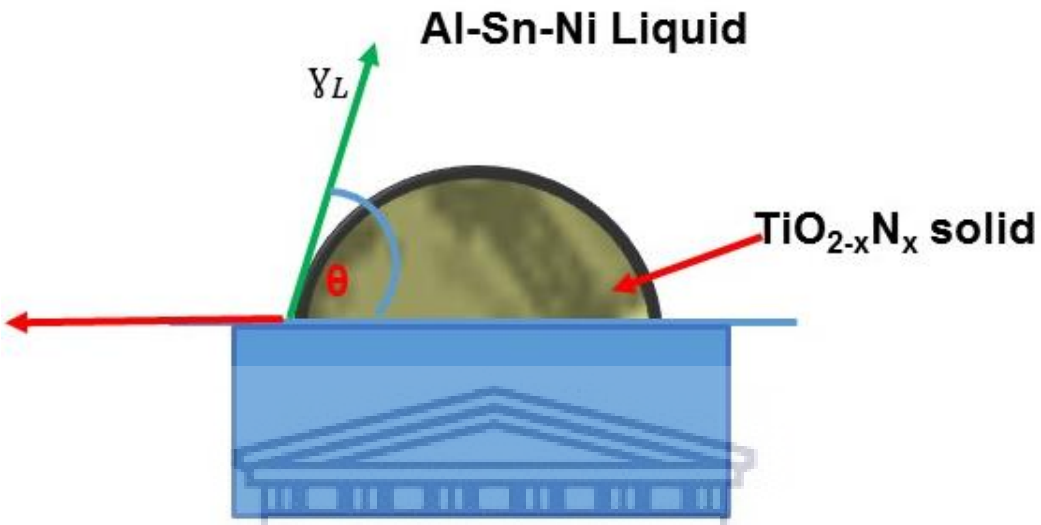


**Figure 8.6**: Illustration of the solid $TiO_{2-x}N_x$ particle wetting by A356-1Sn-5Ni liquid metal.

UNIVERSITY of the
WESTERN CAPE

## 8.4 Conclusion

A metallic binder, A356-1Sn-5Ni was used to bind the spherical $TiO_{2-x}$-$N_x$ coated Ti particles to form a composite. The composite A356-1Sn-5Ni-($TiO_{2-x}$-$N_x$) mixture was sintered at 700 and 800 °C. The structural analysis showed that a tetragonal $TiO_{2-x}N_x$ with lattice parameters a=4.585 Å; c=2.960 Å, HCP $TiO_x$ phase with lattice parameters a=5.140 Å c=9.480 Å and FCC phase with lattice parameter a=5.572 Å were formed.

## References

8.1 D. Švadlák, J. Shán˘elová, J. Málek, L.A. Pérez-Maqueda, J.M. Criado, T. Mitsuhashi, Nanocrystallization of anatase in amorphous $TiO_2$. Thermochimica Acta, 414 (2004)137–143.

http://etd.uwc.ac.za/

8.2 M. Wagemaker, W. J. H. Borghols, F. M. Mulder, Large Impact of Particle Size on Insertion Reactions. A Case for Anatase $Li_xTiO_2$. J. American Cheml Soc, 129 (2007) 4323−4327.

8.3 N.D. Cuong, D.-J. Kim, B.-D. Kang, C.S. Kim, S.-G. Yoon, Analysis of nitrogen species in titanium oxynitride ALD films, Microelectron. Reliab.47 (2007) 752–754.

8.4 C. Nunes, V. Teixeira, M.L. Prates, N.P. Barradas, A.D. Sequeira, Graded selective coatings based on chromium and titanium oxynitride, Thin Solid Films 442 (2003) 173–178.

8.5 F. Maury, F.-D. Duminica, $TiO_xN_y$ coatings grown by atmospheric pressure metal organic chemical vapor deposition, Surf. Coat. Technol. 205 (2010) 1287–1293.

8.6 J. Koerner, L.A. Butterworth, I.V. Mayer, R. Dasbach, H.J. Busscher, Bacterial adhesion to titanium-oxy-nitride ($TiNO_X$) coatings with different resistivities: a novel approach for the development of biomaterials, Biomater. 23 (2002) 2835–2840.

8.7 A.S. Bolokang, Z.P. Tshabalala, G.F. Malgas, I. Kortidis, H.C. Swart, D.E. Motaung, Room temperature ferromagnetism and CH4 gas sensing of titanium oxynitride induced by milling and annealing, Mater. Chem. Phys. 193 (2017) 512-523.

8.8 M. Arunachalam, G. Yun, K-S. Ahn, W-S. Seo, D.S. Jung, S. H. Kang, Unique photoelectrochemical behavior of $TiO_2$ nanorods wrapped with novel titanium Oxy-Nitride ($TiO_xN_y$) nanoparticles, Int. J. hydro. energy 43 (2018) 16458-16467.

8.9 Z. Yu, H. Xua, G. Zhu, D. Yan, A. Yu, Lithium titanium oxynitride thin film with enhanced lithium storage and rate capability, Appl. Surf. Sci. 368 (2016) 173–176.

UNIVERSITY of the WESTERN CAPE

8.10 L. Li, Y. Zhao, K. Sun, H. Ji, D. Feng, Z. Li, Composition, microstructure and mechanical properties of cBN-based composites sintered with AlN-Al-Ni binder, Ceram. Int. 44 (2018) 16915–16922.

8.11 AS Bolokang, MJ Phasha, Thermal analysis on the curie temperature of nanocrystalline Ni produced by ball milling, Advanced Powder Technology 22 (4), 518-521.

8.12 S.T. Camagu, A.S. Bolokang, T.F.G. Muller, D.E.Motaung, C.J. Arendse, Surface characterization and formation mechanism of the ceramic TiO2-xNx spherical powder induced by annealing in air, Powder Technology 351 (2019) 229–237.

8.13 M.N. Mathabathe, G. Govender, C.W. Siyasiya, R.J. Mostert, A.S. Bolokang, Surface characterization of the cyclically oxidized γ-Ti-48Al-2Nb-0.7Cr alloy after nitridation, Materials Characterization 154 (2019) 94–102.

8.14 Z. Gxowa-Penxa, P. Daswa, R. Modiba, M.N. Mathabathe, A.S. Bolokang,

Development and characterization of Al–$Al_3Ni$–Sn metal matrix composite, Materials Chemistry and Physics 259 (2021) 124027.

8.15 O.O. Marenych, A.G. Kostryzhev, Z. Pan, H. Li, S. van Duin, Comparative effect of Mn/Ti solute atoms and TiC/Ni3(Al,Ti) nano-particles on work hardening behaviour in NiCu alloys fabricated by wire arc additive manufacturing, Mater. Sci. Eng. 753 (2019) 262–275.

UNIVERSITY of the WESTERN CAPE

# CHAPTER NINE

# 9.1 CONCLUDING REMARKS AND FUTURE WORK

As per the objectives as set out on section 1.3 for the current research, the following concluding remarks are drawn:

### 9.1.1 Concluding Remarks

***Objective 1:*** To synthesize NiAl alloy via powder consolidation of elemental Ni and Al powders and study the resulting alloy structure.

- Commercially pure Ni and Al powders were blended at 1:1 atomic ratio to obtain a homogeneous mixture, which was cold pressed into cylindrical coupons. Upon sintering followed by air-cooling, the samples exhibited a well-sintered single phase cubic B2-NiAl with equiaxed grain structure with comparable lattice parameters for lower (750 ℃) and higher (1300 ℃) sintering temperatures. The sample sintered at 1300 ℃ was brittle and the product was hand crushed into a powder using a rod and porcelain bowl. Prolonged sintering (48 and 120 h) resulted in recrystallized grains consumed by preferential growth in the <111> orientations as revealed by the Electron Backscatter Diffraction analysis. A thin scale of $Al_2O_3$ was detected upon prolonged (120 h) oxidation in air. The $Al_2O_3$ acted as a protective layer preventing any further bulk oxidation of the sample except for traces of $Al_2O_3$ that formed via intergranular oxidation and transformed into a metastable monoclinic oxynitride phase due N contamination.

***Objective 2:*** To synthesize a TiC reinforced NiAl based alloy and study the resulting composite structure.

UNIVERSITY of the WESTERN CAPE

- The $Ni_{62.5}Al_{37.5}TiC_{1.28}$ composite was developed by powder mixing, compaction and sintering at 650 ºC. The chemical reaction during sintering showed that thermal explosion (TE) occured when small amount of nanosized TiC powder was added. The cold pressing process reduced the activation/ignition temperature of the surface Ni/Al particle interaction, which propagated to the core of the compact. The resultant microstructure revealed martensitic NiAl plates surrounded by the hard $Ni_3Al$ and TiC particles. The formed composite resisted the diamond tool cutting attributable to the work hardening behaviour of the composite. The $Ni_{62.5}Al_{37.5}TiC_{1.28}$ composite has an average hardness of 431±11 HV while the $Ni_{62.5}Al_{37.5}TiC_{1.28}$ is 396±14 HV.

***Objective 3:*** To synthesize a suitable metal oxynitride and study the resulting structure.

- Commercially pure samples of spherical Ti powder were oxidized at 500, 600, 700 and 800 ℃ respectively. Lower temperature oxidation (500 ℃) resulted in the formation of hexagonal close packed $TiO_x$ ($x \leq 2$) while intermediate temperature (600 ℃) oxidation resulted in the formation of $TiO_2$ compared to oxidation at higher temperatures (700 and 800 ℃) whereby $TiO_2/TiO_{2-x}N_x$ phases were detected via X-ray diffraction analysis. Thermal analysis of the samples oxidised at lower temperatures (500 and 600 ℃) revealed $\alpha \leftrightarrow \beta$ phase transformation, which was indicative of the presence of pure titanium. Oxidation at higher temperatures (700 and 800 ℃) yielded no such phase transformation, which meant that the entire titanium had not only oxidised but nitride as well forming a Ti oxynitride via the exchange in oxygen atoms between the non-stoichiometric $TiO_x$ and $TiO_{2-x}N_x$ phases. An increase in temperature results in an increase in N content as shown by the atomic force microscopy (AFM) imagery.

UNIVERSITY of the WESTERN CAPE

***Objective 4:*** To synthesize a NiAl based alloy reinforced with the suitable metal oxynitride and study the resulting composite structure.

- A metallic binder with A356-1Sn-5Ni composition was developed for the $TiO_{2-x}N_x$ ceramic powder. The composite A356-1Sn-5Ni-($TiO_{2-x}N_x$) mixture was liquid-phase sintered at 800 °C. The structural analysis showed that a tetragonal $TiO_{2-x}N_x$ with lattice parameters a=4.585 Å; c=2.960 Å, HCP $TiO_x$ phase with lattice parameters a=5.140 Å; c=9.480 Å and FCC phase with lattice parameter a=5.572 Å were detected in composite material. The density of 4.91 g/cm$^3$ measured on 500 °C annealed sample confirmed the formation of $TiO_x$ phase. Furthermore, dissolution of N at higher temperatures (600, 700 and 800 °C) was accompanied by decrease in density confirming formation of rutile titanium oxynitride.

***Objective 5:*** To synthesize a steel alloy-based matrix reinforced with TiC and study the resulting composite structure.

- The Steel/Ni reinforced with 1.0 -1.5 wt.% ultrafine TiC composites were developed through powder metallurgical compaction and sintering processes. TiC particles segregated around the spherical FeNi grains on the 1.0 wt.% and 1.5 wt.% TiC composite materials. The structural analysis revealed that the 1.0 wt.% TiC-Steel/Ni was composed of the FCC matrix while the 1.5 wt.% TiC-Steel/Ni composite had B2 (BCC) crystal structure. Larger TiC grains were found on the 1.0 wt.% TiC-Steel/Ni composite. On the 1.5 wt.% TiC-Steel/Ni composite, the spherical Steel/Ni matrix was surrounded by the ultrafine TiC grains. The 1.0 wt.% TiC-Steel/Ni composite was composed of lower average hardness compared to the 1.5 wt.% TiC-FeNi composite.

UNIVERSITY of the WESTERN CAPE

### 9.1.2 Future Work

To round up the current study and meet all the objectives set out, the last activity is to:

- Select a suitable steel-based alloy powder,
- Blend the suitable steel-based alloy powder with Titanium oxynitride powder,
- Cold press the blend into cylindrical coupon,
- Sinter the cylindrical coupons to fabricate a composite,
- Perform metallurgical evaluation on the resulting composite, and
- Document the results for peer review.